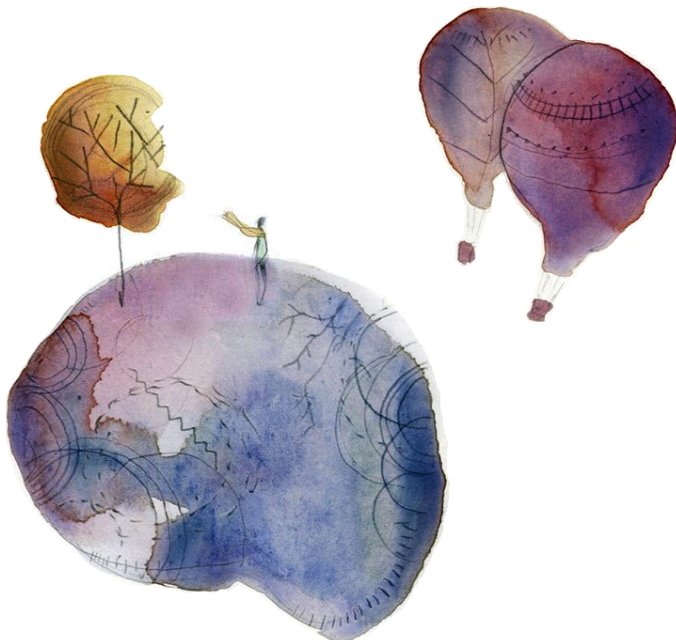


University of Liège
Faculty of Applied Sciences
Department of Electrical Engineering and Computer Science

Dynamical modelling from resting-state brain imaging



PhD Thesis of **Raphaël LIÉGEOIS**

Supervised by Prof. Rodolphe Sepulchre (Advisor)
and Prof. Steven Laureys (Co-advisor)

August 2015

Jury members:

P. Geurts	(Chair)	Professor, University of Liège
R. Sepulchre	(Advisor)	Professor, University of Cambridge - University of Liège
S. Laureys	(Co-advisor)	Professor, University of Liège
R. Lambiotte		Professor, University of Namur (Belgium)
C. Phillips		Associate Professor, University of Liège
B. Thirion		Professor, INRIA and CEA (France)

Abstract

The statistical dependencies among neuroimaging time courses observed in different brain regions are collectively named *functional connectivity* (FC). This quantity is widely used in order to characterize normal brain functioning or neurodegenerative diseases. It is classically measured in a *static* way, by *averaging* the dependencies over the whole imaging acquisition. However, there is increasing evidence that considering the *temporal fluctuations* of FC leads to a finer description of FC properties and corresponding brain function. This observation is the starting point of the work developed throughout this thesis.

First, we study the role of cerebral anatomy in the FC fluctuations. We observe that it guides transitions of FC between different patterns supporting consciousness-related processes such as mind wandering. Following this new characterisation of the fluctuating nature of FC, we develop statistical tools capturing static *and* dynamic properties of FC.

We first introduce three markers of FC, collectively named *spatiotemporal connectivity* (STC), and computed from the power spectral density of the neuroimaging time series. STC captures spatial properties of FC, as classically computed, but also dynamical properties. We show on real data that STC provides a finer characterisation of FC, as well as higher robustness against inherent flaws of the imaging modality considered in our study.

Then, in order to identify dynamical patterns of FC at the whole-brain level, we recast the concept of component analysis in the context of dynamical models. The corresponding development is based on a particular representation of statistical interactions: *dynamical graphical models*. We first propose an algorithm providing a decomposition of these models in a *sparse* contribution, reflecting parsimony of the direct interactions between cerebral regions, and a *low-rank* contribution, modelling the presence of hidden variables spreading a common behaviour in many of these regions. Then, we propose to interpret the identified hidden variables as dynamical neuronal networks, as for component analysis, but with an additional spectral characterisation of the corresponding components.

In conclusion, this thesis presents *descriptive* contributions from the analyses of several datasets, and *methodological* contributions inspired from the properties of these datasets.

Résumé

La motivation initiale de cette thèse a été l'envie, en tant qu'ingénieur, de contribuer au développement des outils d'analyse de données d'imagerie cérébrale. En effet, les modalités d'imagerie actuelles permettent d'acquérir des quantités importantes de données sur l'anatomie cérébrale, ou sur l'organisation de l'activité cérébrale. Cependant l'interprétation de ces données en termes de pathologies, de risques pathologiques, ou simplement en termes de fonctionnement normal du cerveau humain reste très incomplète, constituant par là même un des plus beaux défis scientifiques contemporains. On peut par conséquent espérer que ce type de recherche mènera à des progrès significatifs dans ce domaine, permettant une meilleure compréhension de la nature profonde de l'activité cérébrale et plus largement de la nature humaine.

L'approche la plus répandue pour analyser les données d'imagerie *fonctionnelle*, c'est-à-dire les données mesurant l'*activité* cérébrale dans différentes régions, est la caractérisation de la *connectivité fonctionnelle*, définie comme l'ensemble des interactions statistiques entre les mesures dans ces régions. Il a en effet été montré que cette grandeur des données est pertinente afin de caractériser le fonctionnement -pathologique ou non- du cerveau. Classiquement, la connectivité fonctionnelle est considérée comme étant constatée au cours du temps. Cependant, il a été montré récemment que les *fluctuations* de cette grandeur sont également importantes et permettent de caractériser plus finement les propriétés cérébrales. Cette observation a été le point de départ des développements menés tout au long de cette thèse.

Nous avons d'abord étudié le rôle de l'anatomie cérébrale dans ces fluctuations, et avons observé que l'anatomie guidait les transitions de la connectivité fonctionnelle entre des états présentant des propriétés modulaires différentes. Ensuite nous avons montré que cette réorganisation périodique de la connectivité fonctionnelle reflétait des processus liés à l'état de conscience éveillée des sujets étudiés.

Partant de cette nouvelle observation de l'aspect dynamique et fluctuant de la connectivité fonctionnelle, nous avons ensuite développé différents outils afin de caractériser de manière plus pertinente et plus succincte les propriétés dynamiques de cette grandeur.

Dans un premier temps nous introduisons le concept de connectivité spatio-temporelle, ou STC pour *spatiotemporal connectivity*, rassemblant trois mesures de connectivité fonctionnelle. Les marqueurs de la STC sont calculés à partir de la densité spectrale de puissance des séries temporelles étudiées, et sont définis afin de rendre compte de la connectivité spatiale, comme définie classiquement, ainsi que de ses propriétés dynamiques. Nous montrons ensuite sur des données réelles que la STC permet une caractérisation plus fine des propriétés de connectivité fonctionnelle, et qu'elle permet également plus de robustesse par rapport à certains défauts inhérents au type de données étudiées.

Enfin, afin d'identifier des réseaux dynamiques de connectivité fonctionnelle à l'échelle globale du cerveau nous étendons la notion d'analyse en composantes au cas des modèles dynamiques. Nous nous basons pour ce faire sur une classe particulière de représentation des interactions statistiques entre variables aléatoires: les *modèles graphiques dynamiques*. Nous présentons dans un premier temps un algorithme permettant la décomposition de ces modèles en une contribution *creuse*, modélisant la parcimonie des interactions directes entre les différentes régions cérébrales, et une contribution de *rang faible* qui rend compte de la présence de variables non-observées produisant un comportement similaire dans plusieurs régions cérébrales. Dans un second temps, nous motivons l'interprétation de ces variables cachées comme correspondant à des réseaux neuronaux, comme dans le cas de l'analyse en composantes, mais avec une caractérisation spectrale supplémentaire des composantes correspondantes.

Cette thèse présente donc des contributions descriptives, basées sur l'analyse de données réelles, ainsi que méthodologiques, inspirées des propriétés de ces données. De la même façon que la recherche menée durant cette thèse a été à l'interface des domaines médicaux et de l'ingénierie, nous nous sommes efforcés de rendre la lecture de ce manuscrit accessible et attractive pour les deux communautés. Le rappel de certaines notions de base pourra donc paraître superflu pour le lecteur spécialisé mais nous a semblé pertinent au vu de ce contexte de travail.

Acknowledgements

Completing this thesis has been an enriching and intense experience to which many people contributed. I want here to thank them for their support, help and guidance during the past four years.

First and foremost, I would like to warmly thank my supervisor, Professor Rodolphe Sepulchre, who offered me the opportunity to start this thesis. I am particularly grateful to Rodolphe for his constant support and for giving me so much freedom in my research. More generally, Rodolphe's catching enthusiasm for neuroscience and ability to identify the essence of a research problem, as well as his considerate team management will intimately enrich me as a growing research scientist.

I am also heartily thankful to my co-supervisor, Professor Steven Laureys who gave me the opportunity to explore consciousness, a truly fascinating scientific and philosophical research topic. As a neurologist, Steven perfectly complemented my supervision by providing deeper insight into brain imaging interpretations, challenges and limitations.

I would like to further acknowledge my other close collaborators on specific research projects of this thesis: many thanks to Prof. Andrea Soddu for his warm welcome during my visit at the Brain & Mind Institute and for his caring advice. All my gratitude also goes to Dr. Christophe Phillips for his detailed and prompt answers about various methodological questionings, and to Dr. Erik Ziegler for his precious work and feedback. I finally thank Dr. Bamdev Mishra and Dr. Mattia Zorzi for their thorough explanations and decisive contributions.

Finally, I would like to express my sincere acknowledgements to all the members of the Jury for their interest and for the time devoted to reading and evaluating this thesis.

Working in a stimulating and friendly environment also helped me to enjoy my everyday PhD student life. I thank all my colleagues at the Montefiore Institute, at the Coma Science Group, and all the members of the ReD, the PhD students network of the University of Liège. More specifically, I warmly thank Anne Collard and Marie Wehenkel for our

everyday serious and less serious discussions across the desk. Special thanks further go to Ramouna Fouladi for the magic biking rides. Many thanks finally to Fulvio Forni for his attentive encouragement; to Enrico Amico and Yorgos Antonopoulos for the animated evenings and political discussions; to Laura Trotta for the unexpected philosophical breaks, to Julie Dethier for her catching energy and laughs, to Mohamed Ali Bahri for his technical contributions, and to my other “predecessors” Alexandre Mauroy, Guillaume Drion and Pierre Sacré for their supportive guidance.

I further thank the administrative staff and in particular Sophie Cimino for her cheerfulness and her professionalism.

I feel very lucky to be surrounded and supported by a group of ever standing friends. Lots of thanks to Amory, Loïc, Karim, Yannick, Renaud, Mareg, Dionys and Gilles. I am also grateful to Renaud Pétry for his day-to-day support, and to Marine for taking the final steps of the writing along with me.

My sincere thanks and congratulations also go to Marie Halleux for translating my words and feelings into the front-page illustration.

Finally, my deepest gratitude goes to my family. I owe my parents Philippe and Christine countless thanks for unconditional support and everlasting care over all these years. My blessings also go to my sister Marie and her partner Baptiste for their priceless support and endearment.

Contents

Notations	xi
1 Introduction	1
1.1 Research context and needs	2
1.2 Contributions and publications	6
1.3 Outline of the Thesis	8
2 Static measures of functional connectivity	9
2.1 Introduction	9
2.2 Gaussian and linear statistics	11
2.2.1 The correlation matrix	11
2.2.2 The precision matrix	11
2.2.3 Principal component analysis	16
2.3 Non-gaussian or nonlinear statistics	17
2.3.1 Mutual information	17
2.3.2 Independent component analysis	18
2.4 Other approaches	18
2.5 Conclusion	19
3 Temporal functional connectivity	21
3.1 Introduction	21
3.2 Material and methods	23
3.2.1 Participants	23
3.2.2 Diffusion Weighted Imaging	23
3.2.3 Functional data	24
3.2.4 Sliding Window for FC Analysis	25
3.2.5 Temporal correlation between structural and functional matrices	25
3.2.6 Values of interest	26
3.2.7 Statistical significance of the observed fluctuations	27
3.2.8 Graph theory metrics	28
3.2.9 ROI-level structural and functional contributions	29
3.3 Results	29

3.3.1	Statistical significance of temporal correlation	29
3.3.2	Phases of (de)synchronization between functional and structural connectivities	32
3.3.3	ROI-level analysis	33
3.4	Discussion	35
3.4.1	A) Significance of fluctuations of $R(t)$ observed using the sliding window approach	35
3.4.2	B) Phases of (de)synchronization between functional and structural connectivities	37
3.4.3	C) Future work	40
3.5	Conclusions	41
4	Dynamical measures of functional connectivity	43
4.1	Introduction	43
4.2	Temporal vs. Dynamical models	44
4.3	Dynamical measures and models of FC	44
4.3.1	Directed linear statistics and models	46
4.3.2	Undirected linear statistics and models	49
4.3.3	Nonlinear statistics	51
4.3.4	Model-based measures of FC	51
4.3.5	Dynamical component analysis ?	54
4.4	Conclusion	55
5	Spatiotemporal connectivity	57
5.1	Introduction	57
5.2	Methods	58
5.2.1	Spatiotemporal connectivity	60
5.2.2	STC from the estimated inverse power spectral density	62
5.3	Materials	63
5.3.1	Propofol-induced loss of consciousness dataset	63
5.3.2	Alzheimer patients with different levels of anosognosia dataset	64
5.4	Results	65
5.4.1	Propofol-induced loss of consciousness dataset	65
5.4.2	Alzheimer patients with different levels of anosognosia dataset	68
5.5	Discussion	69
5.5.1	Extending the notion of connectivity	69
5.5.2	Importance of internal memory	70
5.5.3	PSD or inverse PSD ?	70
5.5.4	Limitations and perspectives	71
5.6	Conclusion	71

6 Identification of low-rank plus sparse graphical models	73
6.1 Introduction	73
6.2 Problem formulation	75
6.2.1 S+L graphical models	76
6.2.2 S+L identification problem formulation	78
6.3 Alternating direction method of multipliers	79
6.3.1 Graphical model corresponding to the optimal solution	81
6.4 Results	82
6.4.1 Application on linear synthetic data	82
6.4.2 Application on real data	84
6.5 Discussion	86
6.5.1 Going beyond cubic complexity	87
6.5.2 Accuracy requirements of the proposed decomposition	88
6.6 Conclusion	89
7 From latent variables to dynamic component analysis	91
7.1 Introduction	91
7.2 Component analysis	92
7.2.1 Principal and independent components	92
7.2.2 Component analysis for neuroimaging applications	94
7.3 Characterizing Latent Variables	95
7.3.1 Definition of latent components	96
7.3.2 Linking latent components and component analysis	97
7.4 Results	98
7.4.1 Application on nonlinear synthetic data	98
7.4.2 Application to neuroimaging data	101
7.5 Discussion	103
7.6 Conclusion	103
8 Conclusion	105
8.1 Conclusions	105
8.2 Perspectives	107
Bibliography	109
A Methodological complements to Chapter 3	123
A.1 Correlation between SC and tFC	123
A.2 Other markers of statistical significance	124
A.3 Influence of the threshold	125

B Gaussianity assumption in component analysis	127
B.1 Measuring (non-)gaussianity	127
B.2 PCA and ICA on adequate datasets	128
B.2.1 PCA on gaussian data	128
B.2.2 ICA on non-gaussian data	129
B.3 PCA and ICA on inadequate datasets	131
B.3.1 PCA on non-gaussian data	131
B.3.2 ICA on gaussian data	132

Notations

The following notations are used throughout the thesis.

Sets

\mathbb{N}	The set of natural numbers.
\mathbb{R}	The set of real numbers.
\mathbb{R}^+	The set of positive real numbers.
\mathbb{R}^2	The set of ordered pairs of real numbers.
\mathbb{R}^n	The set of ordered n -tuples of real numbers, or n -dimensional real column vectors.
$\mathbb{R}^{n \times p}$	The set of $n \times p$ real matrices with n rows and p columns.
$[a, b]$	The real interval $\{x \mid a \leq x \leq b\}$.
$\{a, \dots, b\}$	The set of integers $\{x \mid a \leq x \leq b\}$.
(a, b)	The set containing the two real numbers a and b .

Notations on matrices

$\mathbf{A}_{i,j}$	The element at row i and column j in the matrix \mathbf{A} .
\mathbf{A}^T	The transpose of the matrix \mathbf{A} .
\mathbf{A}^*	The conjugate transpose of the matrix \mathbf{A} .
$\text{tr}(\mathbf{A})$	The trace of the square matrix \mathbf{A} .
$\det(\mathbf{A})$	The determinant of the square and invertible matrix \mathbf{A} .
$\ \mathbf{A}\ _2$	The Frobenius norm of the matrix \mathbf{A} .
$\mathbf{A} \succ 0$	The matrix \mathbf{A} is positive definite.
$\mathbf{A} \succeq 0$	The matrix \mathbf{A} is positive semi-definite.
$\exp(\mathbf{A})$	The matrix exponential of \mathbf{A} .
$\log(\mathbf{A})$	The matrix logarithm of the positive definite matrix \mathbf{A} .

Conventions on statistical measures

Φ	Power spectral density.
Σ	Correlation (or Covariance) matrix.
$\tilde{\Sigma}$	Estimated Correlation (or Covariance) matrix.
R_k	k -th lagged correlation (matrix), with $k \in \mathbb{N}$.
p	Usually used to denote the order of an approximation (e.g. in AR models).
$\mathcal{N}(\mu, \Sigma)$	Gaussian distribution of mean μ and covariance Σ .
w	Width of the sliding window.

Conventions on fMRI time series

N	Number of time samples collected in the time series.
m	Number of regions in which the fMRI signal is recorded.
x	time series recorded in m regions and containing N samples, hence $x \in \mathbb{R}^{N \times m}$.
R	Correlation between SC and tFC.
V	Range of variation of R , i.e. the difference between its extreme values.
F^*	Frequency of maximal power spectrum.

Acronyms and abbreviations

fMRI	Functional magnetic resonance imaging.
BOLD	Blood-oxygen level dependent.
DTI	Diffusion tensor imaging.
DWI	Diffusion weighted imaging.
FA	Fractional anisotropy.
PSD	Power spectral density.
Hb	(Oxygenated) hemoglobin.
dHb	(deoxygenated) hemoglobin.
HRF	hemodynamic response function.
AR	Autoregressive.
AR(p)	Autoregressive model of order p .
SC	Structural connectivity.
FC	Functional connectivity.
tFC	Temporal functional connectivity.

CHAPTER 1

Introduction

*“Si le fonctionnement de notre cerveau était simple,
nous serions incapables de le comprendre.”*

—Unknown author

Understanding the basic principles of the human brain is one of the most exciting challenges facing today's research. Every step towards this ultimate goal represents a hope for better treatments of neurological diseases and tells us more about our human nature. Two recent large-scale collaborative research projects illustrate this drive: the BRAIN initiative¹ in the United States of America and its European counterpart: the Human Brain Project². The amounts at stake are at the level of the expected outcomes as neurological disorders have become one of the main causes of mortality in western countries according to the World Health Organization³.

Neurosciences are beautiful in that they are at the meeting point of several domains including, but not limited to, medicine, engineering, physics, ethics, philosophy, biology, mathematics, psychology, chemistry, ethnology or ethology. Consequently, neuroscientists are encouraged to build up multidisciplinary representations of the problems they are facing, in the historic humanistic tradition, placing the human nature at the centre of all attention.

¹ <https://www.whitehouse.gov/brain>

² <https://www.humanbrainproject.eu>

³ <http://www.who.int/mediacentre/factsheets/fs310/en/>

It is in this multi-faceted and effervescent context that our work takes place, more specifically at the edge between brain medicine and systems modelling. As already mentioned being at the crossroads of two different fields has been on the one hand extremely exciting as multiplying the viewpoints helps to build up a coherent understanding of a problematic. On the other hand it has also been difficult to simultaneously meet apparently diverging expectations yielded by these two research approaches. Narrowing the gap between these two fields and eventually identifying converging research paths is in our opinion one of the main contributions of the present thesis.

This Chapter is organised as follows. We first broadly sketch the research context of this thesis, providing some basic notions about functional neuroimaging data. We also highlight some limitations of the classical analyses performed on this data which primarily motivated the work presented in the sequel of this manuscript. We then review the main contributions of our work, as well as the corresponding publications and main communications.

1.1 Research context and needs

The emergence of powerful and noninvasive neuroimaging modalities in the last decades has allowed to actively explore structural and functional properties of the brain. The former basically characterise the anatomical organisation of the brain, and more specifically the organisation of the white matter tracks linking the different cortical regions. Modalities such as Diffusion Tensor Imaging (DTI) allow to capture this information. Complementarily, the latter deals with the spatial and temporal organisation of neuronal activity, mainly taking place in cortical regions, or grey matter.

The different measurement techniques of neuronal activity include electroencephalography (EEG) which provides a measure of electrical activity along the scalp resulting from ionic currents happening within the neurons; positron emission tomography (PET) which measures the level of injected radioactive glucose uptake supposed to be a relevant marker of underlying neuronal activity; single-photon emission computed tomography (SPECT) which is conceptually similar to PET but which uses different radioactive tracers hereby highlighting different cerebral properties; or functional magnetic resonance imaging (fMRI) which is sensitive to the level of blood deoxyhemoglobin and on which we focus in the present manuscript. The properties on which some of the neuroimaging modalities cited here above are based are represented in Figure 1.1.

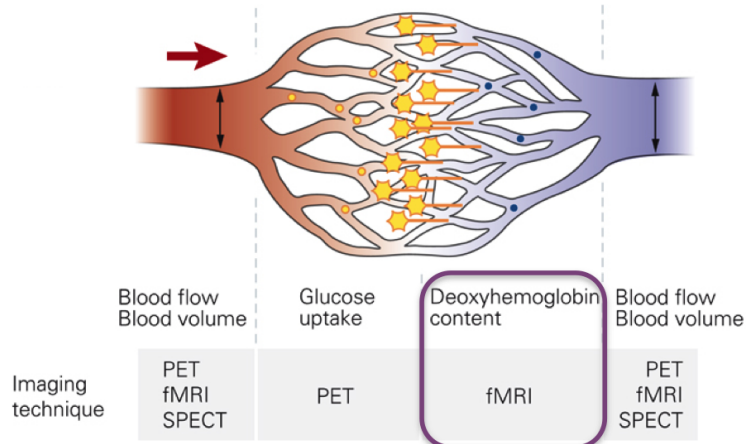


Figure 1.1 – Properties of cerebral blood flow on which some of the main *functional* neuroimaging techniques are based, from [Garraux \(2014\)](#).

We now briefly define the main properties of the so-called BOLD signal used in fMRI. We then explain how new requirements coming from the central neuroimaging application discussed in this thesis led us to blend existing tools with these requirements, based on recent methodological results.

The BOLD signal

We focus in the present work on the fMRI modality, which is based on the Blood Oxygenation Level Depend -or BOLD- signal, for two main reasons. First, unlike PET or SPECT, fMRI is completely noninvasive since it is not required for the patients to absorb radioactive tracers. Then, because the spatial and temporal resolutions of the BOLD signal allow for decent spatial and temporal characterisation of cerebral activity. The temporal resolution is on the order of the second, or even in the sub-second range for the newest machines, whereas PET and SPECT result in a single activation map, hence without any temporal information, and EEG, on the contrary, has a higher temporal resolution on the order of the millisecond. The spatial resolution, however, is much better for the BOLD signal (on the order of the millimeter in the whole brain) whereas for EEG the signal has a low-to-medium resolution for regions close to the scalp (on the order of several centimeters) and very low resolution for internal cerebral regions such as the brain stem because the electrical signal is too much distorted by the skull.

As illustrated in Figure 1.2, the BOLD signal captured by the fMRI modality is due to an underlying neural activation resulting in an increased blood flow in the region where the activation takes place. This increased blood flow is regulated by complex hormonal reactions that aim at bringing more oxygen on the site of the neuronal activation. Oxygen is transported by hemoglobin that can be either oxygenated (Hb), or deoxygenated (dHb).

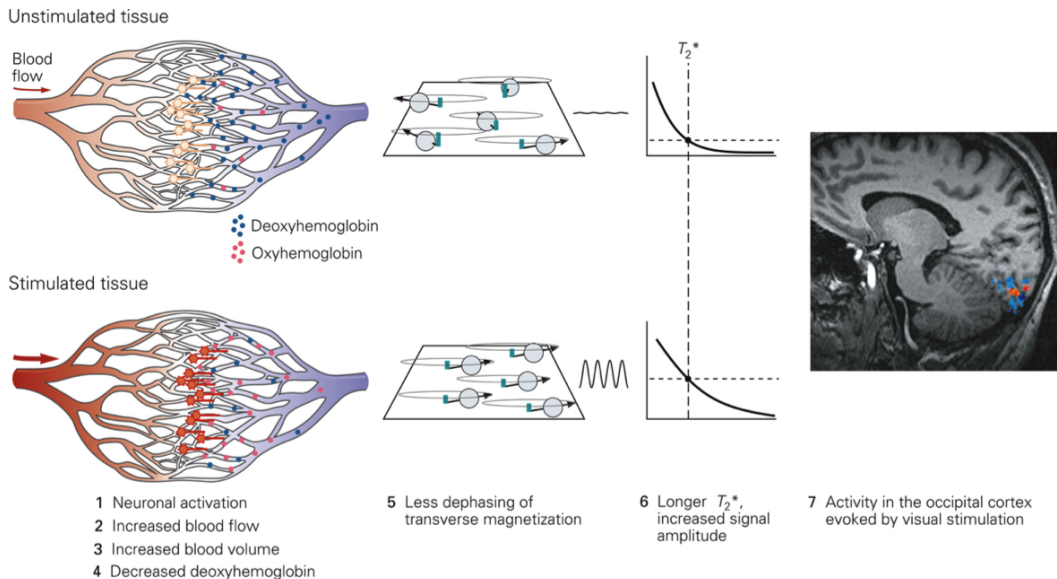


Figure 1.2 – Basic principles leading to the emergence of the BOLD signal, from [Garraux \(2014\)](#).

Hence, when a tissue is stimulated due to an underlying neuronal activation, the proportion of dHb decreases. Finally, since dHb is paramagnetic whereas Hb is diamagnetic, this leads to a different (de)magnetisation of the spins of the haemoglobin molecules that is captured by the magnetic resonance framework used in fMRI.

It should be noted that the way a neuronal activation translates into a change of the corresponding BOLD signal is characterised by the so-called *hemodynamic response function*. Typically, a neuronal activation results in a change of the BOLD signal after 1-2 seconds, with a peak in the BOLD signal after 4-6 seconds, and these values can be significantly different for different regions of the brain ([Buxton et al., 2004](#)).

Eventually, the BOLD signal consists of a collection of time series corresponding to different brain regions, or voxels that we denote $x(t), t \in \{1, \dots, N\}$ throughout the present manuscript. $x(\cdot)$ is a vector of size m , the number of voxels, or cerebral regions that are considered, and N is the total number of samples, usually on the order of several hundreds with a sampling period around 2 seconds corresponding to recordings of several minutes.

(Dynamical) functional connectivity

To date, the primary way to exploit information encoded in the fMRI time series has been to detect statistical dependencies between possibly remote cerebral regions. Once such a

statistical dependence is detected, the corresponding regions are said to be “functionally connected” (Biswal et al., 1997; Friston, 2011). The simplest way to detect these dependencies from the fMRI time series $y(t)$ is to compute the corresponding empirical correlation⁴ matrix, also called *connectivity* matrix:

$$\tilde{\Sigma} = \frac{1}{N}(x^T \cdot x), \quad (1.1)$$

and then detect significant correlations in the square matrix $\tilde{\Sigma}$ of size m .

The main drawback of this classical way of evaluating functional connectivity is that it assumes a constant level of functional connectivity during the whole fMRI acquisition. However, there is increasing evidence that this is not true and that one should blend analyses of functional connectivity with the temporal and dynamical properties of this quantity, even during resting-state experiments as the ones considered in the present work (Hutchinson et al., 2013).

This new modelling approach of functional connectivity is called “dynamical functional connectivity” for which the dynamical information can be encoded in various ways. In this work we present extensions of existing tools in order to capture this information. We also propose a novel dynamical framework based on component analysis, which is introduced in the next Section.

(Dynamical) component analysis

From a methodological point of view, static component analysis techniques such as principal or independent component analysis have been largely used in order to decode information contained in the correlation matrix $\tilde{\Sigma}$ computed from (1.1). Indeed, the corresponding components which capture large-scale correlation patterns are easily interpreted in terms of *neuronal networks*, as explained in further details in Chapter 2.

Following the general motivations described in the previous Section from the applicative point of view, and building upon recent results on identification of the low-rank structure of interactions in multivariate time series (Zorzi and Sepulchre, 2015), we propose to recast the notion of component analysis in the context of dynamical systems. We then analyse dynamical functional connectivity in artificial and real datasets using our new proposed framework. This work is detailed in Chapters 6 and 7 and is the main methodological contribution of this dissertation. It is motivated throughout the manuscript by a concrete application and by a comparison with other dynamical modelling approaches reviewed and tested, for some of them, in the preceding Chapters.

⁴ Since all BOLD, or fMRI, signals are precentered and unit normalised in the classical preprocessing steps, covariance and correlation are equivalent statistics

1.2 Contributions and publications

The main contributions of this thesis and corresponding publications or communications follow the outline of motivations and methodological limitations they try to address and described here above. They can be gathered in three groups of main contributions:

1. The first main contribution is a detailed analysis of the temporal fluctuations of functional connectivity in which we:
 - Assess the presence of *significant* (i.e. not due to noise) temporal fluctuations of functional connectivity using a sliding window.
 - Determine which window width should be used in order to best unveil these fluctuations, leading to confirmatory yet original results.
 - Characterise how underlying anatomy shapes these fluctuations of functional connectivity.
 - Argue why these fluctuations might reflect consciousness-related processes such as mind wandering.

These results are presented in Chapter 3 and are essentially based on the following journal paper:

R. Liégeois, E. Ziegler, C. Phillips, P. Geurts, F. Gómez, M. Ali Bahri, B.T.T. Yeo, A. Soddu, A. Vanhaudenhuyse, S. Laureys, and R. Sepulchre. Cerebral functional connectivity periodically (de)synchronizes with anatomical constraints. Brain Structure and Function, In press, 2015.

2. Then, after the review of different dynamical models of functional connectivity proposed in Chapter 4, we introduce a measure of connectivity called *spatiotemporal connectivity (STC)* based on lagged correlation sequences. The outcomes of this novel approach can be summarised as follows:
 - We extend the classical notion of correlation (1.1) to dynamical models using STC.
 - We show, on two different fMRI datasets that STC provides a finer characterisation of spatial and temporal properties of connectivity.

These results are detailed in Chapter 5 and are based on an original formulation that was selected for an oral presentation during the Second Whistler Scientific Workshop on Brain Function:

R. Liégeois, M. Ali Bahri, M. Zorzi, S. Laureys, and R. Sepulchre. Dynamical properties of fMRI connectivity in neuronal networks mediating consciousness. *Second Whistler Scientific Workshop on Brain Function, Whistler, Canada, 2014.*

3. The last Chapters of this manuscript are then devoted to the development of an efficient algorithm implementing a method that could be seen as an extension of classical component analysis techniques to dynamical models. In these Chapters we:

- Provide an algorithm able to compute the sparse plus low-rank autoregressive identification on datasets of dimensions typically encountered in neuroimaging applications.
- Detail the links between the low-rank part of this decomposition and classical component analysis techniques.
- Apply our proposed framework on a real fMRI dataset and show that the spatiotemporal subspace encoded in the low-rank part of the decomposition provides further insight about the neuronal networks that are classically identified using component analysis techniques.

This work is detailed in Chapters 6 and 7, based on the following paper:

R. Liégeois, B. Mishra, M. Zorzi, and R. Sepulchre. Sparse plus low-rank autoregressive identification in neuroimaging time series. *Paper accepted for the 54th IEEE Conference on Decision and Control, Osaka, December 2015.*

Finally, let us note that another journal paper was published in which our contribution was to provide better insight about the properties of principal component analysis and the corresponding principal components. We do not detail the results of this paper as they do not significantly contribute to the mainline of the development conducted throughout this thesis.

H. Y. Chen, R. Liégeois, J. R. de Bruyn, and A. Soddu. Principal component analysis of particle motion. *Physical Review E 91, 042308, 2015.*

1.3 Outline of the Thesis

The dissertation is organised as follows.

Chapter 2 first provides a formal definition of *functional connectivity* (FC) and then reviews the classical *static* measures used to evaluate FC from fMRI data such as correlation of the fMRI time series.

Chapter 3 studies the *temporal fluctuations* of FC, as measured by the correlation between the fMRI time courses within a sliding window. We particularly focus on the role of brain anatomy in these fluctuations. The link between the observed FC fluctuations and consciousness-related processes such as mind wandering is also motivated. We eventually highlight the limitations of the classical sliding window approach and propose possible improvements.

Chapter 4 first makes the distinction between *temporal* approaches -as the one used in Chapter 3- and *dynamical* approaches for characterising FC fluctuations. We then propose a broad review of different *dynamical* modelling approaches that have been used in order to explore the properties of these fluctuations. Their underlying assumptions, drawbacks and advantages are described in light of the properties of the FC fluctuations they aim to describe.

Chapter 5 proposes a novel and simple marker of connectivity that includes its dynamical properties and that we call *spatiotemporal connectivity (STC)*. This marker is based on lagged correlation matrices and is used for two main reasons. First because this measure is not too sensitive to delays inherent in fMRI time series, and then because it is one of the simplest statistics able to capture the dynamical information encoded in these time series. STC is applied to two fMRI datasets, and in each case it provides a finer analysis of FC dynamics compared to classical connectivity markers.

Chapter 6 presents the main methodological contribution of the thesis. We propose an algorithm able to deal with the dimensions of datasets typically encountered in neuroimaging and computing the *sparse plus low-rank* autoregressive representation from multivariate time series.

Chapter 7 proposes a detailed interpretation of the *low-rank* term in the decomposition presented in Chapter 6. In particular, the links with classical component analysis techniques are discussed from a theoretical point of view as well as based on the analysis of synthetic and real fMRI datasets.

Chapter 8 reviews the main conclusions of this dissertation and identifies potential future research directions.

CHAPTER 2

Static measures of functional connectivity

“Invisible threads are the strongest connections.”

—Friedrich W. Nietzsche

2.1 Introduction

As briefly discussed in the introductory Chapter, *functional connectivity* is a key concept in neuroimaging that Friston (2011) defines as follows:

Definition 2.1.1 *Functional connectivity (FC) collectively denotes the statistical dependencies existing among and between observed neurophysiological responses.* ◇

In this Chapter we propose to review the classically used *static* measures of FC, i.e. the measures that do not take into account potential temporal fluctuations of FC. We also describe the corresponding generative models, main properties, and in which context they are used in order to evaluate functional connectivity from fMRI time series.

The proposed classification is shown in Figure 2.1, and is mainly based on the (non)-linearity of FC measures.

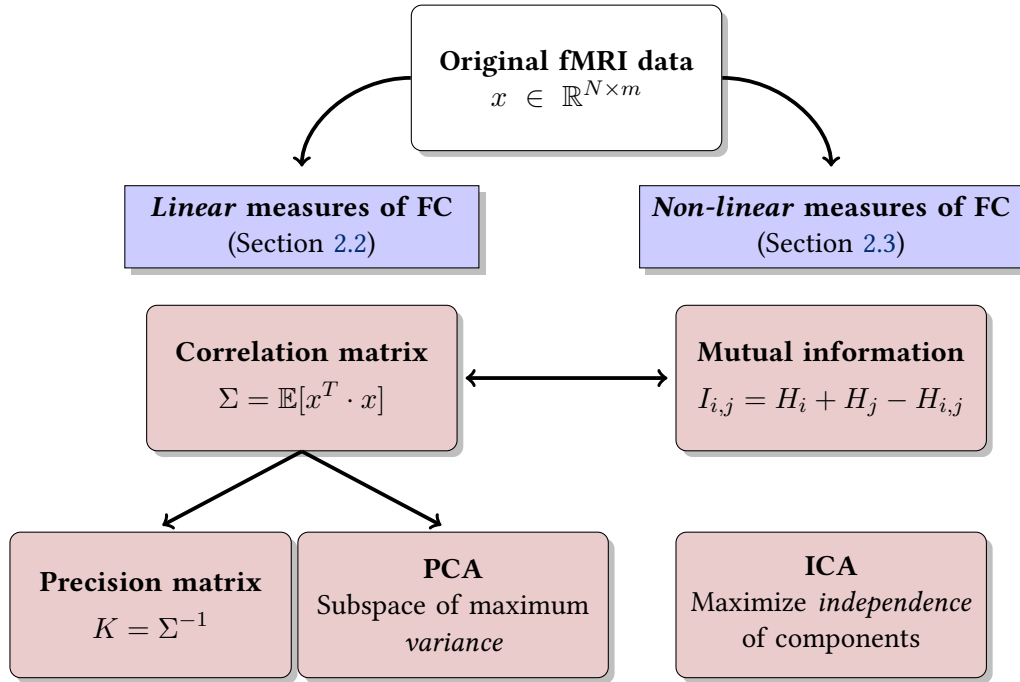


Figure 2.1 – Starting from the original (preprocessed) fMRI data represented in the upper white box, this schematic provides an overview of different popular *static* measures of functional connectivity, and their links with classical *static* measures of connectivity. The main distinction on which the proposed classification is based is the (non-)linearity of proposed FC measures. PCA(ICA) stands for Principal(Independent) Component Analysis.

It should be noted that linearity of FC measures corresponds to a gaussian modelling framework. Indeed, gaussian variables are characterised by their first two statistical cumulants: their mean and covariance. In the case of centered and unit normalised variables, as for fMRI preprocessed data, observed variables in fMRI acquisitions are entirely characterised by their covariance, or correlation matrix since the variables are classically centered and unit normalised during the preprocessing steps. Because the correlation matrix encodes linear relationships between every pair of variables, the gaussianity assumption naturally translates in linear statistical dependencies and connectivity.

Moreover, let us highlight that the BOLD signal is usually assumed to be well approximated by gaussian distributions. This assumption is motivated by the fact that the BOLD signal results from the *linear* superposition of several signals (Boynton et al., 1996; Dale and Buckner, 1997), which converges towards a gaussian distribution whatever the distribution of these underlying signals (central limit theorem, Laplace (1809)). However, the nature of the underlying signals is more controversial which motivates the development of various gaussian and non-gaussian frameworks that we now describe.

2.2 Gaussian and linear statistics

We first describe the group of statistics making the assumption that the observed variables are (jointly-)gaussian which, as just explained, results in FC measures capturing the *linear* dependencies between the variables.

2.2.1 The correlation matrix

The most popular measure of FC from fMRI time series $x(t)$ is the corresponding *correlation* matrix, estimated from $x(t)$ as:

$$\tilde{\Sigma} = \frac{1}{N}(x^T \cdot x), \quad (2.1)$$

where N is the number of fMRI time samples, or fMRI volumes. As suggested here above, $\tilde{\Sigma}_{i,j}$ encodes the strength of the *linear* relationship between the two variables x_i and x_j , hence the correlation matrix as computed in (2.1) provides a global measure of functional connectivity reflecting the strength of the (symmetric) linear dependencies between every pair of variables.

This measure of FC has been extensively used in order to characterise properties of FC during resting-state, or during different states and tasks (for a review see [Friston, 2011](#)).

One limitation of estimating FC from the correlation matrix (2.1) is that dependencies can arise from intermediate relationships, or triangulations. For example, if x_i and x_j are highly correlated, and x_i and x_k are highly correlated, then we might expect that x_j and x_k are also highly correlated even though there is no “direct” link between these variables, except via the intermediate variable x_i . This caveat of correlation coefficients is the main motivation of the statistics we now describe.

2.2.2 The precision matrix

The *inverse* of the correlation matrix, or *precision* matrix, encodes *conditional* dependencies between the observed variables. More precisely, each entry of the precision matrix encodes the dependence between the two corresponding variables, *conditioned* on the knowledge of all the other variables.

An intuitive example

In order to get a better insight about the interpretation of this measure, let us consider the following example. The mass-spring system of Figure 2.2, adapted from [MacKay \(2006\)](#), represents a set of three coupled masses whose positions along the main axis are denoted

by the three variables x_1 , x_2 , and x_3 , and dots in the matrices denote non-zero values.

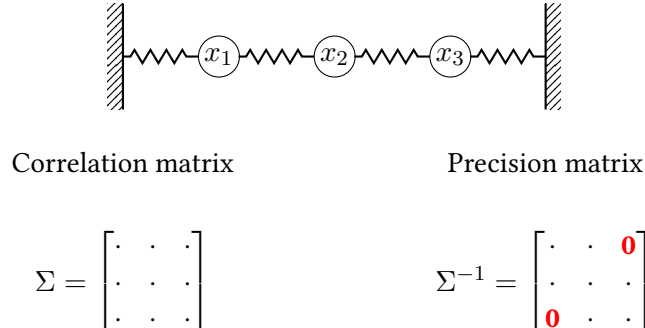


Figure 2.2 – Illustration of the difference between correlation and precision matrices. Dots in the matrices represent values different from zero.

If we assume these masses are subject to random excitation, their coupling through the springs leads to some correlations between their motions. The correlation matrix encodes the usual interpretation of (linear) dependence, and obviously every pair of variables is positively correlated. On the other hand, the precision matrix encodes *conditional* dependence. For example, $(\Sigma^{-1})_{1,3}$ encodes the dependence between x_1 and x_3 , knowing the value of x_2 , or fixing x_2 , and hence its value is zero. This example clearly illustrates that the precision matrix encodes *direct* connections between the variables and do not take into account correlations that might arise from intermediate connections, as in the case of correlation matrices defined in the previous section.

It should be noted that the information encoded in the precision matrix is intimately related to the notion of *partial correlation* that is also used to characterise functional connectivity (e.g. [Ryali et al., 2012](#)). Denoting by $\rho_{i,j}$ the partial correlation between two variables x_i and x_j , the following relationship holds ([Whittaker, 1990](#)):

$$\rho_{i,j} = -\frac{(\Sigma^{-1})_{i,j}}{\sqrt{(\Sigma^{-1})_{i,i}(\Sigma^{-1})_{j,j}}}.$$

Hence, partial correlations also encode *direct* connections between the variables and can be seen as a standardised, or normalised, version of the information contained in the precision matrix.

Precision matrix and conditional dependence: mathematical groundings

We now formally derive the mathematical justifications of this interpretation of the precision matrix, which are not always clearly referred in papers on this topic.

Conditional distribution of the multivariate normal distribution

Consider an n -dimensional random vector $\mathbf{X} = [\mathbf{X}_I \ \mathbf{X}_J] \sim \mathcal{N}(\mu, \Sigma)$ where \mathbf{X}_I and \mathbf{X}_J denote a partition of the n variables of \mathbf{X} in p and q variables, respectively. μ and Σ can be expressed as:

$$\mu = \begin{bmatrix} \mu_I \\ \mu_J \end{bmatrix} \quad \text{and} \quad \Sigma = \begin{bmatrix} \Sigma_{II} & \Sigma_{IJ} \\ \Sigma_{JI} & \Sigma_{JJ} \end{bmatrix}. \quad (2.2)$$

For clarity purposes we will consider centred variables (i.e. $\mu_I = \mu_J = 0$). The joint density of \mathbf{X} is:

$$f(\mathbf{X}) = f(\mathbf{X}_I, \mathbf{X}_J) = \frac{1}{(2\pi)^{n/2} \det(\Sigma)^{1/2}} \exp\left[-\frac{1}{2}\mathbf{X}^T \Sigma^{-1} \mathbf{X}\right] \quad (2.3)$$

$$= \frac{1}{(2\pi)^{n/2} \det(\Sigma)^{1/2}} \exp\left[-\frac{1}{2}\mathcal{Q}(\mathbf{X}_I, \mathbf{X}_J)\right] \quad (2.4)$$

where $\mathcal{Q}(\mathbf{X}_I, \mathbf{X}_J)$ is defined as:

$$\mathcal{Q}(\mathbf{X}_I, \mathbf{X}_J) = \mathbf{X}^T \Sigma^{-1} \mathbf{X} \quad (2.5)$$

$$= [\mathbf{X}_I, \mathbf{X}_J]^T \begin{bmatrix} \Sigma_{II} & \Sigma_{IJ} \\ \Sigma_{JI} & \Sigma_{JJ} \end{bmatrix} \begin{bmatrix} \mathbf{X}_I \\ \mathbf{X}_J \end{bmatrix} \quad (2.6)$$

$$= \mathbf{X}_I^T \Sigma^{II} \mathbf{X}_I + 2\mathbf{X}_I^T \Sigma^{IJ} \mathbf{X}_J + \mathbf{X}_J^T \Sigma^{JJ} \mathbf{X}_J \quad (2.7)$$

and the following notation is used:

$$\Sigma^{-1} = \begin{bmatrix} \Sigma_{II} & \Sigma_{IJ} \\ \Sigma_{JI} & \Sigma_{JJ} \end{bmatrix}^{-1} = \begin{bmatrix} \Sigma^{II} & \Sigma^{IJ} \\ \Sigma^{JI} & \Sigma^{JJ} \end{bmatrix}. \quad (2.8)$$

The distribution of \mathbf{X}_J conditioned on the knowledge of \mathbf{X}_I is denoted $f(\mathbf{X}_J | \mathbf{X}_I)$ and is computed by:

$$f(\mathbf{X}_J | \mathbf{X}_I) = \frac{f(\mathbf{X}_I, \mathbf{X}_J)}{f(\mathbf{X}_I)}, \quad (2.9)$$

where $f(\mathbf{X}_I)$ is the marginal distribution of \mathbf{X}_I .

After basic manipulation that can be found for example in pp. 116-117 of [Eaton \(1983\)](#) it is possible to express $\mathcal{Q}(\mathbf{X}_I, \mathbf{X}_J)$ as $\mathcal{Q}(\mathbf{X}_I, \mathbf{X}_J) = \mathcal{Q}_1(\mathbf{X}_I) + \mathcal{Q}_2(\mathbf{X}_I, \mathbf{X}_J)$ with:

$$\begin{cases} \mathcal{Q}_1(\mathbf{X}_I) = \mathbf{X}_I^T \Sigma^{II} \mathbf{X}_I \\ \mathcal{Q}_2(\mathbf{X}_I, \mathbf{X}_J) = (\mathbf{X}_J - b)^T A^{-1} (\mathbf{X}_J - b) \end{cases} \quad (2.10)$$

where we defined:

$$b = \Sigma_{IJ}^T \Sigma_{II}^{-1} \mathbf{X}_I \quad (2.11)$$

$$A = \Sigma_{JJ} - \Sigma_{IJ}^T \Sigma_{II}^{-1} \Sigma_{IJ} \quad (2.12)$$

Then, after computing the marginal distribution of \mathbf{X}_I :

$$f(\mathbf{X}_I) = \int f(\mathbf{X}_I, \mathbf{X}_J) d\mathbf{X}_I = \frac{1}{(2\pi)^{p/2} \det(\Sigma_{II})^{1/2}} \exp\left[-\frac{1}{2} \mathbf{X}_I^T \Sigma_{II}^{-1} \mathbf{X}_I\right], \quad (2.13)$$

the conditional distribution of \mathbf{X}_J given \mathbf{X}_I naturally follows from (2.9):

$$f(\mathbf{X}_J | \mathbf{X}_I) = \frac{1}{(2\pi)^{q/2} \det(A)^{1/2}} \exp\left[-\frac{1}{2} \mathbf{X}_J^T A^{-1} \mathbf{X}_J\right]. \quad (2.14)$$

Conditional dependence is encoded in the precision matrix

Consider the same variable $\mathbf{X} = (x_1, x_2, \dots, x_n)$ and the particular case where the set $J = (k, l)$ and $I = \{1, \dots, n\} \setminus (k, l)$. The centered gaussian variables x_k and x_l are independent, or equivalently uncorrelated¹, conditioned on all the other variables if and only if the covariance associated to $f(\mathbf{X}_J | \mathbf{X}_I)$ in (2.14) is diagonal, that is, using the properties of the Schur complement:

$$A = \Sigma_{JJ} - \Sigma_{IJ}^T \Sigma_{II}^{-1} \Sigma_{IJ} = (\Sigma^{-1})_{JJ}^{-1} \quad (2.15)$$

should be diagonal. This leads to the final result: x_k and x_l are independent, conditioned on all the other variables, if and only if:

$$(\Sigma^{-1})_{kl} = 0. \quad (2.16)$$

¹ This is due to the fact that gaussian variables are completely characterised by their first two statistical moments, but is not true in general

Graphical models

A particular class of graphs, called *graphical models* precisely encode these conditional independence relationships. Each node of such a model represents a variable, and there is an edge between the nodes corresponding to variable x_k and variable x_l if and only if the corresponding element of the precision matrix $(\Sigma^{-1})_{kl}$, as just defined in (2.16), is different from zero. For example, the graphical model representing the system of Figure 2.2 is represented in Figure 2.3.

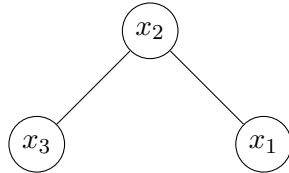


Figure 2.3 – Graphical model corresponding to the system of Figure 2.2.

Graphical models are popular because they lead to concise representations of conditional dependencies, especially if the precision matrix is sparse.

The covariance selection problem

The covariance selection problem is a classical identification problem strongly related to the interpretation of the precision matrix (2.16). This estimation problem first formulated in [Dempster \(1972\)](#) results from the maximum likelihood estimation of the covariance matrix of a centered gaussian random variable $x \sim \mathcal{N}(0, \Sigma)$ from N samples of that variable: $x_i, i \in 1, \dots, N$. The likelihood function, given the data, is:

$$h(\Sigma) = c \frac{1}{\det(\Sigma)^{N/2}} \prod_{i=1}^N \exp\left[-\frac{1}{2} x_i^T \Sigma^{-1} x_i\right] \quad (2.17)$$

$$= c \frac{1}{\det(\Sigma)^{N/2}} \exp\left[-\frac{N}{2} \text{tr}(\Sigma^{-1} \cdot \bar{\Sigma})\right] \quad (2.18)$$

$$= c \exp\left[-\frac{N}{2} (\ln \det(\Sigma) + \text{tr}(\Sigma^{-1} \cdot \bar{\Sigma}))\right] \quad (2.19)$$

where $\bar{\Sigma}$ is the sample covariance estimate.

This likelihood function is maximised by maximising the argument of the exponential in (2.19). However, since $\ln \det(\cdot)$ is a concave function on the positive semidefinite cone,

we change the variables by setting $K = \Sigma^{-1}$ which leads to the final covariance selection optimization problem:

$$\min_{K\succ 0} = -\ln \det(K) + \mathbf{tr}(K \cdot \bar{\Sigma}) \quad (2.20)$$

which is convex. Another advantage of changing variables is that the formulation (2.20) can be blended with regularisation terms inducing *sparsity* of K , the precision matrix, as the number of *direct* interactions between the variables is supposed to be limited. This regularisation is the most common one because it results in simple models of the statistical interactions, that can be efficiently represented by graphical models defined in the previous Section. Other types of regularisations are also possible based on this formulation, as we will show in Chapters 6 and 7 of this manuscript.

Precision matrices in fMRI

The measure of functional connectivity through *direct* interactions between the variables has also been tested in fMRI data (e.g. [Marrelec et al., 2006](#)) but with a limited use, compared to the correlation matrix. One possible explanation for this comes from the fact that different clusters of variables with a common behaviour might be less visible in the precision matrix as each entry of this matrix captures residual dependences between variables, neglecting this common behaviour. Since these large-scale patterns of correlated activity in many variables are important in functional connectivity studies (see [Moussa et al. \(2012\)](#) and next section), this might explain why precision matrices have gained less interest than correlation matrices in this context so far.

2.2.3 Principal component analysis

Generally speaking, component analysis aims at modelling the observed variables as the superposition, or the sum, of different *components* spreading a common behaviour (with different weights) in all the variables.

In the case of principal component analysis (PCA), the corresponding components called *principal* components capture a subspace of maximal *variance* of the observed variables ([Jolliffe, 2002](#)). This framework also makes the assumption of gaussian observed variables, entirely characterised by their covariance, which is the reason why the criterion of maximum variance is used for the subspace identification since it naturally translates into a subspace capturing maximum information contained in the observed dataset.

From a mathematical point of view, the principal components are identified by computing the eigenvectors of the estimated covariance, or correlation matrix $\tilde{\Sigma}$ defined in (2.1) associated to the highest eigenvalues. Hence, PCA can be seen as an alternative to

represent information encoded in $\tilde{\Sigma}$ that models functional connectivity as the superposition of different orthogonal connectivity patterns ([Liégeois, 2011](#)). This representation has three main advantages:

1. First this static approach is simple, well-grounded on clear hypotheses about the nature of fMRI time series; we refer the interested reader to Appendix B for a detailed description of PCA, the corresponding generative model, and a comparison with another component analysis technique: independent component analysis (ICA) that is briefly described in the next section.
2. Then, considering only the first principal components allows to reduce the dimensionality of the initial data, keeping only the subspace capturing most information and removing noise.
3. Finally, it has also been shown that the hidden variables h in these models can be interpreted as *neuronal-networks*. These networks encode some large-scale coordinated activation of different and possibly remote cerebral regions that were associated to different cognitive tasks -even during resting-state acquisitions-, thereby providing a straightforward neurological interpretation of every hidden variable ([Moussa et al., 2012](#)).

2.3 Non-gaussian or nonlinear statistics

It has been suggested that measuring functional connectivity using nonlinear statistics can help reveal other types of dependencies than the linear dependency captured in the correlation matrix (e.g. [David et al., 2004](#)). We now describe two of the corresponding approaches.

2.3.1 Mutual information

This measure, derived from information theory, is defined for two random variables x_i and x_j as follows:

$$I(x_i, x_j) = H(x_i) + H(x_j) - H(x_i, x_j), \quad (2.21)$$

where $H(x_i)$ is the marginal (Shannon) entropy of x_i , and $H(x_i, x_j)$ the joint entropy of x_i and x_j . Intuitively, mutual information, or MI, evaluates the amount of information, in the sense of Shannon, shared by two variables. This is computed by determining the degree of similarity between the joint probability distribution of these variables and the product of their marginal distributions. Using information theoretic measures allows to quantify not only linear dependencies, as for correlation, but also non linear dependencies between variables, as illustrated in [Chai et al. \(2009\)](#).

We do not further develop the motivations behind information theory metrics, but we present mutual information in this Chapter for two reasons. First, it is the basis for other popular *dynamical* measures such as transfer entropy presented in Chapter 4. Then, it can be seen as the nonlinear extension of the classical correlation measure defined here above, with an exact relation between these two measures that can be derived in some cases as shown in [Li \(1990\)](#).

2.3.2 Independent component analysis

Independent component analysis, or ICA, is another component analysis approach related to PCA in the sense that the primal motivation is also to decompose the data in a sum of several components, but these components are identified based on a different criterion. Indeed, ICA assumes that the *hidden* variables are non-gaussian, and identify the so-called *independent* components by maximising their non-gaussianity ([Hyvärinen et al., 2001](#)). The interested reader will find in Appendix B a detailed description of ICA and some applications on different toy examples. Let us just note two main advantages of ICA, which make it one of the most popular approaches in order to identify the *neuronal networks* mentioned here above (see e.g. [Calhoun et al. \(2001\)](#)).

1. First, as for PCA, independent components can be easily interpreted in terms of *neuronal networks*, hereby providing a natural interpretation of the hidden variables.
2. Then, since the neuronal networks are supposed to be *sparse*, i.e. only some regions of the brain are implied in a particular neuronal network, ICA is well suited in order to identify them because sparse distributions correspond to highly non-gaussian components which are preferentially identified by ICA ([Daubechies et al., 2009](#)).

However, since non-gaussianity is a scale-free measure, as opposed to (co)variance, the independent components can not be ranked and no dimensionality reduction can be performed based on this approach. In addition, two different runs of ICA algorithms with two different initial conditions might lead to two different results, which makes it less robust compared to the PCA framework for example ([Liégeois, 2011](#)).

2.4 Other approaches

Other tools have been used in order to characterise functional connectivity from fMRI data. Let us mention graph theoretic metrics, computed from *adjacency* matrices corresponding to a particular graph. Since the adjacency matrices are usually binary matrices -there is either an edge or no edge between two variables-, the most frequently used approach to characterise FC is to threshold the correlation matrix (2.1) which can then be interpreted as a binary adjacency matrix ([Bullmore and Bassett, 2011](#)). From there, different metrics of

the corresponding graph can be computed such as small-worldness, modularity, efficiency, or more generally (hierarchical) clustering measures (e.g. [Meunier et al., 2010](#)).

These types of markers could obviously also be relevant in order to characterise FC. However, there are many different markers leading to various specific characterisations of the FC properties, sometimes with more complex neurological interpretations.

2.5 Conclusion

We have seen that *functional connectivity*, as defined in Definition 2.1.1, can be measured in different ways with a corresponding statistical interpretation, mainly distinguished based on the (non-)gaussianity assumption on the statistical model.

Among gaussian statistics, the most popular measure of FC from fMRI data is the correlation matrix (2.1) of the fMRI time series which encodes *linear* dependencies between every pair of variables. On the contrary, the inverse of the correlation matrix, the precision matrix, encodes *conditional* dependencies among the variables, leading to an interpretation of FC that will discount third-party effects, such as shared inputs from a third node. Then, principal component analysis allows to identify a subspace capturing the largest part of information contained in the data, hereby reducing the dimensionality of the problem. This subspace is encoded in aggregate variables, or components, that have natural neurological interpretations.

Next, non-gaussian frameworks such as mutual information and independent component analysis extend these notions in order to capture broader types of dependencies between the variables, i.e. not only the linear relationships. The counterpart of this generalisation is a higher complexity of the corresponding mathematical tools, and a possible lack of interpretability of resulting functional connectivity measures.

The common point of the statistics presented in this Chapter is that they are *static* measures of functional connectivity, that is, they do not take into account potential fluctuations of FC. However, as mentioned in the introductory Chapter, it has been shown that FC shows temporal fluctuations, leading to different FC patterns in different periods of the fMRI acquisition ([Hutchison et al., 2013](#)). If a *static* measure is computed from this known fluctuating FC, these fluctuations are in a certain sense averaged over the whole time courses, leading to a unique FC measure that neglects these fluctuations. Chapter 3 illustrates how static FC measures can be adapted in order to account for the fluctuating nature of FC.

CHAPTER 3

Temporal functional connectivity

The primal motivation of the work presented in this manuscript has been to explore the temporal fluctuations of functional connectivity defined in the previous Chapter, and measured from fMRI time series. As the presence of these fluctuations had already been assessed, we chose to explore how the underlying cerebral anatomy, i.e. the white matter tracks linking the different cortical regions, shapes these fluctuations and eventually how and if they support consciousness-related processes. The present Chapter is essentially based on the results of [Liégeois et al. \(2015\)](#):

R. Liégeois, E. Ziegler, C. Phillips, P. Geurts, F. Gómez, M. Ali Bahri, T. Yeo, A. Soddu, A. Vanhaudenhuyse, S. Laureys, and R. Sepulchre. *Cerebral functional connectivity periodically (de)synchronizes with anatomical constraints*. Brain Structure and Function, In press, 2015.

3.1 Introduction

As presented in the introductory Chapters, the human brain shows organized spatiotemporal activity even in task-free or “resting-state” conditions. This activity is characterized by very slow ($< 0.1\text{Hz}$) fluctuations of the fMRI Blood Oxygen Level Dependent (BOLD) signal ([Gusnard et al., 2001](#); [Greicius et al., 2003](#)). Separate and possibly remote cerebral regions have been shown to exhibit coherent activity patterns, which collectively form what is called *functional connectivity* (FC). This notion has been previously introduced in defi-

nition 2.1.1, and it is classically measured by the *correlation* between regional fMRI BOLD time series, as pointed out in Chapter 2. It has been shown that FC is organized in robust resting-state networks (Beckmann et al., 2005; Damoiseaux et al., 2006; Moussa et al., 2012), and has been used to explore a range of properties such as cognition (Richiardi et al., 2011; Heine et al., 2012), emotions (Eryilmaz et al., 2011), and learning (Bassett et al., 2011).

From an anatomical point of view, the density of white matter tracks linking every pair of cortical regions is encoded in what is called structural connectivity (SC). This connectivity matrix and its multi-scale spatial organization have also been characterized (Sporns et al., 2004, 2005) and linked to brain diseases (Kaiser, 2013; Griffa et al., 2013; Engel et al., 2013) and genetic influences (Jahanshad et al., 2013; Ziegler et al., 2013).

The relationship between SC and FC, and more particularly the way cerebral anatomy shapes neuronal functions is a question that has been addressed ever since neuroimaging techniques allowed to collect both structural and functional information (e.g. McIntosh and Gonzalez-Lima, 1994). Different approaches have been used to tackle this question, such as direct comparison of functional and structural connectivities (Kötter and Sommer, 2000; Sporns et al., 2000), graph theory (Passingham et al., 2002; Bullmore and Sporns, 2009a), and model based approaches to explain the link between SC and FC (Koch et al., 2002). However, it is only recently that a clear link between SC and FC (Honey et al., 2009; van den Heuvel et al., 2009)[reviewed in Damoiseaux and Greicius (2009)] has been established, allowing for testable models (Honey et al., 2010; Deco et al., 2012).

Meanwhile, the classical approach of assuming FC as constant during resting-state recordings (Bullmore and Sporns, 2009a; Friston, 2011) has also evolved recently, as pointed out in the concluding remarks of Chapter 2. We will refer to this assumption as a *static* analysis of FC that treats FC as a static quantity, averaging FC over the entire time series. In contrast, many recent studies have emphasized the importance of considering the fluctuations of FC (Hutchison et al., 2013; Park and Friston, 2013). Different tools have been proposed to introduce temporal variations into the analyses of FC, such as sliding windows (Sakoğlu et al., 2010; Bassett et al., 2011; Shirer et al., 2012; Allen et al., 2012; Handwerker et al., 2012), dynamic conditional correlation (Lindquist et al., 2014), single-volume co-activation patterns (CAPs) (Tagliazucchi et al., 2012; Liu and Duyn, 2013; Amico et al., 2014), as well as a combination of sliding windows and other methods, such as Independent Component Analysis (Kiviniemi et al., 2011) or Principal Component Analysis (Leonardi et al., 2013). For a review of these methods, see (Hutchison et al., 2013).

Using a temporal framework various studies have further shown that temporal FC (tFC) can be seen as the transition between several FC patterns (Gao et al., 2010; Deco et al., 2013a; Yang et al., 2014) presenting varying network properties (Lv et al., 2013; Sidlauskaitė et al., 2014; Gollo and Breakspear, 2014; Shen et al., 2015). The level of variation,

or flexibility of tFC between specific cerebral regions has also been studied (Bassett et al., 2011; Allen et al., 2012; Gonzalez-Castillo et al., 2014), as well as the role of anatomy in these fluctuations (Gollo et al., 2015) in the macaque cortex.

Finally, many groups have explored day-dreaming, or mind wandering using functional imaging. The networks implied in these processes are mainly the default mode network (Kucyi and Davis, 2014; Fox et al., 2013), the executive control network (Christoff et al., 2009) as well as their interplay (Hasenkamp et al., 2012). The temporal properties of mind wandering have also been studied and characteristic frequencies on the order of 0.03-0.05 Hz were found (Bastian and Sackur, 2013; Vanhaudenhuyse et al., 2011).

The first part of this work addresses the issue of selecting a proper time window, leading to confirmatory, yet original and independent results (Allen et al., 2012; Hutchison et al., 2013; Leonardi and Van De Ville, 2015). Next, motivated by recent work on the temporal functional connectivity repertoire (Yang et al., 2014; Sidlauskaitė et al., 2014) and the influence of the underlying architecture on the flexibility of tFC (Gollo et al., 2015), we explore the role of anatomy in the shaping of different FC patterns, the transition between these states, and their structure. To this end, we compute the temporal correlation between SC and tFC using the appropriate sliding window width and test whether the level of SC-tFC correlation influences tFC variability or the organization of FC patterns. Based on spatiotemporal arguments, we finally discuss the possible interpretation of the SC-tFC fluctuations in terms of consciousness-related processes.

3.2 Material and methods

3.2.1 Participants

Data was collected from 14 healthy volunteers (age range 45 ± 7 years, 7 women, all right-handed). Volunteers gave their written informed consent to participate in the study, which was approved by the Ethics Committee of the Faculty of Medicine of the University of Liège.

3.2.2 Diffusion Weighted Imaging

DWI acquisition Data was acquired on a 3T head-only scanner (Magnetom Allegra, Siemens Medical Solutions, Erlangen, Germany) operated with the standard transmit-receive quadrature head coil. A high-resolution T1-weighted image was acquired for each subject (3D magnetization-prepared rapid gradient echo sequence, field of view = $256 \times 240 \times 120$ mm 3 , voxel size = $1 \times 1 \times 1.2$ mm). A single unweighted ($b = 0$) volume was acquired followed by a set of diffusion-weighted ($b = 1000$) images using 64 non-colinear directional gradients. This sequence was repeated twice for a total of 130 volumes.

Processing The processing pipeline was developed in Nipype ([Gorgolewski et al., 2011](#)) and has been described in more detail previously ([Ziegler et al., 2013](#)). Structural MR images were first segmented using the automated labeling of Freesurfer ([Desikan et al., 2006](#)). Segmented structural images were then further parcellated using the Lausanne2008 atlas for a total of 1015 regions of interest (ROIs) ([Cammoun et al., 2012; Hagmann et al., 2008](#)). Diffusion-weighted images were aligned using FSL to the initial unweighted volume to correct for image distortions arising from eddy currents ([Smith et al., 2004](#)). Fractional anisotropy maps were generated, and a small number of single-fiber (high FA) voxels were used to estimate the spherical harmonic coefficients of the response function from the diffusion-weighted images ([Tournier et al., 2004, 2007](#)). Using non-negativity constrained spherical deconvolution, fiber orientation distribution (FOD) functions were obtained at each voxel. For our dataset with 64 directions, we used the maximum allowable harmonic order of 8 for both the response estimation and spherical deconvolution steps. Probabilistic tractography was performed throughout the whole brain using seeds from subject-specific white-matter masks and a predefined number of tracks ([Tournier et al., 2012](#)).

Fiber tracking settings were as follows: number of tracks = 300,000, FOD amplitude cutoff for terminating tracks = 0.1, minimum track length = 10 mm, maximum track length = 200 mm, minimum radius of curvature = 1 mm, tracking algorithm step size = 0.2 mm.

Using tools from Dipy (Diffusion in Python, <http://nipy.sourceforge.net/dipy/>), the tracks were affine-transformed into the subject's structural space and connectome mapping was performed by considering every contact point between each tract and the outlined regions of interest ([Ziegler et al., 2013](#)).

3.2.3 Functional data

BOLD acquisition Three hundred multi-slice T2*-weighted functional images were acquired with a gradient-echo echo-planar imaging sequence using axial slice orientation and covering the whole brain (32 slices; voxel size: $3 \times 3 \times 3 \text{ mm}^3$; matrix size $64 \times 64 \times 32$; repetition time = 2000 ms; echo time = 30 ms; flip angle = 78°; field of view = $192 \times 192 \text{ mm}^2$). The three initial volumes were discarded to avoid T1 saturation effects.

Processing fMRI data preprocessing was performed using Statistical Parametric Mapping 8 (SPM8; www.fil.ion.ucl.ac.uk/spm). Preprocessing steps included slice-time correction, realignment and adjustment for movement-related effects, coregistration of functional onto structural data, segmentation of structural data, spatial normalization into standard stereotactic Montreal Neurological Institute (MNI) space, and spatial smoothing with a Gaussian kernel of 8 mm full width at half-maximum. Further motion correction

was applied using ArtRepair toolbox for SPM¹ which corrects for small, large and rapid motions, noise spikes, and spontaneous deep breaths. Finally, linear regression of mean global BOLD signal, mean ventricular BOLD signal and mean white matter BOLD signals from each voxel was performed. Even if it is still a debated question it could be argued that global signal regression (Macey et al., 2004) could induce spurious correlations in our analysis (e.g. Murphy et al., 2009). However, it has been shown in Honey et al. (2009) that global signal regression is an important step in order to better reveal the correlation between structural and functional connectivities. Since this SC-FC link is the main focus of this work we regressed out the global signal.

The timecourse for each region-of-interest was extracted by taking the average signal over all voxels in each ROI defined following the same parcellation procedure as for anatomical data.

3.2.4 Sliding Window for FC Analysis

In order to explore the fluctuations of the correlations between structural and functional connectivities we repeated the computation of the FC matrices from truncated portions of the fMRI time series, as previously presented (Chang and Glover, 2010; Hutchison et al., 2012; Allen et al., 2012; Leonardi et al., 2013). However, it has been shown recently that spurious correlations can arise from this classical approach when short windows are used. To limit this confound, we high-pass filtered the fMRI time series with a cutoff frequency of $1/w$, where w is the width of the truncated portions (Leonardi and Van De Ville, 2015; Zalesky and Breakspear, 2015).

Denoting by N the number of volumes in the fMRI time series and considering a window width w , we computed $N - w + 1$ successive FC matrices from the truncated fMRI time series in each particular window, each one being shifted forward by one TR with respect to the previous one as shown in Figure 3.1 *right*.

We used window widths ranging from 5 to 100 volumes, corresponding to 10 to 200 seconds, to explore the fluctuations between structural and functional connectivities.

3.2.5 Temporal correlation between structural and functional matrices

We then computed the correlation between all the FC matrices and the SC matrix (Figure 3.1 *right*). This included, as in Honey et al. (2009), log-rescaling of the non-zero values in the SC matrix such that the range in both matrices have the same order of magnitude.

¹ <http://cibsr.stanford.edu/tools/human-brain-project/artrepair-software.html>

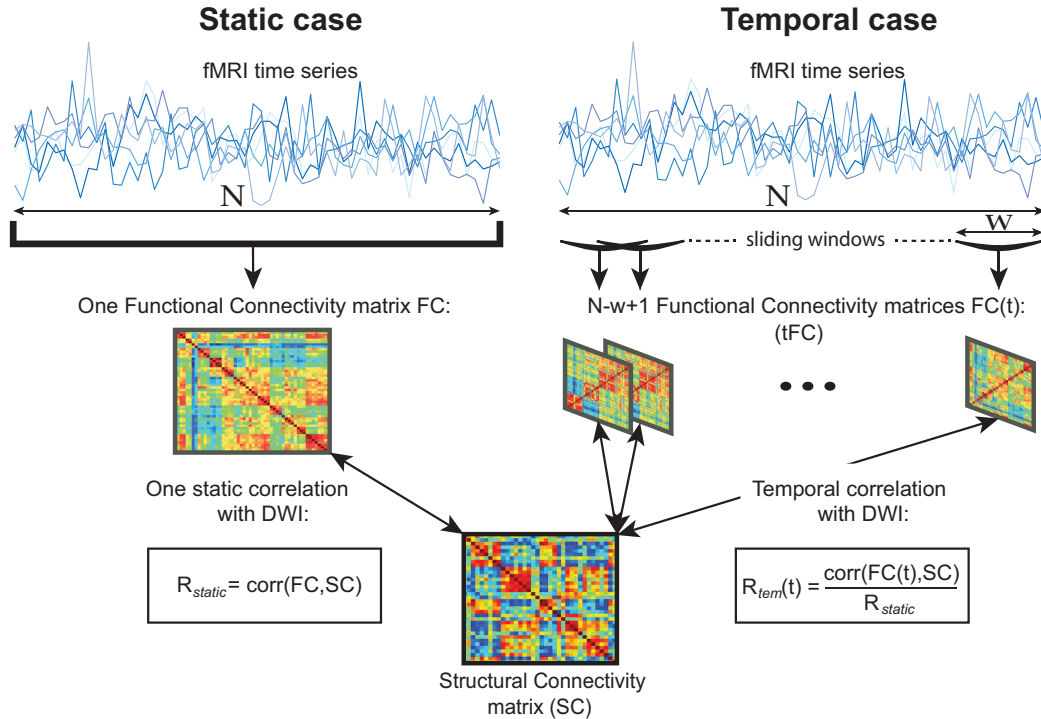


Figure 3.1 – Comparison between the static and the temporal analysis of the correlation between structural and functional connectivities (SC and FC, resp.). *Left* In the static case FC is computed using the whole fMRI time course. The static correlation R_{static} between SC and FC, is then computed as in e.g. Honey et al. (2009). *Right* In the temporal case tFC is computed in windows of the fMRI time courses that are slid across the whole fMRI time course. The temporal correlation used in the present work $R_{temp}(t)$ between SC and FC(t) is then computed and normalized by R_{static} and R_{temp} is a vector of size $N - w + 1$.

In order to facilitate inter-subject comparisons, the evolution of this correlation was normalized by the *static correlation* between the SC and the FC matrices computed using the whole fMRI time series (Figure 3.1 bottom right), resulting in what we call the *temporal correlation*, denoted by $R(t)$.

In order to characterize the fluctuations of the temporal correlation the power spectrum of $R(t)$ was computed using Welch's method (Welch, 1967) and normalized in order to have $\int_0^{0.25} P(f)dF = 1$ where $P(f)$ is the power spectral content corresponding to frequency f .

3.2.6 Values of interest

In order to characterize fluctuations observed in the time-evolving *temporal correlation* curves and their corresponding spectral power, we used two markers:

- V is the range of variation in the *temporal correlation*, computed as the difference between its maximal and minimal value, in percent. V is used to highlight the phases of (de)synchronization between SC and FC (Fig 3.2A),
- F^* is the frequency of maximal relative spectral power (in Hz), and corresponds to the main oscillatory mode of a time course, such as presented in Figure 3.2B.

3.2.7 Statistical significance of the observed fluctuations

A key challenge in fMRI time series analyses is disentangling the neuronal fluctuations from noise (Handwerker et al., 2012). To this end we performed the same computations as the one described in Figure 3.1 using surrogate data obtained by *phase randomization* in the Fourier domain of the fMRI volumes (Theiler et al., 1992), similar to what is presented in Allen et al. (2012), for example. Doing so leaves the *static correlation* unchanged because the overall covariance structure is preserved, whereas the evolution of the temporal correlation $R(t)$ using windowing will be totally rearranged. More specifically, the mean, the variance and the temporal autocorrelation of the time series are preserved but the information contained in the ordering of the fMRI volumes is destroyed.

We observed larger fluctuations (higher V) of $R(t)$ in the original data compared to the surrogate data. Hence, we chose this marker to test for differences between the results obtained with ordered and phase-randomised fMRI time series. For each value of window width and each subject we did 1000 permutations (see e.g. Chap 3.5 in Edgington and Onghena, 1969) and computed the z-score corresponding to the following null hypothesis:

$$\mathcal{H}_0 = \{V_{ord} \geq V_{rand}\}$$

where V_{ord} (resp. V_{rand}) is the range of variation of $R(t)$ in the original ordered (resp. surrogate) data.

The group level significance curve presented in Figure 3.4B was computed from the z-scores of all the subjects. This technique is known as the Stouffer's method (Stouffer et al., 1949), and allows for the combination of z-scores from several independent tests bearing upon the same group-level hypothesis. In our case, we proceeded as follows:

1. Compute the z-score corresponding to the null hypothesis for each subject and each window, denoted by $Z_i, i \in \{1\dots14\}$,
2. Compute the z-score for each window width at the group-level analysis Z_G as follows:

$$Z_G = \frac{\sum_{i=1}^{N_s} Z_i}{\sqrt{N_s}},$$

where N_s is the number of subjects.

3.2.8 Graph theory metrics

In order to further characterize FC during the phases of (de)synchronization with SC, we used three common graph metrics of FC considered as a weighted undirected graph ([Bullmore and Sporns, 2009a](#)).

In this context, each ROI is considered as a *node* of the graph and the absolute value of the correlation between each two regions i and j , $\text{abs}(FC_{i,j})$, is the weight of the *edge* connecting these two regions. Since FC is symmetric, it follows that the corresponding graph is undirected. We used the three following metrics on the whole FC matrices:

- *Density* is the number of total connections divided by the number of possible connections ([Sporns, 2002](#)),
- *Efficiency* measures how 'close' each pair of nodes are in the graph. It is inversely related to the characteristic path length ([Onnela et al., 2005; Rubinov and Sporns, 2010](#)),
- *Modularity* quantifies to which degree a network can be subdivided into distinct groups ([Newman and Girvan, 2004](#)).

The Brain Connectivity Toolbox ([Rubinov and Sporns, 2010](#)) was used to evaluate the value of these three markers during phases of high and low correlation between SC and $FC(t)$.

For each subject, averaged top and bottom 5% of $FC(t)$ matrices were selected, sorted by $R(t)$ value. Since density was designed for binary graphs, we binarized the functional connectivity matrices (only for this metric) by considering only the *significant* correlations as defined by [Leonardi and Van De Ville \(2015\)](#), which corresponds in our case to a threshold of 0.44.

It should be noted that the choice of these thresholds does not influence the trend observed in results presented in Figure 3.6 as shown in Figure A.3.

For illustration purposes, ROIs belonging to auditory (AUD), somatomotor (SM), visual (VIS), cognitive control (CC), default-mode (DM) were gathered in networks following the

same grouping as in [Allen et al. \(2012\)](#) in order to highlight the modular and diagonal structures of the connectivity matrices.

3.2.9 ROI-level structural and functional contributions

All computations above have been performed at the whole-brain level. In order to explore the contribution of each of the 1015 regions to the brain level SC-FC fluctuations, for each ROI we computed the temporal correlation $R(t)$ (window width $w = 20$ TR = 40 sec) between SC and FC by considering only the connections implying this ROI.

We then computed the range of variation V of $R(t)$ as defined previously and computed the average variation over all subjects for each ROI. We finally also computed the average degree over the subjects of the corresponding regions of the structural connectivity matrix, which is plotted as a function of the averaged value of V in Figure 3.7B.

3.3 Results

3.3.1 Statistical significance of temporal correlation

The temporal correlation for a representative subject is shown in Figure 3.2 for a window width = 20 TR = 40 sec.

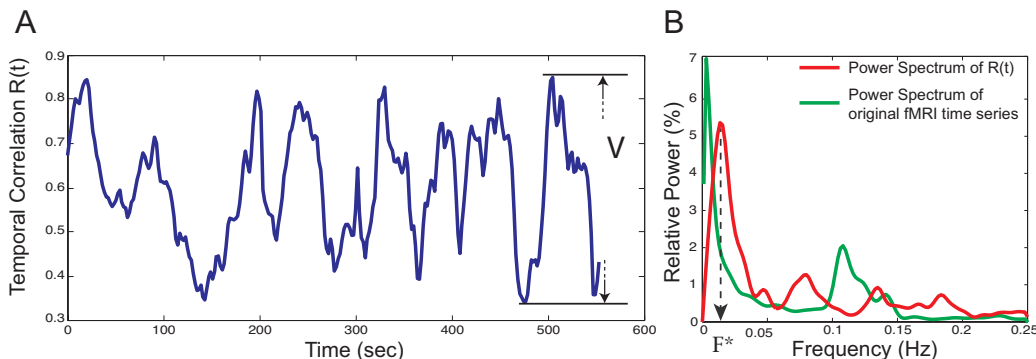


Figure 3.2 – (A) Temporal correlation between SC and FC. (B) Corresponding power spectra. Results are shown for a representative subject and a window width of $w = 13\text{TR}$. The static correlation $R_{static} = 41.2\%$, $V = 53.2\%$ and $F^* = 0.013\text{Hz}$. The fMRI time series average spectrum for the same subject is also plotted for comparison.

In this example the temporal correlation varies from 34% to 87% ($V = 53\%$) of the static correlation, and the main oscillatory mode is $F^* = 0.013\text{Hz}$. We illustrate in Figure 3.3 the impact of the window width w for selected values of w .

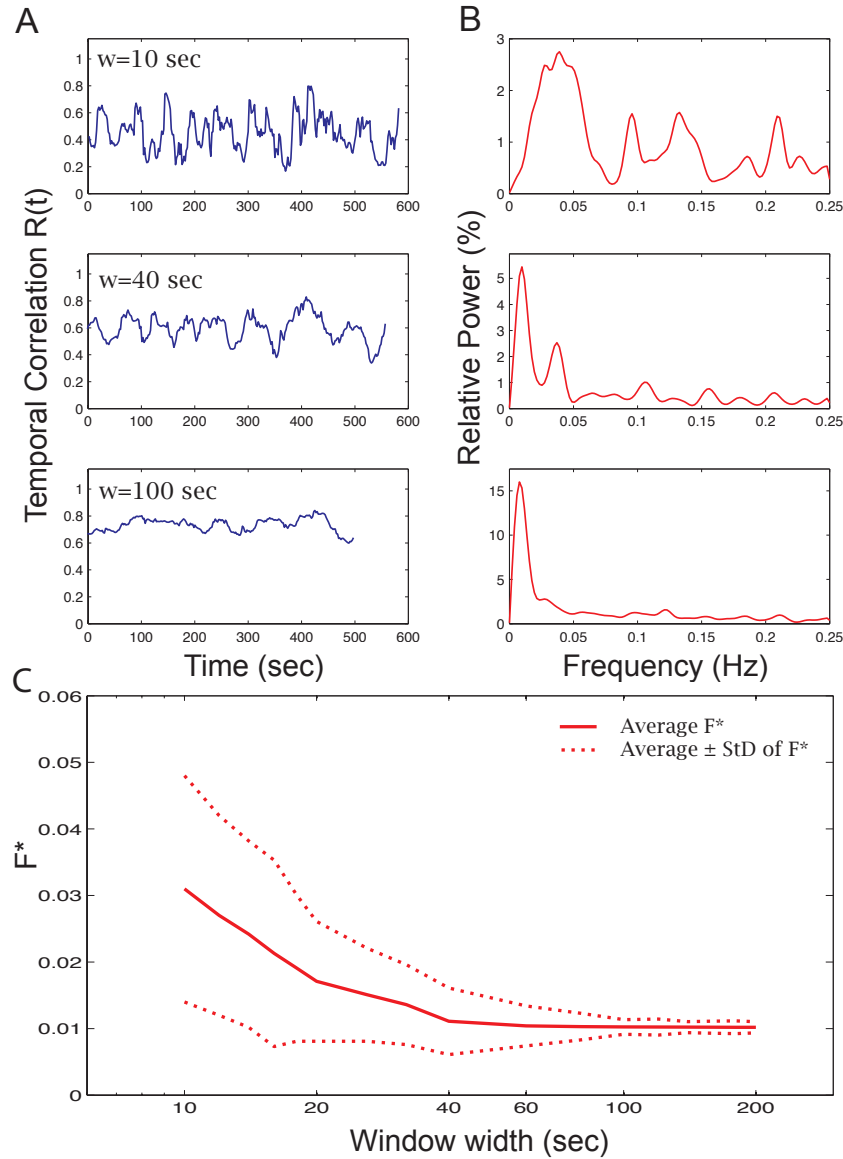


Figure 3.3 – (A) $R(t)$ and (B) corresponding power spectrum for different window widths w and for a representative subject. (C) Mean and standard deviation of F^* for all subjects as a function of the window width w .

We observe that increasing w results in smoothing of the temporal correlation curve (Figure 3.3A). This can also be observed in the power spectrum, which is globally shifted towards low frequencies when w increases (Figure 3.3B), resulting in a decrease of F^* for higher values of w (Figure 3.3C). In order to assess the significance of observed fluctuations, comparison against phase-randomised fMRI time series as explained in the Methods section. The group-level results are presented in Figure 3.4.

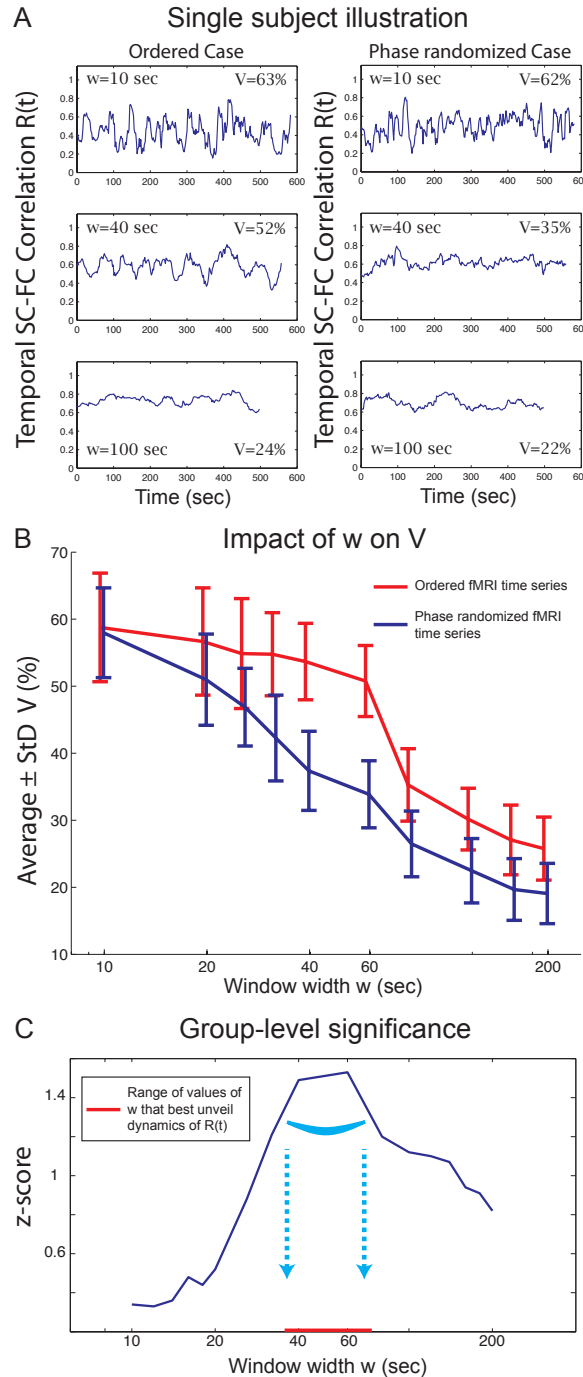


Figure 3.4 – (A) $R(t)$ for different window widths for a representative subject in the original dataset and one sample of the surrogate dataset. (B) Impact of the window width w on V at the group level, in ordered and phase-randomised time series. (C) Estimation of the statistical significance region at the group level based on V .

Figures 3.4A,B illustrate the fact that the difference between ordered and phase randomised fMRI time series as captured by V is more pronounced for intermediate values of w . At the group level, a peak of statistical significance can be observed around $w = 20\ TR = 40\ sec$ (Figure 3.4C) hence this is the window width that we will use in the following analyses.

It should be noted that the value of V increases with the total length of the fMRI time series but stabilizes once this length is above 200-300 sec. Hence, with a total acquisition time of 600 sec the value of V is stable and the group-level curve presented in Figure 3.4C is robust to changes in the recording time period (results not shown here).

3.3.2 Phases of (de)synchronization between functional and structural connectivities

We show in Figure 3.5 the average patterns of $FC(t)$ computed during phases corresponding to 5% highest and lowest value of $R(t)$ as well as the constant structural connectivity matrix, for one particular subject.

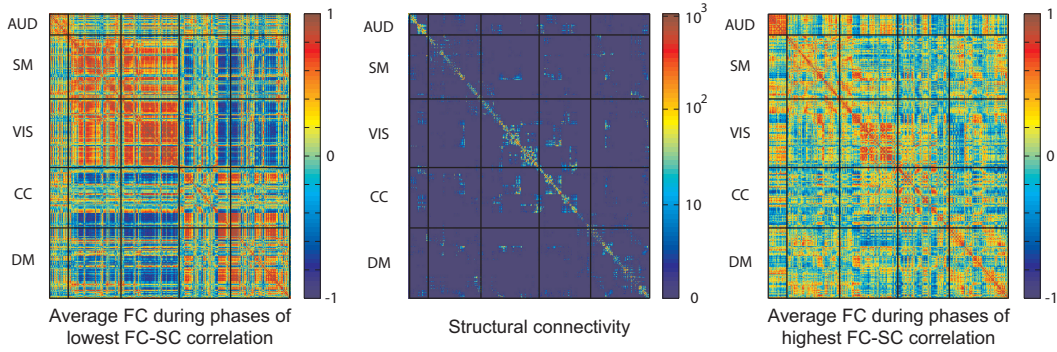


Figure 3.5 – left Average FC matrix computed by averaging the FC matrices that have the 5% lowest correlations with SC for the same subject and $w = 20\ TR = 40\ sec$. **middle** Structural connectivity matrix. **right** Average FC matrix computed by averaging the FC matrices that have the 5% highest correlations with SC. Auditory (AUD), somatomotor (SM), visual (VIS), cognitive control (CC), default-mode (DM) networks are grouped in order to highlight the modular and block diagonal structure of connectivity matrices as in [Allen et al. \(2012\)](#).

Density, efficiency and modularity of the high and low FC patterns for all the subjects are represented in Figure 3.6.

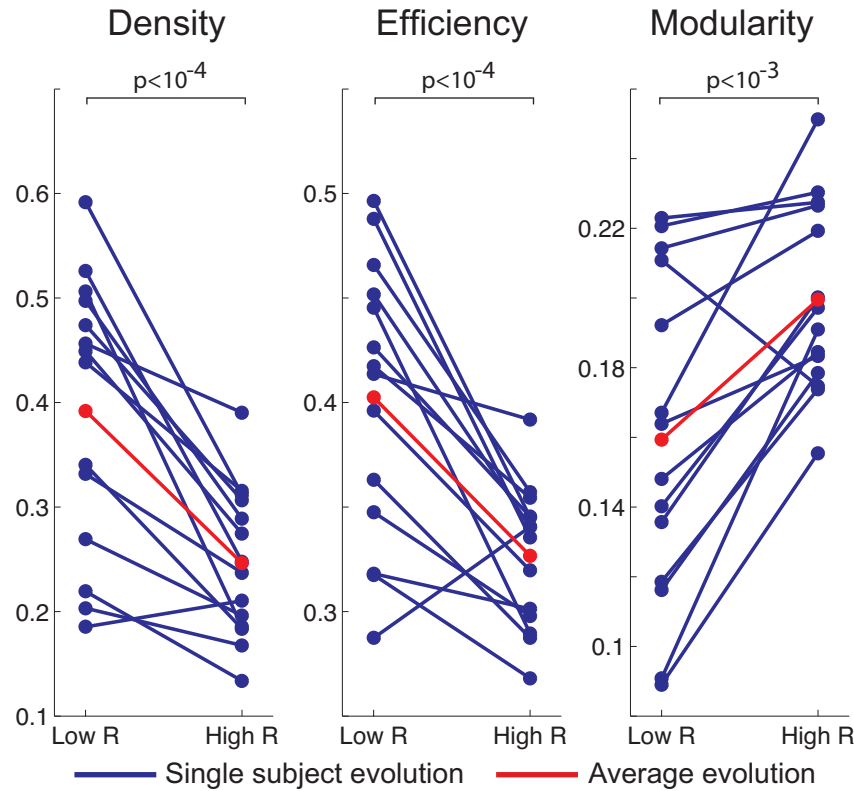


Figure 3.6 – Density, Efficiency and Modularity of FC averaged over the 5% lowest correlations with SC (low R - left columns) and FC averaged over the 5% highest correlations with SC (high R - right columns) for all the subjects. The group mean is represented in red.

Density and efficiency appear to be significantly lower ($p < 10^{-4}$ and $p < 10^{-3}$ using a paired t-test) when the correlation between $FC(t)$ and SC is high whereas modularity increases at the same time ($p < 10^{-3}$).

3.3.3 ROI-level analysis

The average range of variation V of $R(t)$ in the 1015 regions of interest are represented in Figure 3.7A and the impact of the average degree of structural connectivity on V is represented in Figure 3.7B.

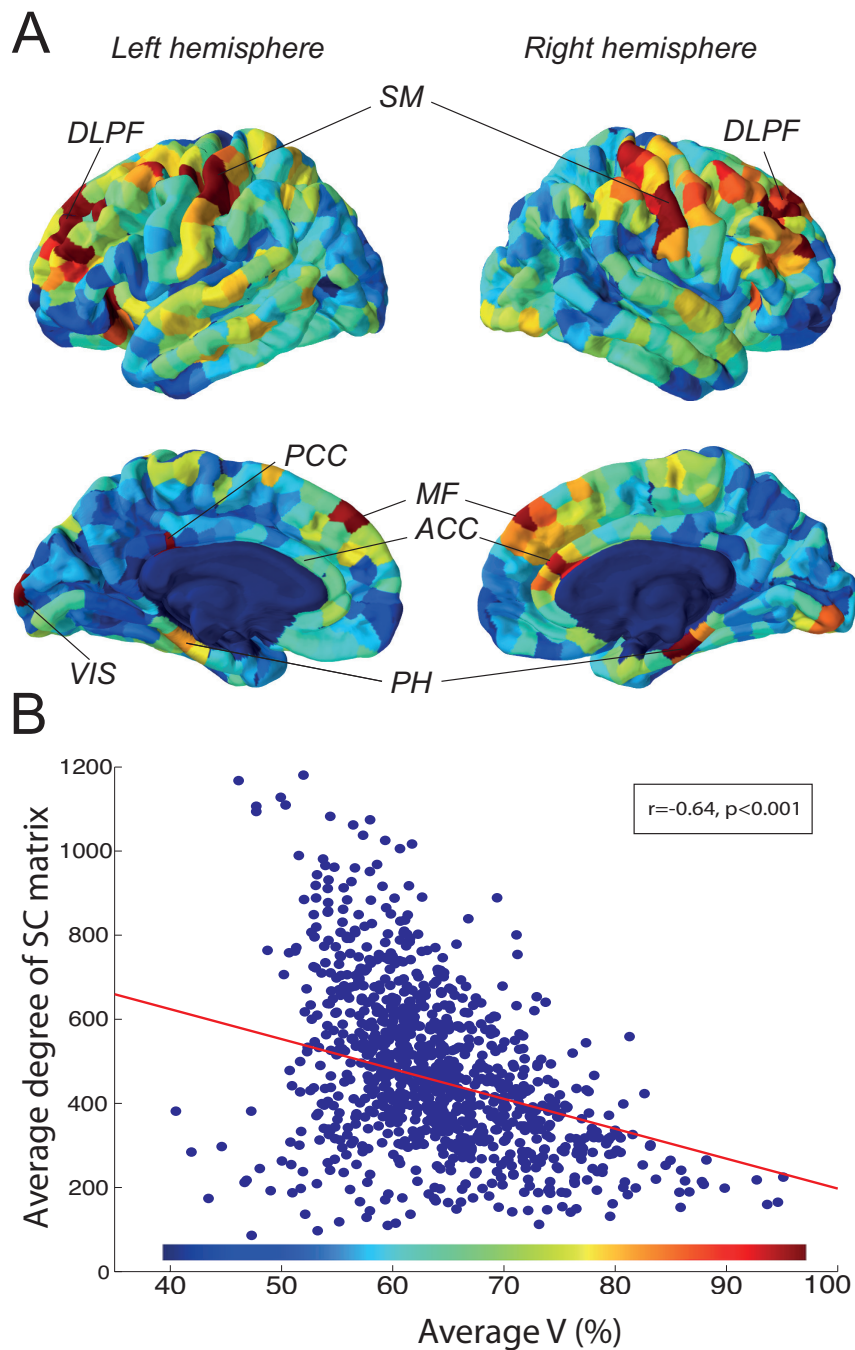


Figure 3.7 – (A) Average V in each ROI for $w = 40$ sec and corresponding distribution. *DLPF*: dorso-lateral prefrontal cortex; *SM*: sensory-motor cortex; *PCC*: posterior cingulate cortex; *MF*: mesio-frontal cortex; *ACC*: anterior cingulate cortex; *PH*: parahippocampal cortex; *VIS*: visual cortex. (B) Link between average degree of SC matrix and average V.

The regions with the highest values of V are the ones that most contribute to the whole-brain level behaviour presented in Figure 3.4C. These areas encompass bilateral anterior cingulate, mesio-frontal, posterior cingulate, temporo-parietal and para-hippocampal gyri that overlap with the default mode network while the bi-lateral dorso-lateral pre-frontal cortices are part of the executive control network (See Discussion for details). Note that also peri-rolandic sensory-motor and occipital visual sensory cortices showed a high range of variation of $R(t)$.

Moreover, there is a significant negative correlation of -0.64 between the degree of the connectivity matrix and the value of V , averaged over the subjects.

3.4 Discussion

3.4.1 A) Significance of fluctuations of $R(t)$ observed using the sliding window approach

Sliding window techniques have been widely used in recent studies in order to analyze FC fluctuations. [Allen et al. \(2012\)](#) used a width of 22 TR (TR=2 sec) to track oscillations in FC fluctuations, [Shirer et al. \(2012\)](#) showed that considering a width above 15-30 TR (TR=2 sec) allows for robust estimation of the FC without considering fluctuations. More recently, [Leonardi et al. \(2013\)](#) used widths ranging from 20 to 120 TR (TR=1.1 sec) and observed different “eigenconnectivity patterns” depending on the window that was used and [Hutchison et al. \(2012\)](#) also found different results with window widths going from 10 to 120 TR (TR=2 sec).

Our study reveals a peak of statistical significance in the observed fluctuations around $w = 20 - 30$ TR (TR=2 sec) for which w is sufficiently large to robustly estimate functional connectivity matrices and sufficiently small to capture corresponding fluctuations. This results from a general tradeoff in time series analyses: longer windows improve the estimation of the correlation but mask the fluctuations because they act as low-pass filters with cutoff frequency f_c that decreases when w increases ([Smith, 1997](#); [Lindquist et al., 2014](#); [Leonardi and Van De Ville, 2015](#)) and hence we can interpret the results of Figure 3.4B as the combination of these two effects as represented in Figure 3.8.

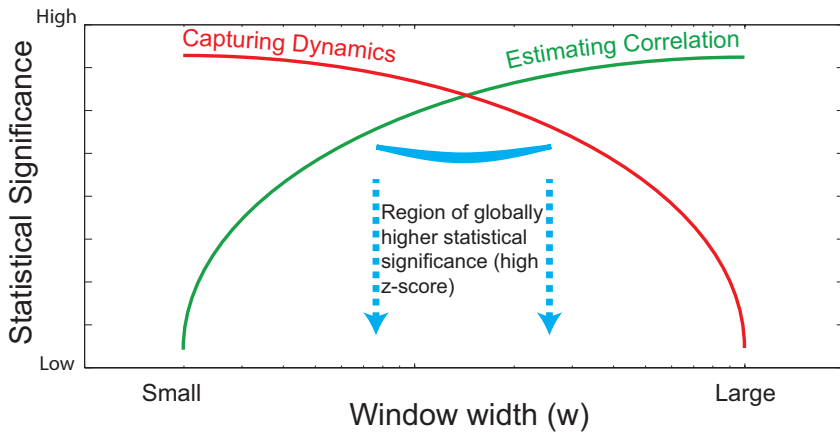


Figure 3.8 – Interpretation of results presented in Figure 3.4C: tradeoff between capturing fluctuations and estimating correlation.

The first effect illustrated by the green curve in Figure 3.8 and corresponding to the estimation of functional connectivity was studied by [Shirer et al. \(2012\)](#). They show based on a classification experiment that using windows larger than 15-30 TR (TR = 2 sec) allows for correct estimation of functional connectivity information, which is consistent with our findings. Our analysis provides the additional insight that considering higher values of w does not capture the FC neuronal fluctuations, which is illustrated by the red curve in Figure 3.8.

The peak in the ability to capture FC fluctuations was observed using the *range of variation* (V) of $R(t)$ and another statistical test based on the *variance* of the $R(t)$ curves (see Figure A.1) also shows a peak for values of w around 20 TR. Even if it is not surprising to find similar effects using variance instead of the range of variation, this confirms our conclusions about which window width should be used.

Hence, we believe that the significance testing framework proposed in the present work is a simple way to find a window width w that both allows for robust estimation of FC matrices and captures the corresponding fluctuations. In addition, since this test is based on a comparison against phase-randomised time series, it could also be used to improve the interpretation of observed functional connectivity fluctuations and the delicate distinction from noise with similar properties ([Hutchison et al., 2013](#)).

Let us finally note that the high-pass filtering preprocessing step with cutoff frequency of $1/w$ of the fMRI time courses performed following [Leonardi and Van De Ville \(2015\)](#) removes a large part of the original signal for small window widths. This may also explain why, for small values of w , the significance of the variations of $R(t)$ is poor (Figure 3.4C). When w increases in the range of 40-60 sec, the effect of the high-pass filtering becomes

milder and the neuronal information expected to be encoded around 0.1 Hz is not filtered out leading to more significant fluctuations of $R(t)$. Finally, for higher values of w , the fluctuations of $R(t)$ are averaged and their statistical significance drops.

Limitations

The sliding window acts as a low-pass filter. In our case, considering $w = 20$ TR = 40 sec results in a cutoff frequency $f_c \approx 0.02$ Hz ([Smith, 1997](#), Chap.15). Hence, a robust estimation of FC, which requires a window width $w \approx 20$ TR, necessarily filters out the FC fluctuations happening at higher frequencies than ≈ 0.02 Hz.

This limitation should be taken into account when interpreting results of temporal FC analyses using sliding windows. In particular, it should be highlighted that having a main oscillatory mode at around 0.01 Hz (Figure 3.3C) for the values of w that are statistically significant does not mean that the fluctuations are only occurring at these frequencies. As explained earlier, hypothetical fluctuations happening at higher frequencies are filtered out when we use 20 TR (40 sec) windowing.

This is also a call for more advanced identification methods for estimating correlation, pushing the green curve of Figure 3.8 to the smaller window widths, consequently freeing access to higher frequency fluctuations.

Finally, it is interesting to note that we were not able to distinguish ordered from phase-randomised time courses using F^* (see Figure A.2), suggesting that F^* is imposed by the sliding window method and by w (Figure 3.3C) and is not *a priori* capturing neuronal fluctuations. It is therefore not surprising to find similar values of F^* in studies using a similar window width: [Allen et al. \(2012\)](#) found oscillations at 0.005-0.015 Hz using a 22 TR (44 sec) windowing. However, as argued in [Hutchison et al. \(2013\)](#), this does not imply that the value of F^* for ordered fMRI time series has a non-neuronal origin, which is why we decided to continue considering this marker, while remaining aware of this caveat.

3.4.2 B) Phases of (de)synchronization between functional and structural connectivities

The link between structural and functional connectivities was established a few years ago ([Honey et al., 2009](#); [van den Heuvel et al., 2009](#)). Thereafter, a lot of interest has been devoted to deepening the understanding of how anatomical constraints shape functional connectivity ([Honey et al., 2010](#); [Breakspear et al., 2010](#); [Cabral et al., 2011](#); [Deco et al., 2012](#)), and how this relationship can be affected by different pathologies ([de Kwaasteniet et al., 2013](#); [van Schouwenburg et al., 2013](#)).

In most of these studies either the fluctuations of FC are not taken into account, or it is modeled, but the information coming from the data and used to assess models is deduced with a static approach of FC (e.g. [Deco et al., 2013b](#)).

To our knowledge, this work is the first purely data-driven attempt to study the temporal relationship between SC and FC. More specifically, we show in Figure 3.4 that there are statistically significant (i.e. resulting from the neuronal fluctuations, not noise) phases of (de)synchronization between the functional correlation and the anatomical constraints. When using statistically significant values of w such as $w = 20$ TR, the range of variation V is on the order of 52% of the static correlation, compared to 35% in the randomised case, meaning that the correlation between FC and SC is significantly increased at some points and significantly decreased at some other points.

Structure guides transitions between functional brain states

Many studies have recently highlighted the presence of different and successive functional connectivity states, even at rest ([Lv et al., 2013](#); [Gao et al., 2010](#); [Deco et al., 2013a](#); [Yang et al., 2014](#); [Sidlauskaitė et al., 2014](#)). The results shown in Figures 3.5 and 3.6 suggest that the temporal reorganization of functional connectivity patterns is at least partly shaped by anatomy. More particularly, it can be observed in Figure 3.6 that phases of high correlation between FC and SC correspond to functional connectivity patterns that have low efficiency and high modularity. The interpretation is that during these phases the brain is poorly functionally connected, and organized in modules shaped by anatomy with few inter-module connections ([Newman and Girvan, 2004](#)). On the other hand, during phases of low correlation between FC and SC, the number of inter-module functional connections increases, resulting in highly connected FC patterns.

Very recently, [Messé et al. \(2014\)](#) demonstrated a decoupling between anatomically defined networks and other networks resulting from stationary and non-stationary FC fluctuations, but not related to anatomy. Combined with our results, these observations lead us to propose that anatomy could periodically play the role of a relay that guides switches between different highly connected FC patterns not shaped by anatomy (low value of $R(t)$), alternating with phases of lower efficiency and higher modularity, defined by SC architecture (high value of $R(t)$). Whereas we can consider the latter as similar modes of the tFC repertoire highly defined by structure, the FC patterns corresponding to low values of $R(t)$ may cover a much larger repertoire of FC modes, as previously observed ([Gollo and Breakspear, 2014](#); [Shen et al., 2015](#)), leading to a wider distribution of the graph metric values in Figure 3.6. This interpretation echoes recent work ([Zalesky et al., 2014](#)) in which the connections showing the largest fluctuations are shown to be inter-modular, and support the emergence of temporary phases of high functional efficiency.

More generally, the spatial distribution of the level of fluctuation of tFC (Allen et al., 2012) and its link with cognitive tasks (Bassett et al., 2011) have also been explored. Interestingly, the anterior cingulate cortex, part of the DMN, was consistently identified as a region showing large tFC variability, coherently with the results presented in Figure 3.7A. However, there does not seem to be a clear global correspondence between the regions identified in these studies and the ones identified here. One possible explanation for this might be the bias introduced in this work by the projection of tFC onto the underlying anatomical structure leading to a partial picture of tFC fluctuations.

Furthermore, the results shown in Figure 3.7B suggest that the level of the fluctuations is strongly influenced by the underlying anatomy, possibly explaining why the most stable functional connections are observed between symmetric inter-hemispheric ROIs, expected to be more densely connected, whereas the most variable connections are found between non-symmetric inter-hemispheric regions (Gonzalez-Castillo et al., 2014).

R(t) as a footprint of resting-state mentation ?

Our understanding of the physiological and cognitive meaning of FC as measured by resting-state fMRI is limited and controversial (e.g. Lamme, 2003; Vincent et al., 2007). Hence the interpretation of the fluctuations of R(t) remains speculative but we propose that they could be related to task-independent thoughts as classically reported during resting-state fMRI studies encompassing mind wandering, day-dreaming, inner speech and mental imagery (for a review see Lieberman (2007)). Indeed, growing neuroscientific evidence supports that these conscious mentation processes (Goldberg et al., 2006) are supported by the interplay between a default mode network (or internal awareness network) involved in self-related processes (Fox et al., 2005) with an external awareness network called the executive network (Vanhaudenhuyse et al., 2011).

We now argue based on temporal and spatial arguments that R(t) fluctuations could be related to these mentation processes.

First, the temporal fluctuations of our observed R(t) possess a main oscillatory mode in the range 0.01 ± 0.003 Hz (Figure 3.3C). It is interesting to note the overlap with the so-called "periodic shifts" (Vanhaudenhuyse et al., 2011) from external to internal awareness of behavioural scores observed in healthy volunteers in resting-state fMRI conditions occurring with a frequency of 0.05 Hz (range 0.01 – 0.1 Hz). However, this argument has to be considered cautiously because the fluctuations in spontaneous cognitive activity are known to show substantial variability at the individual subject level (Fox et al., 2007) and as indicated above we were not able to show that the frequency of the main oscillatory mode results from neuronal fluctuations.

Next, with regards to the spatial characteristics of the intensity of oscillations in $R(t)$, our results presented in Figure 3.7 show that the identified bilateral anterior cingulate, mesio-frontal, posterior cingulate, temporo-parietal and para-hippocampal gyri overlap with the default mode internal awareness network (e.g. [Kucyi and Davis, 2014](#)) while the bilateral dorso-lateral prefrontal cortices are part of the executive control/external awareness control networks ([Vanhaudenhuyse et al., 2011](#)).

Finally, let us note that these hypotheses could be linked to the previous point of the discussion. Indeed [Doucet et al. \(2012\)](#) reported that mind wandering was correlated with fluctuations of functional modular organization, inner-oriented activities being associated to phases of low inter-module connectivity. This is an additional argument supporting the interpretation of $R(t)$ as reflecting task-independent processes encompassing mind wandering, but that could also be related to spontaneous thoughts ([Buckner and Carroll, 2007](#)) or monitoring of the external world (for review see [Hahn et al. \(2007\)](#)).

3.4.3 C) Future work

The results of this Chapter call for several methodological refinements. Windowing is an approach that shows some limitations, and in our view future studies should consider more advanced techniques for detecting community structure of time-evolving functional networks (e.g. [Bassett et al., 2013](#)). This would allow to further bridge the gap between the temporal fluctuations of FC changes, their underlying static anatomical architecture, and their subjective cognitive counterparts. These alternatives should allow for clearer identification of temporal changes in functional connectivity, and could help unveil processes occurring at higher frequencies, such as mind wandering. As fast scanning becomes feasible with new scanners and parallel imaging, one simple way to test this hypothesis would be to use smaller TRs, up to the sub-second range, in order to increase the low-pass cutoff frequency of the windowing process.

It could also be worth completing the present multi-modal analysis with other imaging modalities such as EEG. It has for example been suggested that EEG micro-states can be considered as building blocks of cognition, and that they shape the networks detectable with resting fMRI ([Van de Ville et al., 2010](#)). Hence, including the high-resolution temporal information provided by EEG measurements could lead to a better understanding of the interaction between anatomy and function and its interpretation in terms of cognitive processes.

3.5 Conclusions

The contribution of the present Chapter is threefold. From a methodological point of view we highlight some characteristics of the sliding window technique to reveal functional connectivity fluctuations. Our results suggest that the width of those windows should be chosen around the 20-30 TR (40-60 sec) range to both provide a robust estimate of tFC and capture significant corresponding neuronal fluctuations. For smaller or larger values, we could not distinguish functional connectivity fluctuations from noise with similar properties, hereby confirming in an independent way previous studies characterising tFC.

Next, we use a suitable window width to show that temporal functional connectivity oscillates between states of high modularity, mostly shaped by structural connectivity architecture, and states of low modularity, not defined - or indirectly defined - by structural connectivity, during which more inter-network connections take place.

Finally, considering that the fluctuations of $FC(t)$ on the anatomical architecture are occurring at a characteristic frequency of ≈ 0.01 Hz and that regions mostly contributing to their fluctuations belong to the default mode or the executive control networks, we propose that they could be related to task-independent processes such as mind wandering.

From a broader point of view, this work also illustrates the difficulty of extracting relevant information from observed FC fluctuations. The projection of the tFC onto structural connectivity resulted in a single time course, $R(t)$, whose temporal properties were presumably easier to analyse and to interpret compared to the initial series of tFC matrices. Still, we had to perform multiple significance testing in order to assess the neuronal origin of the fluctuations of $R(t)$, and the some of the main results presented in this Chapter were obtained by considering the extreme values of $R(t)$, and the corresponding FC matrices. This is obviously a partial analysis of the information encoded in the temporal fluctuations of $R(t)$, or tFC, and in particular it does not provide a well-grounded analysis of the *dynamical* properties of the fluctuations of FC. In the next Chapter, we clarify the distinction between *temporal* approaches, as used in the work presented here, and *dynamical* models of functional connectivity on which we will focus in the following Chapters as they often result in simpler and more interpretable markers of the observed FC fluctuations.

CHAPTER 4

Dynamical measures of functional connectivity

“[...] However, my definition was pragmatic and any applied researcher with two or more time series could apply it, so I got plenty of citations. Of course, many ridiculous papers appeared.”

—Clive W.J. Granger, NOBEL LECTURE, 2003

4.1 Introduction

Chapter 3 presents one simple way to extend a *static* measurement of functional connectivity, as presented in Chapter 2, in order to take into account the fluctuating nature of FC. The corresponding temporal measure of FC captures important information encoded in the original fMRI time series, as already highlighted in e.g. [Allen et al. \(2012\)](#). Following the structure of Chapter 2, we here propose to review other *dynamic* measures of functional connectivity, computed from fMRI time series.

We first discuss the difference between *temporal* and *dynamical* models of functional connectivity. Then, we present the main properties of connectivity encoded by the different dynamical models leading to the classification presented in Figure 4.1. The corresponding models or statistics are also defined and results using these approaches on fMRI data are discussed. We conclude by motivating the methodological choices done in Chapters 5, 6 and 7, considering the outcomes of the present Chapter.

4.2 Temporal vs. Dynamical models

The adjectives “temporal” and “dynamical” are often used in order to describe extensions of the classical *static* modelling of fMRI time series and corresponding functional connectivity. Sometimes, no clear distinction is provided between these terms: for example [Zalesky et al. \(2014\)](#) uses equivalently the expressions “temporal fluctuations” and “dynamic fluctuations” to denote the fluctuations in the brain networks’ organisational properties. We here first make a clear distinction between these two terms as they are in our opinion associated to different analysis approaches.

We use “*temporal*” in order to refer to the *fluctuations over time* of some *statistics*, such as correlation. Different techniques can be used to go from *static* to *temporal* statistics characterising time courses, the most straightforward being sliding windows, as presented in Chapter 3. This approach has in our opinion two main limitations: first, as all local measurements, it is prone to biases due to noise that is important in fMRI time series and can arise from different sources such as breathing, heart beating, or motion ([Hutchison et al., 2013](#)). Then, and most importantly, these measures, as detailed in the conclusion of Chapter 3, do not reduce to simple markers. On the contrary, they considerably increase the amount of information extracted from the time series leading to more complex interpretations.

We reserve the word “*dynamical*” to *models* considering time series composed of N time samples as *processes* of length N . This is in contrast to *static* approaches that consider a time series as a collection of N *variables*. In other words, dynamical models take into account and exploit information encoded in the *ordering* of the time samples composing the time series whereas static models do not.

After presenting in Chapter 3 a *temporal* analysis of the fluctuations of functional connectivity, we review in the present section different *dynamical* models and corresponding statistics of functional connectivity derived from fMRI time series.

4.3 Dynamical measures and models of FC

Following the classification of *static* measures presented in Chapter 2, we propose the classification illustrated in Figure 4.1 for the *dynamic* measures of FC.

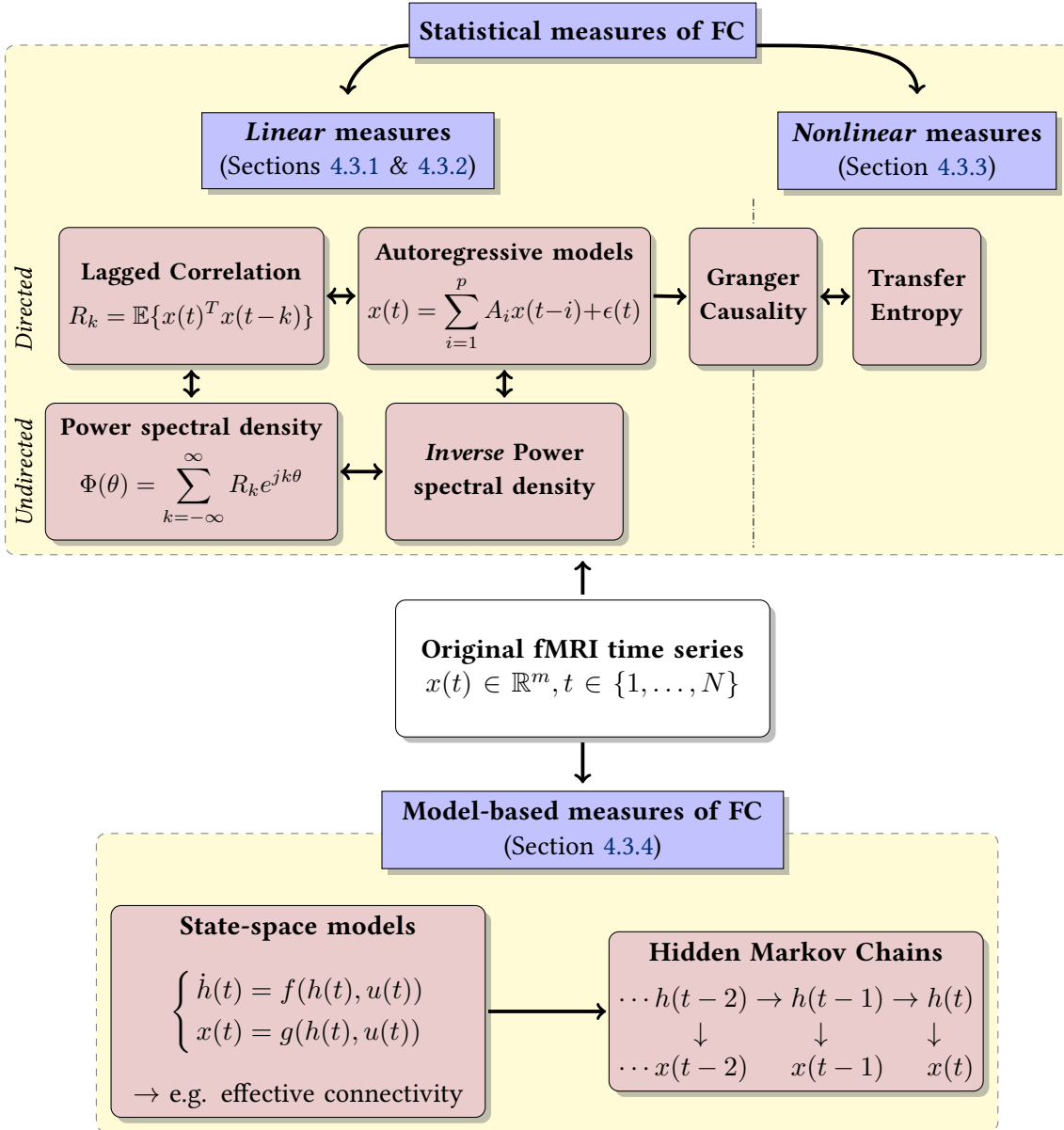


Figure 4.1 – Starting from the original (preprocessed) fMRI time series represented in the central white box, this schematic provides an overview of different popular *dynamic* measures of functional connectivity. Upper panel presents statistical measures directly derived from fMRI time series. Within this panel, classification is done based on (non)linearity (*left-right*) and (non)symmetry (*first/second* line) of the FC measures. In the lower panel we finally represent some measures of FC based on an explicit modelling of underlying neuronal activity.

We first present in the upper panel of Figure 4.1 the *statistical* measures that can be directly derived from the original time series for which the time indexing is now explicitly taken into account, as opposed to the static case (see white boxes in Figures 2.1 & 4.1). These measures are first classified based on the (non)linearity nature of the interactions they capture, as for static measures of FC presented in Chapter 2.

Then, the information encoded in the ordering of the time series leads to a second dichotomy between subclasses of statistical dynamical measures. Indeed the precedence information offers the possibility, for some dynamical frameworks, to identify *causality* relationships, or *directed* statistical links from one variable towards another variable. This type of approach results in *non-symmetric*, or *directed* measures of functional connectivity. Indeed, one can for example imagine that x_i is informative in order to predict “future” values of x_j whereas x_j does not provide any information about “future” values of x_i . Hence in the sequel we also distinguish between the different dynamical measures of FC based on this second criterion, which was not used in Chapter 2 since *static* measures of FC are inherently symmetric, or undirected. Undirected measures of FC are represented in the first line of the upper panel in Figure 4.1 and directed measures are represented in the second line of the same panel.

Finally, we also discuss a last class of measures of FC (lower panel in Figure 4.1) based on explicit modelling of the underlying neuronal activity that gives rise to the BOLD signal measured in fMRI time series.

4.3.1 Directed linear statistics and models

We first present *directed* linear models and corresponding statistics, leading to *non-symmetric* measures of functional connectivity.

Lagged correlation

One simple measure of connectivity exploiting temporal information of fMRI time series is the *lagged correlation sequence* denoted $\{R_k\}$. This sequence is defined from multivariate time series $x(t) \in \mathbb{R}^{N \times m}$ as:

$$R_k = \mathbb{E}[x^T(t+k)x(t)], k \in \mathbb{N}, \quad (4.1)$$

where N is the number of time samples and m is the number of variables of x . This sequence can be evaluated from the fMRI time series by the following approximation:

$$\tilde{R}_k = \frac{1}{N-k} \sum_{i=1}^{N-k} [x(i+k)^T x(i)]. \quad (4.2)$$

It should be noted that this formulation is the dynamical extension of the estimated correlation matrix defined in (2.1); in particular we have that $\tilde{\Sigma} = \tilde{R}_0$.

One of the advantages of considering lagged correlations is that they can capture connections between delayed fluctuations in the time series, which can typically be observed in the BOLD signal. Indeed, as already presented in Figure 1.2 and associated discussion, the underlying neuronal activity is indirectly encoded into the BOLD response via the *hemodynamic response function* (HRF) which has been shown to be potentially different in different cerebral regions. Hence, a simultaneous underlying neuronal activations sometimes lead to delayed BOLD responses, with shifts on the order of 1 to 3 seconds (Rajapakse et al., 1998). Hence, considering the fact that the sampling period in fMRI protocols is usually around 2 seconds, it seems relevant to consider at least the first lagged correlation matrix in order to capture these potential “delayed correlations”.

For these reasons, the connectivity measures encoded in the non-symmetric R_k , $k \geq 1$ can not lead to interpretations in terms of *causality* because a given precedence in the BOLD responses does not automatically translates into the same precedence, or causality of the underlying neuronal activations.

Autoregressive models

A closely related modelling approach is the autoregressive (AR) representation of the multivariate time series $x(t) \in \mathbb{R}^m$, $t \in \{1, \dots, N\}$. In this case, the impact every variable has on the next values of each other variable is explicitly modelled as follows:

$$x(t) = \sum_{i=1}^p A_i x(t-i) + \epsilon(t), \quad (4.3)$$

where p is the number of previous samples of x considered in the expression of $x(t)$ -the corresponding model is an AR(p) model-, A_i is a matrix encoding the weights of $x(t-i)$ in the expression of $x(t)$, and $\epsilon(t)$ is gaussian noise.

It should be highlighted that considering an AR(p) model of the time series is related to considering the first p correlation lags $\{\tilde{R}_k\}$, $k \in \{1, \dots, p\}$ through the Yule-Walker equations that are usually used in order to identify the parameters of the AR(p) model (Yule, 1927; Walker, 1931):

$$\begin{bmatrix} \tilde{R}_0 & \tilde{R}_1^* & \dots & \tilde{R}_p^* \\ \tilde{R}_1 & \tilde{R}_0 & & \vdots \\ \vdots & & \ddots & \tilde{R}_1^* \\ \tilde{R}_p & \dots & & \tilde{R}_0 \end{bmatrix} \begin{bmatrix} I \\ A_1 \\ \vdots \\ A_p \end{bmatrix} = \begin{bmatrix} \Sigma \\ 0 \\ \vdots \\ 0 \end{bmatrix}. \quad (4.4)$$

where Σ is the covariance of ϵ in (4.3).

Classically, it is the information encoded in A_i that is exploited in order to characterise dependencies between brain regions (Harrison et al., 2003). As for the lagged correlations, the connectivity measures encoded in the (non-symmetric) A_i matrices obviously capture both neuronal and hemodynamic factors leading to delicate interpretations in terms of functional connectivity (Rogers et al., 2010).

Extensions to this approach include prior deconvolution of the HRF from the observed time series in order to apply the AR identification process on time series expected to represent true underlying neuronal activity (David et al., 2008). However, this leads to complex inversion problems, hereby limiting the scalability of this approach to whole-brain level analyses.

Granger Causality

Granger causality (Granger, 1969) has been one of the most popular tools used to identify *causal* connectivity from fMRI time series and other neuroimaging modalities (Bressler and Seth, 2011). We place it in Figure 4.1 between the linear and nonlinear statistical measures of FC because it relies on the autoregressive formulation (4.3) of the fMRI time series, but the statistics that is deduced from the AR identification process is more related to information-theoretic measurements, as we now detail.

In the bivariate case (i.e. $m = 2$), the first order AR model writes:

$$\begin{cases} x_1(t) = a \cdot x_1(t-1) + b \cdot x_2(t-1) + w \\ x_2(t) = c \cdot x_1(t-1) + d \cdot x_2(t-1) + z, \end{cases} \quad (4.5)$$

where a, b, c , and d are the parameters of A_1 , and w and z are noise. Granger causality is then evaluated by first computing the univariate model for x_1 alone:

$$x_1(t) = a \cdot x_1(t-1) + u, \quad (4.6)$$

and then fitting the bivariate model:

$$x_1(t) = a \cdot x_1(t-1) + b \cdot x_2(t-1) + w. \quad (4.7)$$

Granger causality is eventually calculated from the variance of the residuals w and u as follows:

$$G(x_2 \rightarrow x_1) = \log \frac{\text{var}(u)}{\text{var}(w)}.$$

If $G(x_2 \rightarrow x_1) > 0$, the variance of u is greater than the variance of w which means that the fitting in the bivariate model of $x_1(t)$ in (4.7) is better than in the univariate model (4.6). In other words, x_2 encodes statistically significant values about future values of x_1 and we say that x_2 “Granger causes” x_1 .

In the present case of the BOLD signal measured in fMRI imaging, as already mentioned it might be the case that simultaneous neuronal activation lead to lagged changes in the BOLD signal in the corresponding regions due to different hemodynamic response functions (David et al., 2008). Hence once again the notion of “causality” does not apply in this case as the precedence of neuronal activations can not be assessed. As in the case of AR models, a proper deconvolution of the fMRI time series can be applied (e.g. Wen et al., 2013), with the same drawbacks as the one highlighted in the previous section.

In conclusion, the same limitations as for autoregressive models due to the non-symmetric nature of the connectivity measure provided by Granger causality apply here.

4.3.2 Undirected linear statistics and models

We have seen that primal dynamical statistics computed from the fMRI time series result in non-symmetric measures of functional connectivity. These measures are difficult to interpret because they capture both neuronal and hemodynamic factors, hence no causality can be interpreted from these measures. We now present two *symmetric*, or *undirected* measures of connectivity, as well as their links with the measures presented in the previous section.

Power spectral density

The Power Spectral Density (PSD) is defined as the Discrete Time Fourier Transform of the lagged correlation sequence $\{R_k\}$ defined in (4.1) (Stoica and Moses, 1997):

$$\Phi(e^{j\theta}) = \sum_{k=-\infty}^{\infty} R_k e^{jk\theta}, \quad (4.8)$$

which has a symmetric real part and an anti-symmetric imaginary part, and gathers all the information encoded in the lagged correlation sequence in a single mathematical object. By applying the inverse Fourier Transform, each covariance lag can also be recovered from the PSD, which illustrates that the two representations eventually gather the same information.

The PSD can be seen as the dynamical extension of the static correlation matrix defined in (2.1). Indeed, for each pair of variables x_i and x_j , $\Phi(e^{j\theta})_{i,j}$ encodes a measure of dependence between these two variables, as a function of $\theta \in [0, 2\pi]$. In other words, the PSD contains a correlation matrix for each $\theta \in [0, 2\pi]$, providing a measure of functional connectivity for each frequency. This frequency-banded correlation, which can be computed from the coherence or from the wavelet decomposition, is a popular measure of FC in EEG for which the distinction between connectivity in different frequency bands δ , α , β and γ is important (e.g. [D'avanzo et al., 2009](#)). It can also be applied to fMRI time series (e.g. [Sun et al., 2004](#); [Van De Ville et al., 2004](#)) but the evaluation of the connectivity patterns in different frequency bands does not appear to be as relevant as for EEG since there is no well known spectral localisation of information, as opposed to the case of EEG. Hence, capturing efficiently the (static and dynamic) connectivity information encoded in the PSD still represents a challenge in neuroimaging applications and is further discussed in Chapter 5.

Inverse power spectral density

The interpretation of the *inverse PSD*, compared to the PSD, is similar to the interpretation of the *precision matrix*, compared to the correlation matrix developed in section 2.2.2. Hence, the inverse PSD encodes *conditional* dependencies between the variables discounting shared input effects (see Figure 2.2), whereas the PSD encodes the classical linear dependencies between each pair of variables, and for each frequency. The following relation, extending the static result (2.16) also holds: two variables x_k and x_l are independent, conditionally on the other variables of x over $\{t \in \mathbb{Z}\}$, if and only if

$$(\Phi(e^{j\theta})^{-1})_{kl} = 0 \quad \forall \theta \in [0, 2\pi]. \quad (4.9)$$

The mathematical derivation is omitted here but can be found in [Brillinger \(2001\)](#). Let us finally note that the covariance selection problem presented in the static case can also

be extended to the dynamic case, with the same interpretation and the same possibilities of regularisation of the cost function as the ones described in section 2.2.2. This is the basis of the work presented in Chapters 6 and 7.

4.3.3 Nonlinear statistics

As in the static case, some dynamic measures of functional connectivity explore broader types of dependencies between the variables compared to linear dependencies captured by the measures described in the previous sections. One popular statistics belonging to this class is now presented, as well as its links with other static and dynamic measures.

Transfer Entropy

Transfer entropy (TE) is a nonlinear dynamical measure of functional connectivity, derived from information theoretic metrics and defined as follows ([Schreiber, 2000](#)):

$$T_{x_i \rightarrow x_j} = H(x_j(t)|x_i(t-1:t-p)) - H(x_j(t)|x_i(t-1:t-p), x_j(t-1:t-p)), \quad (4.10)$$

where $H(a|b)$ is the Shannon entropy of a *conditioned* on the knowledge of b , and p is the number of lags considered to compute transfer entropy. In words, $T_{x_i \rightarrow x_j}$ evaluates how knowing past values of x_i reduces uncertainty about future values of x_j , knowing its past values.

TE is an extension of the static mutual information (see section 2.3.1) to conditional probability distributions. Conditioning on these specific variables shown in (4.10) makes it a *directed* and *dynamical* metric. It has been widely used in several applications, including exploration of transfer of information between fMRI time series ([Lizier et al., 2011](#); [Vicente et al., 2011](#)). However, the limitations highlighted for directed measures in the above section still hold. Finally, it should be noted that as the definition of TE strongly echoes the one of Granger causality, it can actually be shown that for gaussian variables Granger causality is equal to TE ([Barnett, 2009](#)).

4.3.4 Model-based measures of FC

The measures of functional connectivity detailed in the previous sections are directly derived from the fMRI time series. As already mentioned, the BOLD signal measured in the fMRI time series only indirectly reflects neuronal activations. We now briefly describe two approaches explicitly modelling the underlying neuronal activations from the observed fMRI data in order to provide a better interpretation of the observed interactions among the fMRI time series.

State-space models

State-space models can be generically represented as follows:

$$\begin{cases} \dot{h}(t) = f(h(t), u(t)) \\ x(t) = g(h(t), u(t)) \end{cases} \quad (4.11)$$

In the case of fMRI data, the state variables most often refer to the underlying neuronal activity producing the changes in the BOLD signal encoded in the fMRI time series. The underlying neuronal activity is important because it encodes the “true” interactions between different cerebral regions. Connectivity measures capturing interactions at this level are called *effective* connectivity which refers to the influence one neuronal system exerts over another (Friston et al., 2003; Bhattacharya et al., 2006) which is assumed to make more neurological sense than *functional* connectivity. A representative example of this approach is the dynamical causal modelling (DCM) framework introduced in Friston et al. (2014). The corresponding generative model writes:

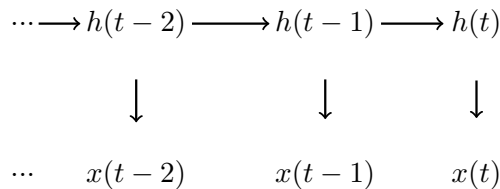
$$\dot{h}(t) = A h(t) + u(t)$$

where $h(t)$ encodes the hidden neuronal states driven by their interconnections to other regions through A which encodes *effective connectivity* measures, and by endogenous fluctuations $u(t)$. The parameters that have to be estimated here are the matrix A and the parameters used in the general formulation of $u(t)$, usually a power law. Then the link between state variables and the observed fluctuations x is described by the function g in (4.11) called the *hemodynamic response function* that also has to be parametrised (Stephan et al., 2007).

In order to identify the proper parameters of A , u and g , a Bayesian model comparison is performed, which leads to hard inversion problems. The resulting exponential complexity limits the size of the neuronal networks considered in these types of approaches to five or six nodes which can be insufficient. Another recurrent criticism against this framework is that since the parameter space is very large, there is no guarantee of finding a *true* set of parameters due to the high risk of overfitting (Lohmann et al., 2012). These limitations could be overcome by adding prior information about the hidden variables using other data sources such as EEG as for example presented by Lenz et al. (2011), but merging different neuroimaging modalities is still a challenge, and is a different -yet related- research topic than the one discussed in the present Chapter.

Hidden Markov Models

Hidden Markov chains or models (HMM) (Baum and Petri, 1966) are also bi-layer models for which the second layer are the observations x and the first layer are the hidden variables h causing the observations. HMM are classically represented as follows:



HMM can be seen as specific case of discrete state-space models including two specific properties:

1. First, the hidden variables in a HMM describe *discrete* states. In the case of fMRI time series, the hidden variables can usually take only two values, or two states corresponding to neuronal active and non-active states (e.g. Duan and Man, 2012). This approach is motivated by the binary-like behaviour of neurons observed at the microscopic level that are roughly either in bursting mode or at rest. At the macroscopic level we are considering in the case of fMRI data this assumption is perhaps over simplistic as the measures result from the interactions within populations of neurons which can be very different compared to single neurons behaviours (Moran et al., 2013).
2. Then, the hidden variables are assumed to satisfy the Markov property:

$$\mathbb{P}(h(t) = h_t | h(t-1) = h_{t-1}, \dots, h(0) = h_0) = \mathbb{P}(h(t) = h_t | h(t-1) = h_{t-1}) \quad (4.12)$$

where $h_i, i \in [0, \dots, t]$ are the discrete states mentioned in the first point.

In words, (4.12) implies that the state of the hidden variable h in time t is influenced only by the state of h in time $t - 1$. Another way of formulating this is that the previous lag is sufficient in order to capture the memory of the system explaining the current value of h .

It should finally be noted that the transition from the hidden states h to the observed variables x is also a challenge in this modelling approach. As discussed for state space models this transition has to be estimated through the hemodynamic response function which can not be considered to be the same in each region.

In conclusion, HMM do not seem to be geared towards exploring dynamical properties of fMRI time series. Indeed, they require strong modelling assumptions about the HRF, and considering a limited number of states of neuronal activity does not seem particularly relevant during resting state, even if it could be relevant in different experimental settings.

4.3.5 Dynamical component analysis ?

It should be noted that we did not include in the preceding classification component analysis techniques as potential tools to measure dynamical properties of FC, as opposed to the static case where we presented PCA and ICA. This is because, in our opinion, current dynamical approaches using component analysis techniques do not really capture inherent dynamical properties of FC.

For example, a first type of approach is to apply PCA or ICA to segmented versions of the original time courses ([Banko et al., 2011](#); [Leonardi et al., 2013](#)). As precised in section 4.2 this is more closely related to *temporal* models of functional connectivity.

Another approach, closer to *dynamical* modelling, is to apply component analysis techniques in the Fourier domain of the observed neuroimaging data ([Brookes et al., 2011](#); [Ramkumar et al., 2014](#)). This framework is interesting because it allows to build up a spatio-temporal view of functional connectivity, but it relies on a sequence of different steps (Fourrier transformation, bandpass filtering, etc., see e.g. Figure 2 in [Ramkumar et al. \(2014\)](#) for details) possibly limiting robustness and coherency of the whole analysis process.

In Chapters [6](#) & [7](#) we propose a component analysis technique based on a *dynamical* generative model, as opposed to classical ICA or PCA. As a consequence the dynamical aspect is a built-in feature of the proposed framework allowing a comprehensive and coherent dynamical analysis from and of the original fMRI time series.

4.4 Conclusion

The main dichotomies that we exploit in the classification proposed in this Chapter are the (non)linearity and the (non) directionality of the proposed measures of connectivity, as well as the use or not of hidden variables to model underlying neuronal activity. The properties of the different modelling approaches highlighted here motivate the work presented in the next Chapters.

First, it does not appear from the results reviewed here that considering more complex metrics of connectivity, able to capture linear and nonlinear dependencies between variables, lead to significantly better results compared to the equivalent linear metrics. On the contrary, their interpretation often seems to be delicate because the type of dependency highlighted by these models can take various forms.

Then, directionality of the connectivity measure and the associated notion of causality are actively debated when applied to fMRI time series. It appears from the most recent studies that causality can not be assessed because of different time delays in the BOLD signal appear in different brain regions after a neuronal activation. Hence, in order to avoid difficulties of interpretation, we prefer considering undirected measures of connectivity that are easier to compute and to interpret.

Finally, modelling the presence of hidden variables should be considered only if the cost of identifying plausible hidden variables does not lead to crippling computational complexity. In particular, if the hidden variables are assumed to capture underlying neuronal activity, and are linked to the observed variables via an unknown function to be determined using some identification process, this approach does not seem to us well suited in order to explore functional connectivity between multiple brain regions.

CHAPTER 5

Spatiotemporal connectivity

After exploring the temporal fluctuations of functional connectivity in Chapter 3, the motivation of the work presented in this Chapter is to extract simple markers of the spatial and dynamical properties of functional connectivity, based on the properties of existing markers presented in Chapters 2 and 4. The selected spatiotemporal markers are applied to fMRI data and compared to classic static connectivity measures. This work was selected in an original formulation for an oral presentation at the Second Whistler Scientific Workshop on Brain Function:

R. Liégeois, M. Ali Bahri, M. Zorzi, S. Laureys, and R. Sepulchre. *Dynamical properties of fMRI connectivity in neuronal networks mediating consciousness.* Second Whistler Scientific Workshop on Brain Function, Whistler, Canada, 2014.

5.1 Introduction

In Chapter 4 we describe different *dynamical* generative models for neuroimaging time series. It appears from the different properties of these models that the most straightforward extension of classical connectivity matrices in the context of dynamical models is the power spectral density (PSD). For each couple of variables, the PSD encodes a measure of (in)dependence between the corresponding variables, as a function of $\theta \in [0, 2\pi]$. In other words, PSD encodes one connectivity matrix for each value of $\theta \in [0, 2\pi]$. This considerably enlarges the amount of information to be analysed about connectivity properties and

rises the question of how to capture efficiently this information which is first addressed in the present Chapter.

Then, we also explore from an experimental point of view the difference between information contained in PSDs and *inverse* PSDs that encode *conditional* dependence relationships, based on markers similar to the ones defined for PSDs.

This chapter is organised as follows. We first define three markers of spatial and temporal connectivity based on first order approximations of the (inverse) PSD, collectively forming what we call *spatiotemporal connectivity (STC)*. We then illustrate the use of STC on two fMRI datasets. The first one consists of fMRI time series of healthy subjects undergoing four different states of consciousness. This set has already been studied using static connectivity measures in [Vanhaudenhuyse et al. \(2011\)](#), allowing us to highlight the differences between a static and a dynamic characterization of connectivity. The second one also consists of fMRI time series and was acquired on Alzheimer patients with different levels of anosognosia, the degree of self-awareness of the presence of the disease. In both cases we show that STC, computed either from the PSD or the inverse PSD, leads to a finer description of the level of functional connectivity, compared to the classical static markers.

5.2 Methods

The following reminders are common results that can be found in many reference books such as [Box and Jenkins \(1976\)](#) or [Stoica and Moses \(1997\)](#).

The Power Spectral Density (PSD), as already mentioned in Section 4.3.2 of the previous Chapter, is defined as the Discrete Time Fourier Transform of the sequence $\{R_k\}$:

$$\Phi(e^{j\theta}) = \sum_{k=-\infty}^{\infty} R_k e^{jk\theta}, \quad (5.1)$$

where $\{R_k\}$ is the lagged covariance sequence defined from multivariate time series $x(t) \in \mathbb{R}^m, t \in \{1, \dots, N\}$ as:

$$R_k = \mathbb{E}[x^T(t+k)x(t)], k \in \mathbb{N}. \quad (5.2)$$

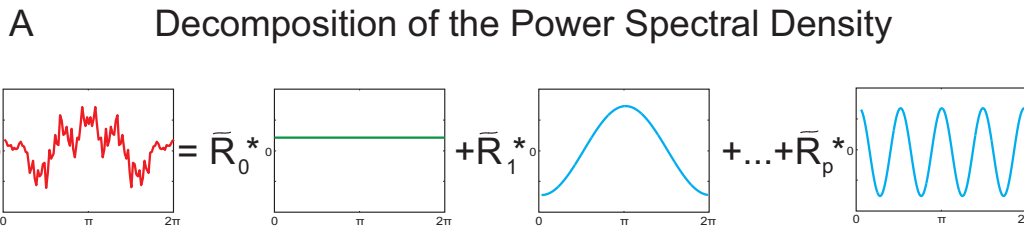
This sequence can be evaluated from the time series by the following approximation:

$$\tilde{R}_k = \frac{1}{N-k} \sum_{i=1}^{N-k} [x(i+k)^T x(i)]. \quad (5.3)$$

Hence, if one considers only the p first estimated lagged correlation matrices \tilde{R}_k , $|k| \leq p$, the PSD can be estimated by:

$$\Phi(e^{j\theta}) = \sum_{k=-p}^p \tilde{R}_k e^{jk\theta}. \quad (5.4)$$

This approximation of the power spectral density is illustrated in Figure 5.1 A in the univariate case:



B First order approximation in static and dynamic systems

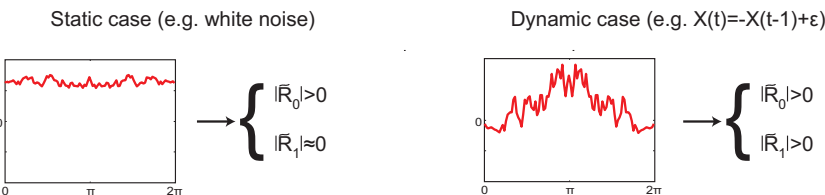


Figure 5.1 – (A) Standard decomposition of the PSD in the frequency domain. \tilde{R}_0 corresponds to the classic static contribution of the PSD whereas further estimated covariance lags $\tilde{R}_1, \dots, \tilde{R}_p$ correspond to the dynamical contribution to the PSD. (B) Using a first order approximation of the PSD, the dynamical properties of a univariate time course can be characterised using \tilde{R}_0 and \tilde{R}_1 .

Figure 5.1B then shows the estimation of a static and a dynamic system using the first two estimated lagged correlations. Static processes show a flat power spectral density corresponding to a large value of $|\tilde{R}_0|$ and small values of $|\tilde{R}_1|$ whereas for dynamical processes $|\tilde{R}_0|$ and $|\tilde{R}_1|$ are both a priori significantly greater than zero. This led us to use first order approximations of the PSD in order to capture dynamical properties of the original time series. Furthermore, instead of extracting information directly from PSDs

it seems more adequate to deduce it from its building blocks \tilde{R}_0 , assumed to capture the *static* contribution to the connectivity, and \tilde{R}_1 , assumed to capture its *dynamic* contribution.

Based on these considerations, we define for a specific network of size m *spatiotemporal connectivity* in the multivariate case (\tilde{R}_0 and \tilde{R}_1 are in this case matrices of size m) using three complementary measures of connectivity.

5.2.1 Spatiotemporal connectivity

Definition 5.2.1 Spatiotemporal connectivity (STC) is defined from the first two elements of a lagged correlation matrix sequence such as $\{\tilde{R}_k\}$ as the collection of the three following measures:

$$\left\{ \begin{array}{l} \sigma_s = \frac{1}{m^2 - m} \sum_{\substack{i,j=1,\dots,m \\ i \neq j}} |\tilde{R}_0|_{i,j}, \\ \sigma_d = \frac{1}{m^2 - m} \sum_{\substack{i,j=1,\dots,m \\ i \neq j}} |\tilde{R}_1 + \tilde{R}_{-1}|_{i,j}, \\ \delta = \frac{1}{m} \sum_{i=1,\dots,m} |\tilde{R}_1|_{i,i} = \frac{1}{m} \text{tr}(|\tilde{R}_1|), \end{array} \right. \quad (5.5)$$

where:

- σ_s is the average classical static correlation in the network formed by the m variables, hence encoding spatial dependencies between the variables,
- σ_d is the average dynamic correlation which measures how each region is dynamically connected to each other in the network formed by the m variables hereby encoding spatiotemporal connectivity information,
- δ is the average first order auto-correlation of the variables composing the network. High values of δ correspond to processes that are highly determined by their past time samples, or equivalently possessing an internal memory, whereas small values of δ essentially correspond to static processes such as noise. Hence, δ captures an average of what we call temporal connectivity of each variable belonging to the network. ◇

As highlighted in this definition, these markers provide spatial and temporal measures of connectivity, which is the reason why they collectively form what we call *spatiotemporal* connectivity, or STC. Figure 5.2 shows how STC can be represented:

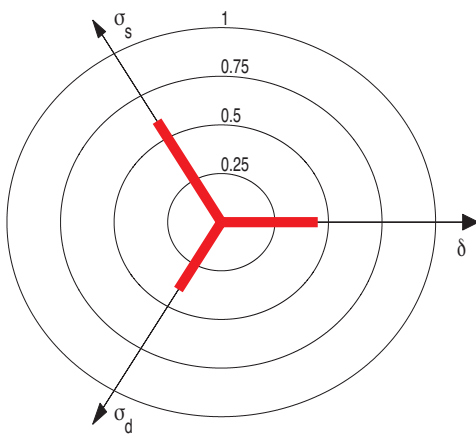


Figure 5.2 – Spatiotemporal Connectivity is characterised by three complementary measures of connectivity: static connectivity σ_s , dynamic connectivity σ_d and first order auto-correlation δ .

We also show in Figure 5.3 the values of the three markers of STC in four representative cases of a two-dimensional network.

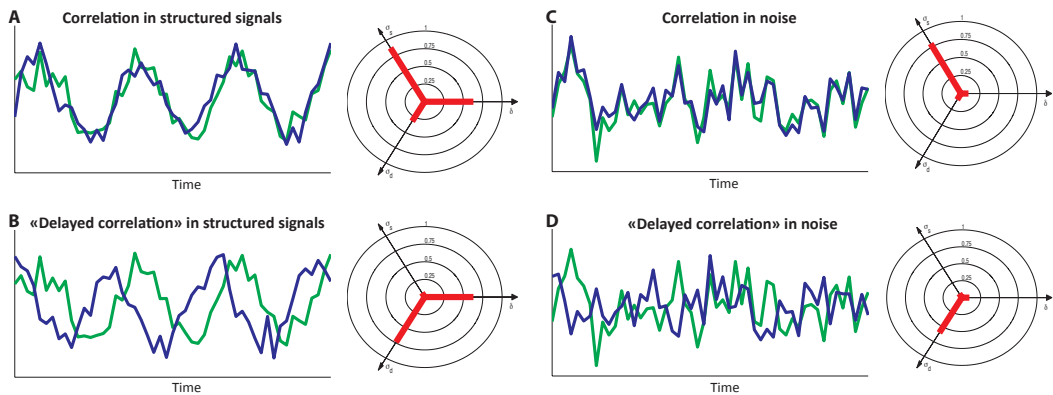


Figure 5.3 – Spatiotemporal Connectivity in four different cases.

Figure 5.3A presents the case of two highly temporally structured and correlated signals, as classically defined in static models (e.g. using Pearson's correlation). In this case σ_s and δ have high values and σ_d is low. Figure 5.3B also considers the case of two temporally structured signals (high δ) but in this case the two signals are unsynchronized leading to a low value of the static correlation σ_s . However, there is obviously a "connection" between the two signals and it appears that this connection is now captured by the dynamic correlation coefficient σ_d . The right part of Figure 5.3 represents the same cases but for temporally unstructured signals, leading to a low value of δ .

The cases represented in Figure 5.3B,D in which one signal is delayed with respect to the other are important because they can typically be encountered in fMRI time series. Indeed, the neuronal activity happening in a specific cerebral region is first filtered by the *hemodynamic response function* before giving rise to the BOLD signal captured by magnetic resonance imaging. In addition, it has been shown that the hemodynamic response function can be different in different cerebral regions (David et al., 2008). This leads to different filtering of the underlying neuronal activity, hence different delays for the corresponding BOLD fluctuations, as modelled in Figure 5.3B,D.

5.2.2 STC from the estimated inverse power spectral density

As already mentioned in this thesis the PSD encodes statistical dependencies between the variables whereas its inverse encodes *conditional* dependence between the variables, that is, their dependence conditioned on all the other variables. The interested reader can find the mathematical justification for this in Section 2.2.2 and in Brillinger (2001).

It appears that from an autoregressive representation of the initial fMRI time series:

$$B_0x(t) = - \sum_{k=1}^p B_k x(t-k) + \nu(t), \quad \nu(t) \sim \mathcal{N}(0, I), \quad (5.6)$$

it is possible to define a sequence $\{\tilde{Y}_k, |k| \leq p\}$ such that:

$$\tilde{Y}_k = \sum_{l=0}^{p-k} B_l^T B_{l+k} \text{ for } k = 0, \dots, p \text{ and } \tilde{Y}_{-k} = \tilde{Y}_k^T. \quad (5.7)$$

Then, the inverse PSD of the autoregressive process (5.6) is given by (Songsiri and Vandenberghe, 2010):

$$\Phi(e^{j\theta})^{-1} = \sum_{k=-p}^p \tilde{Y}_k e^{jk\theta}. \quad (5.8)$$

Based on this formulation of the estimated inverse PSD, we propose another measure of STC based on \tilde{Y}_0 and \tilde{Y}_1 following definition 5.2.1. In order to avoid confusion in the sequel, we denote STC_R (STC_Y) the measure of spatiotemporal connectivity computed from $\{\tilde{R}_k\}$ ($\{\tilde{Y}_k\}$), hence capturing connectivity properties encoded in the approximated (inverse) PSD.

5.3 Materials

The STC framework was applied to two fMRI datasets.

5.3.1 Propofol-induced loss of consciousness dataset

Data was collected from 19 healthy volunteers (age range 22.4 ± 3.4 years, 15 women, all right-handed). Volunteers gave their written informed consent to participate in the study, which was approved by the Ethics Committee of the Faculty of Medicine of the University of Liège.

The subjects underwent four different states of consciousness: wakefulness (W), mild sedation (MS), deep sedation or unconsciousness (U) and subsequent recovery of consciousness (R). The same preprocessing as in ([Boveroux et al., 2010](#)) was performed including 0.007-0.1Hz bandpass filtering and global signal regression.

Representative seeds of four resting state networks were then selected and the average signal in a 6-mm spherical ROI was computed. Three seeds were selected in the default mode network, two seeds in the executive control network, one in the visual network and one in the auditory network. The MNI (Montreal Neurologic Institute) coordinates are given in Table 5.1.

Brain Area	MNI Coordinates		
	x	y	z
DMN			
Seed	6	-42	32
Precuneus	12	-61	25
Sup. Frontal Sulcus	21	35	46
EXN			
Right dorsolateral prefrontal cortex	44	36	20
Left dorsolateral prefrontal cortex	-44	36	20
Aud			
Left Heschl's gyrus	-40	-22	8
Right Heschl's gyrus	40	-26	14
Vis			
Visual Cortex	-4	-84	8
Medial Frontal Cortex	0	58	-14

Table 5.1 – MNI coordinates of the seven ROIs selected in four resting state networks.

5.3.2 Alzheimer patients with different levels of anosognosia dataset

Participants Thirty-one patients (21 women) with probable Alzheimer's disease (AD) (McKhann et al., 2011) and 19 healthy older adults (14 women) took part in the experiment. Patients were selected in the memory clinic, University Hospital of Liège, Belgium. Probable AD diagnosis was based on interviews with the patient and a relative, neuropsychological assessment, a clinical exam and neuroimaging. The University Hospital ethics committee approved the study and written informed consent was obtained from all participants.

Memory Awareness Rating Scales – MARS AD patients and healthy controls answered the MARS–Memory Functioning Scale (Clare et al., 2002), which is composed of sentences describing real-life situations where memory abilities are required. Patient's answers were then compared to answers to the same questions provided by relatives and an awareness score of the patient was finally calculated by evaluating the discrepancy between patient's and relative's answers (Clare et al., 2010). Based on these results, AD patients were classified into two groups: the anosognosic AD patients (AD-A), and the conscious AD patients (AD-C).

Neuroimaging data acquisition A high-resolution T1-weighted anatomical image was acquired on a 3T head-only scanner (Magnetom Allegra, Siemens Medical Solutions, Erlangen, Germany) operated with the standard transmit-receive quadrature head coil. Multislice T2*-weighted functional images were acquired with a gradient-echo EPI sequence using axial slice orientation and covering the whole brain (TR 2130 ms, 250 volumes). The initial three volumes were discarded to avoid T1 saturation effects.

fMRI preprocessing The fMRI data were preprocessed using Statistical Parametric Toolbox (SPM8: Wellcome Department of Imaging Neuroscience, <http://www.fil.ion.ucl.ac.uk/spm>) implemented under MATLAB 7.12. The typical preprocessing steps of functional connectivity analysis including slice timing and motion corrections, spatial smoothing (FWHM = 8 mm), temporal filtering with a bandpass filter (0.005 to 0.1 Hz), and the removal of linear and quadratic temporal trends, were applied. In addition, the brain-averaged signal, the time series of regions of interest in the white matter and cerebrospinal fluid, and six affine motion parameters were regressed out from the dataset. The fMRI data of each subject was first spatially coregistered to high-resolution anatomical images and then to the 152-brain Montreal Neurological Institute (MNI) space.

Selecting regions of interest (ROIs) We selected the ROIs belonging to the default mode network (DMN) and listed in Table 5.2. This choice is motivated by the fact that we have prior information about the role that should be played by this network.

Brain Area DMN	MNI Coordinates		
	x	y	z
Orbito-frontal	-2	44	-18
Antero-medio-frontal	-3	55	9
Precuneus	1	-54	30
Right angular	52	-57	33
Left angular	-45	-51	38
Right temporal inf	58	-16	-26
Left temporal inf	48	7	-31
Left antero MTL	-59	-20	-12

Table 5.2 – MNI coordinates of the ROIs selected in the DMN.

Spatiotemporal connectivity We finally computed spatiotemporal connectivity in the DMN for the three groups of subjects: controls (CTRL), conscious AD patients (AD-C) and anosognosic AD patients (AD-A). The most significant results were obtained using δ and hence we report only results related to this marker of spatiotemporal connectivity.

5.4 Results

The results of the analyses of the two datasets are now detailed. We also include in this Chapter a brief discussion specific to each dataset, in order to focus on global considerations about the tool introduced here in the next section.

5.4.1 Propofol-induced loss of consciousness dataset

STC_R and STC_Y were computed from the time series recorded in the regions defined in Table 5.1. The three markers of STC_R are represented in Figure 5.4.

In order to evaluate the sensitivity of the different markers to the state of consciousness, assumed to be best captured in the DMN, we performed a paired t-test assessing the difference between the values of the different markers in the DMN during states W and U. The corresponding p-values are also indicated in Figure 5.4.

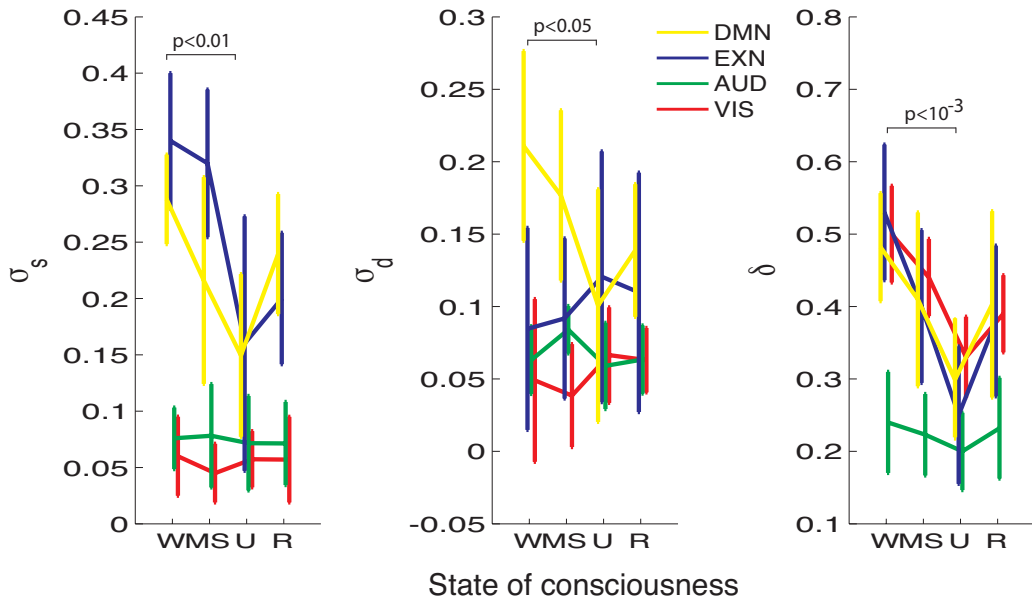


Figure 5.4 – Average and standard deviation of σ_s , σ_d and δ of STC_R in four different states of consciousness and in four networks: the default mode (DMN), the external control (EXN), the visual (VIS) and the auditory (AUD) networks. The results of a paired t-test assessing the significance of the difference between values of the markers in the DMN in states W and U is also showed.

In the DMN we observe a concomitant decrease in the three markers during the unconscious state (U), coherently with what is observed in [Vanhaudenhuyse et al. \(2011\)](#). In the EXN, we observe during the phase of unconsciousness a decrease in the static connectivity σ_s and in δ but an increase in the dynamic connectivity σ_d . This complements the findings of [Vanhaudenhuyse et al. \(2011\)](#) in which a significant decrease of (static) connectivity was found during the phase of unconsciousness. Indeed, our results suggest that the overall connectivity in the EXN does not disappear during this phase but is *delayed*.

Then, the marker of internal memory of the network, δ , seems to be a relevant marker of the state of consciousness. Indeed the decrease is much more pronounced for this marker during unconsciousness than for the other ones (lower p-value), in three networks (DMN, EXN, VIS) among the four considered here.

Finally, it should be noted that σ_s and σ_d provide no significant distinction between W and U states in the Visual network, whereas δ revealed significant differences. This is important because it shows that δ is not only a redundant measure of the first markers, but can be considered as an independent measure of connectivity, capturing its dynamical properties, hereby complementing the information captured by the first two markers.

Based on the approximated *inverse PSD* of the same dataset, we now represent the markers of STC , denoted STC_Y , in Figure 5.5:

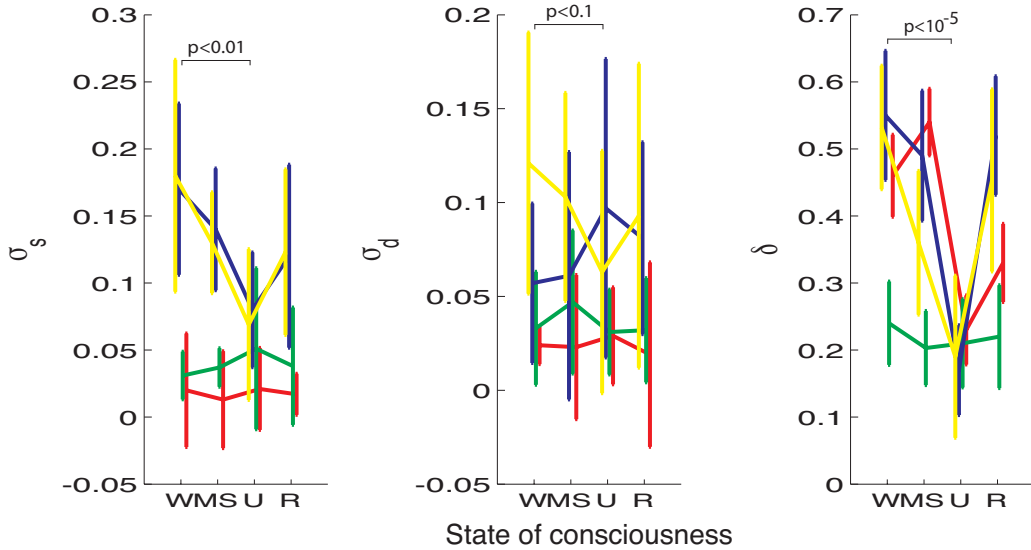


Figure 5.5 – Average and standard deviation of σ_s , σ_d and δ of STC_Y in four different states of consciousness and in four networks: the default mode (DMN), the external control (EXN), the visual (VIS) and the auditory (AUD) networks. The results of a paired t-test assessing the significance of the difference between values of the markers in the DMN in states W and U is also showed.

Even if the magnitude obtained for the markers of STC_Y is not exactly the same as the one of the markers obtained from STC_R , the general tendency for all the markers is highly similar between STC_R markers and STC_Y markers. Hence conditioning dependencies on other variables does not seem to affect qualitatively connectivity information contained in dependencies as encoded in PSDs. This similarity might be caused by the fact that the networks we considered are highly connected, and hence no intermediated connections can be significantly highlighted in the PSD, compared to their inverses, as illustrated in Figure 2.2.

We also computed STC_R and STC_Y from the next dataset and observed the same qualitative similarities between the corresponding markers. Hence we present in the sequel only the results obtained from STC_R .

5.4.2 Alzheimer patients with different levels of anosognosia dataset

We computed STC_R for this dataset and found significant differences between the three groups of subjects only based on the values of δ , represented in Figure 5.6. Hence the other markers of STC_R are not reported here.

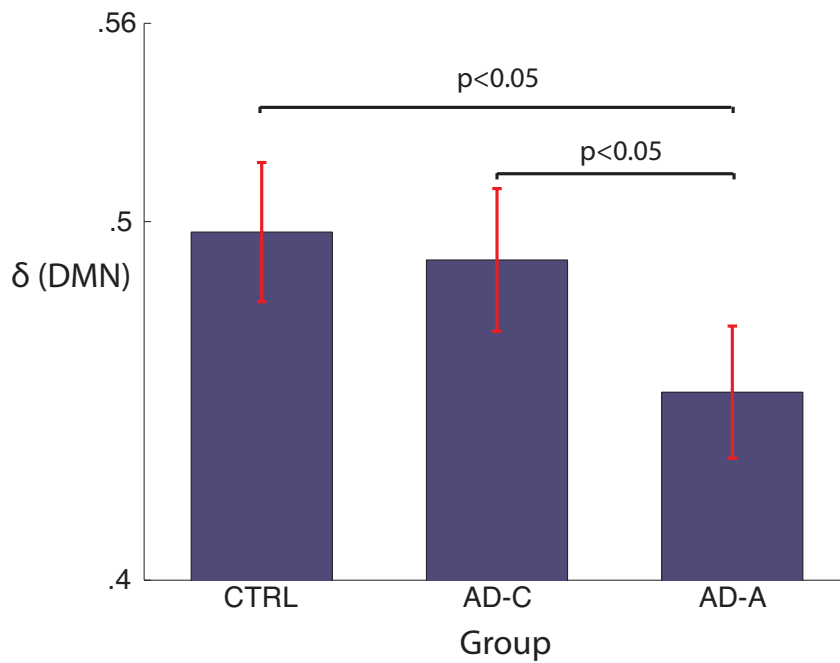


Figure 5.6 – Average and standard deviation value of δ in the three groups of subjects: controls (CTRL), conscious (AD-C) and anosognosic (AD-A) AD patients.

We observe a significant decrease of δ in the anosognosic patients compared to controls or conscious AD patients. However, this marker does not distinguish controls from conscious AD patients. One possible interpretation for this surprising observation is that δ is more sensitive to instantaneous self-awareness phenomena implied in anosognosia, than to losses of memory characterising AD patients. To our knowledge, this is the first time that conscious and anosognosic AD patients could be distinguished, based on fMRI time series.

In order to further characterize anosognosia in AD patients, we now show in Figure 5.7 the value of δ as a function of the MARS score used to evaluate the degree of anosognosia of AD patients (Clare et al., 2010).

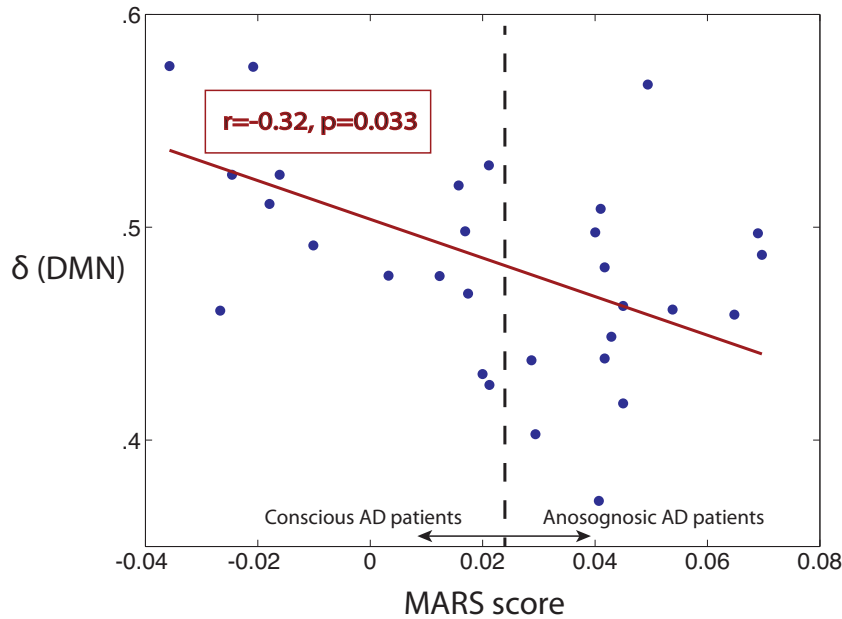


Figure 5.7 – δ as a function of the MARS score.

We observe a significant negative correlation between these values: higher values of δ correspond to patients with a higher degree of awareness of their disease. In other words, patients with a highly temporally structured signal in the default mode network are more aware of their disease.

5.5 Discussion

In this Chapter we illustrate the potential benefits of extending the notion of connectivity to dynamical models. The corresponding markers of connectivity proposed in this Chapter recover spatial and temporal connectivity information and from our results it appears that the latter is sensitive to the degree of consciousness, or awareness.

5.5.1 Extending the notion of connectivity

As spatial static functional connectivity, classically measured by correlation, is averaged over the whole time series, the primal motivation of this approach was to explore whether a similar measure could be extracted from the temporal information encoded in the fMRI time series. However, we here didn't want to track the *temporal* fluctuations of FC, or "non-stationarities" (Zalesky and Breakspear, 2015), which is the primal aim of using sliding windows, because of the limitations highlighted in Section 4.2. Rather, we wanted to characterise the *dynamical* properties of FC, and more particularly the extent to which

a network is influenced by its past. This notion is closely related to notions of auto-correlation, and it appears that δ , as computed from STC_R , precisely captures this aspect, as illustrated in Figure 5.3. σ_d , on the other hand, is closer to the classic static correlation except that correlation is detected for unsynchronised signals or delayed signals. Hence this marker appears to be a relevant complementary measure to static correlation as it has been demonstrated that fMRI signals can show unsynchronised activations due to different hemodynamic response functions (David et al., 2008). For these reasons, we claim that the three markers presented in definition 5.2.1 provide a spatiotemporal measure of functional connectivity and our results suggest that they provide a more comprehensive characterisation of connectivity compared to static connectivity, useful and relevant for applications to fMRI time series.

The proposed STC markers should also be compared to related work identifying AR models from the fMRI time series (e.g. Harrison et al., 2003; Maxim et al., 2005). In these approaches, it is the information encoded in the AR parameters, A_i as defined in (4.3), that is exploited in order to characterise dependencies between brain regions. The advantage of the STC markers lies in the decomposition of FC into static and dynamic contributions, whereas the link between A_i and FC is more ambiguous, in particular because these matrices are non symmetric.

5.5.2 Importance of internal memory

As we just discussed, δ provides a measure of the average internal memory within a network. From the results presented in Figures 5.4-5.7 it appears that this marker is highly sensitive to changes in the level of consciousness or awareness. These are preliminary results but we might expect that a careful examination of this marker in similar studies could help to reveal finer features of the fMRI connectivity properties.

5.5.3 PSD or inverse PSD ?

Figures 5.4 and 5.5, (as well as equivalent comparisons performed on the second dataset, not shown here) suggest that from a practical and qualitative point of view, the connectivity information as computed with STC markers, is highly similar when estimated from PSDs or inverse PSDs. We do not have a simple and unique explanation for this observation and the causes could be multiple. For example, it might be due to the fact that the variables considered in this case are effectively highly directly connected. In that case the level of correlation as measured in PSDs would be actually due to these direct interconnections, and not to indirect connections through a third intermediate variable, that are captured in PSDs, but not in their inverses, as illustrated in Figure 2.2. This hypothesis is plausible in this context as we always considered the computations of STC within networks that are known to be highly interconnected such as the default mode network (DMN). Comparing PSDs and their inverses in random networks could be a way to test this hypothesis.

5.5.4 Limitations and perspectives

This work is a first attempt to extend the notion of connectivity to dynamical models and several refinements might be considered. First, one may ask whether considering *first* order approximations is sufficient. Indeed, we could suspect that longer delays between the different time series might not be captured by considering only these approximations. This question highly depends on the spectral content and on the sampling rate of the time series. Indeed, considering only the previous sample in a dataset with high sampling rate and low frequency content might not be as informative as in the case of a low sampling rate and a distributed power spectrum which is closer to the case of fMRI time series. In addition, the potential delays due to different hemodynamic response functions are on the order of 1-2 seconds, which corresponds to the usual sampling rate in fMRI time series. For these reasons we believe considering first order models already significantly captures dynamical properties as well as potential “delayed correlations” of the considered network.

A clearer limitation of the approach in the present Chapter is that we compute STC within predefined networks, hence we need prior information about these networks and we cannot measure inter-network connectivity. In the static case, an alternative to analysing the values of the correlation matrix within (or between) different networks is to use components analysis techniques. These techniques provide a decomposition of the correlation matrix in a sum of different components that has been shown to be particularly relevant in the case of neuroimaging time series since these components can be interpreted as distinct neuronal networks. Hence, in Chapters 6 and 7 we explore the extent to which this decomposition could be transposed to the dynamical case presented here, leading to a framework needing no prior information about the brain connectivity properties or clusters.

It should finally be noted that the proposed markers of STC capture neuronal *and* non-neuronal related correlations (e.g. [Woolrich et al., 2001](#)). As a consequence these markers should be applied as a discriminating tool between different groups of subjects but its interpretation in terms of neuronal underlying processes remains delicate.

5.6 Conclusion

Spatiotemporal connectivity is a new tool to evaluate connectivity within networks. Since it is based on a *dynamic* generative model, it provides insight about the *spatio-temporal* connectivity properties of a network. From a spatial point of view, the first two markers of STC, σ_s and σ_d , can be seen as an extension of classical connectivity as they can capture connectivity between unsynchronised signals. From a temporal point of view, the last marker of STC, δ , encodes information about internal memory of the network that is totally neglected in classical static connectivity measures. From the analyses of two fMRI datasets, δ appears to be at least as informative and sensitive as classical connectivity measures

about the degree of consciousness of the subjects. Hence we believe this marker should be considered systematically in fMRI based studies as our results suggest it provides a complementary measure to static connectivity.

CHAPTER 6

Identifying low-rank plus sparse graphical models from large-scale data

The work presented in this Chapter is the main methodological contribution of the present manuscript. Following the motivation of component analysis in the static case, we propose an algorithm able to identify a sparse plus low-rank ($S+L$) decomposition of the inverse power spectral density. An efficient formulation is obtained by exploiting separability of the sparse and low-rank constraints, hereby scaling the algorithm to dimensions typically encountered in neuroimaging data. This Chapter corresponds to the technical contribution of the following paper. A detailed interpretation of the low-rank contribution as an extension of component analysis techniques to dynamical models is provided in the next Chapter.

R. Liégeois, B. Mishra, M. Zorzi, and R. Sepulchre. *Sparse plus low-rank autoregressive identification in neuroimaging time series*. Accepted at the 54th IEEE Conference on Decision and Control, Osaka, December 2015.

6.1 Introduction

We have seen in the previous Chapters that exploiting information contained in connectivity matrices (*static* models) or power spectral densities (*dynamical* models) has raised a lot of attention recently. In Chapter 5 we use the primary information encoded for each couple of variables in the correlation coefficients of these matrices or spectral densities, without

exploring the global structure of the macro-scale level connectivity patterns. A popular way to exploit this information, especially in neuroimaging applications, are *graphs* because they allow to study and represent the interactions between (groups of) variables in a concise manner ([Bullmore and Sporns, 2009b](#)).

Graphical models, a particular class of graphs already introduced in Section 2.2.2, encode information about dependence between the variables conditioned on all the other variables, or *conditional dependence* ([Koller and Friedman, 2009](#)). As detailed in Section 2.2.2, for *static* models this information is contained in the inverse of the covariance matrix, or *precision* matrix. The identification of the model is then a covariance selection problem¹ ([Dempster, 1972](#)). Additionally, as shown in Section 2.2.2, sparsity and/or low-rank structural constraints can be imposed to the precision matrix estimation. The sparsity constraint results from the parsimony principle in model fitting, i.e., one assumes few direct interactions between the variables, and is enforced through l_1 -norm regularizers ([Banerjee et al., 2008](#)). The low-rank structure, enforced through nuclear-norm regularizers, models the presence of *latent variables* that are not observed but generate a common behavior in all the observed variables ([Chandrasekaran et al., 2010](#)). The low-rank modeling is inspired from what is done in classical component analysis techniques, and leads to models that are simpler and more interpretable ([Jolliffe, 2002](#); [Hyvärinen et al., 2001](#)). An example of graphical model that is both sparse and low-rank is given in Figure 1.

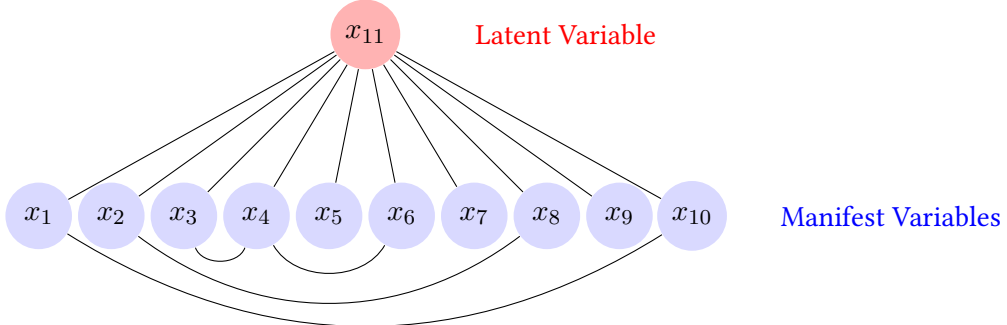


Figure 6.1 – Ten observed variables $x_i, i \in [1 \dots 10]$ with few interactions among them (sparse structure) and one latent variable x_{11} (low-rank structure).

In *dynamical* models, the additional information of the ordering of the data is taken into account and datasets are seen as time series. As reminded in Figure 4.1, a widely used class of models encoding this information are autoregressive (AR) models which are

¹ The interested reader will find the mathematical groundings of the interpretation of the precision matrix, as well as the derivation of the covariance selection problem in Section 2.2.2

characterized by their power spectral density, the dynamic equivalent of the covariance matrix ([Stoica and Moses, 1997](#)). As in the static case, it has been shown that a zero in the inverse power spectral density corresponds to conditional independence between two variables ([Brillinger, 2001](#)). In the dynamic case the (inverse) power spectral density is encoded in a block Toeplitz matrix. Because of this particular structure the classical l_1 -norm can not be used to induce sparsity in the inverse power spectral density. This problem is solved by introducing an alternate regularization proposed in ([Songsiri and Vandenberghe, 2010](#)). Finally, ([Zorzi and Sepulchre, 2015](#)) presents a unifying framework allowing sparse plus low-rank identification of inverse power spectral densities in multivariate time series.

In this Chapter we adapt the problem formulated in ([Zorzi and Sepulchre, 2015](#)) to the alternating direction method of multipliers (ADMM) framework of ([Boyd et al., 2011](#)) in order to scale it with larger datasets for which the CVX Matlab toolbox of ([Grant et al., 2005](#)) is computationally expensive. In particular, we exploit separability of constraints of the ADMM framework to decouple the sparsity and the low-rank constraints. The first update is a projective gradient update similar to the one proposed in ([Songsiri and Vandenberghe, 2010](#)) and the second update is a well known projection onto the cone of positive semidefinite matrices. In the numerical examples we show the performance of the proposed algorithm on a real neuroimaging dataset.

We present in the following Section the optimization problem leading to this sparse plus low-rank decomposition and we explain how we use ADMM to efficiently solve it in Section 6.3. We then show the results of our approach on synthetic and real data in Section 6.4 and conclude.

6.2 Problem formulation

We first introduce some basic notions, explain the motivation of the sparse plus low-rank (S+L) graphical models and then formally deduce the corresponding optimization problem.

Consider a q -dimensional autoregressive (AR) gaussian process $x = [x_1(t) \dots x_q(t)]^T$ of order p

$$x(t) = \sum_{i=1}^p A_i x(t-i) + \epsilon(t),$$

where $x(t) \in \mathbb{R}^q$, $A_i \in \mathbb{R}^{q \times q}$, $i = \{1, \dots, p\}$ and $\epsilon(t)$ is white gaussian noise with covariance matrix Σ . x is completely characterized by its spectral density $\Phi(e^{j\theta})$ which encodes information about dependence relations between the q variables ([Stoica and Moses, 1997](#)). On the contrary, as shown in the static case in Section 2.2.2, the *inverse* power spectral density $\Phi(e^{j\theta})^{-1}$ encodes *conditional* dependence relations between variables ([Brillinger,](#)

(2001; Dahlhaus, 2000). That is, two variables x_k and x_l are independent, conditionally on the other $q - 2$ variables of x over $\{t \in \mathbb{Z}\}$, if and only if

$$(\Phi(e^{j\theta})^{-1})_{kl} = 0 \quad \forall \theta \in [0, 2\pi]. \quad (6.1)$$

The nodes of the corresponding graphical model are the q variables of x and there is no edge between the two nodes x_k and x_l if and only if (6.1) is satisfied (Brillinger, 2001).

6.2.1 S+L graphical models

Assume that $x(t) = [(x^m(t))^T \ (x^l(t))^T]^T$ where $x^m(t) = [x_1(t) \dots x_m(t)]^T \in \mathbb{R}^m$ contains *manifest* variables, that is variables accessible to observations such as the brain regions in which the BOLD signal is measured in the case of fMRI data. On the contrary, the vector $x^l(t) = [x_{m+1}(t) \dots x_{m+l}(t)]^T \in \mathbb{R}^l$ contains *latent* variables, not accessible to observations. The power spectrum of x can be expressed using the following block decomposition

$$\Phi_x = \begin{bmatrix} \Phi_m & \Phi_{ml}^* \\ \Phi_{ml} & \Phi_l \end{bmatrix}, \quad \Phi_x^{-1} = \begin{bmatrix} \Upsilon_m & \Upsilon_{ml}^* \\ \Upsilon_{ml} & \Upsilon_l \end{bmatrix}, \quad (6.2)$$

where the $*$ denotes the conjugate transpose operation.

In order to better characterize the conditional dependence relations between the manifest variables, from (6.2) we obtain the following decomposition of Φ_m^{-1} using the Schur complement (Horn and Johnson, 1990)

$$\Phi_m^{-1} = \Upsilon_m - \Upsilon_{ml}^* \Upsilon_l \Upsilon_{ml}. \quad (6.3)$$

The main modeling assumption here is that $l \ll m$ and that the conditional dependencies relations among the m manifest variables encoded in Φ_m^{-1} can be largely explained through few latent variables. The corresponding graphical model has few edges between the manifest variables and few latent nodes, as in Figure 1. This leads to a S+L structure for Φ_m^{-1} following (6.3): $\Phi_m^{-1} = \Sigma - \Lambda$, where $\Sigma = \Upsilon_m$ is sparse because it encodes conditional dependence relations between the manifest variables and $\Lambda = \Upsilon_{ml}^* \Upsilon_l \Upsilon_{ml}$ is low-rank. Since x is an AR process of order p , we can assume that Σ and Λ belong to the

family of matrix pseudo-polynomials

$$\mathcal{Q}_{m,p} = \left\{ \sum_{j=-p}^p e^{-ij\theta} R_j : R_j = R_{-j}^T \in \mathbb{R}^{m \times m} \right\}.$$

Following [Zorzi and Sepulchre \(2015\)](#) we further rewrite Σ and Λ as

$$\begin{aligned} \Sigma - \Lambda &= \Delta X \Delta^*, \\ \Lambda &= \Delta L \Delta^*, \end{aligned} \tag{6.4}$$

where Δ is a shift operator $\Delta(e^{i\theta}) := [I \ e^{i\theta} I \ \dots \ e^{ip\theta} I]$ and X and L are now matrices belonging to $Q_{m(p+1)}$ which is the set of symmetric matrices of size $m(p+1) \times m(p+1)$.

Finally, $M_{m,p}$ is the vector space of matrices $W := [W_0 \ W_1 \ \dots \ W_p]$ with $W_0 \in Q_m$ and $W_1 \dots W_p \in \mathbb{R}^{m \times m}$. The linear mapping $\mathcal{T} : M_{m,p} \rightarrow Q_{m(p+1)}$ outputs a symmetric block Toeplitz matrix from the blocks of W as

$$\mathcal{T}(W) = \begin{pmatrix} W_0 & W_1 & \cdots & W_p \\ W_1^T & W_0 & \ddots & \vdots \\ \vdots & \ddots & \ddots & W_1 \\ W_n^T & \cdots & W_1^T & W_0 \end{pmatrix}.$$

The adjoint operator of \mathcal{T} is the linear mapping $\mathcal{D} : Q_{m(p+1)} \rightarrow M_{m,p}$ defined for a matrix $X \in Q_{m(p+1)}$ partitioned in square blocks of size $m \times m$ as

$$X = \begin{pmatrix} X_{00} & X_{01} & \cdots & X_{0p} \\ X_{00}^T & X_{11} & \cdots & X_{1p} \\ \vdots & \vdots & \ddots & \vdots \\ X_{0p}^T & X_{1p}^T & \cdots & X_{pp} \end{pmatrix}. \tag{6.5}$$

Following this partition, $W = \mathcal{D}(X) \in M_{m,p}$ is given by

$$\begin{cases} W_0(X) &= \sum_{h=0}^p X_{hh}, \\ W_j(X) &= 2 \sum_{h=0}^{p-j} X_{h,h+j} \quad \forall j = 1 \dots p. \end{cases} \tag{6.6}$$

6.2.2 S+L identification problem formulation

Assume that we have a finite length realization $x^m(1) \dots x^m(N)$ of the manifest process x^m . It should be emphasized that no data is available regarding the latent process x^l , and its dimension is not even known. Our goal is to recover the S+L model defined in the previous Section which best explains the collected data. Therefore, one estimate of X and L (hence of Σ and Λ) is given by solving the regularized maximum entropy problem (Byrnes et al., 1998; Cover and Thomas, 1991) for which the primal is

$$\begin{aligned} \min_{X, L \in Q_{m(p+1)}} \quad & -\log \det X_{00} + \langle C, X \rangle \\ & + \lambda \gamma h(\mathcal{D}(X + L)) + \lambda \operatorname{trace}(L) \end{aligned} \quad (6.7)$$

subject to $X \succeq 0, X_{00} \succ 0, L \succeq 0,$

where

- $\gamma > 0$ and $\lambda > 0$ are weighting parameters leading to a sparse Σ and a low-rank Λ ,
- $C = \mathcal{T}(\hat{R})$ where $\hat{R} \in M_{m,p}$ are the $p+1$ first sample covariance lags \hat{R}_k (Stoica and Moses, 1997),
- $\langle \cdot, \cdot \rangle$ is the inner product associated with $\mathbb{R}^{m \times m}$,
- h is the following function chosen to favor a structured sparse solution $\mathcal{D}(X + L)$

$$h(Y) = \sum_{j>i} \max\{|(Y_0)_{ij}|, \max_{k=1,\dots,p} |(Y_k)_{ij}|, \max_{k=1,\dots,p} |(Y_k)_{ji}|\}, \quad (6.8)$$

which is convex but non smooth. This limitation was overcome in similar works (Songsiri and Vandenberghe, 2010) by solving the corresponding dual problem. In the present case, it can be shown based on Songsiri and Vandenberghe (2010) and Zorzi and Sepulchre (2015) that the dual of (6.7) is

$$\begin{aligned} \max_{Z \in M_{m,p}} \quad & \Psi(C + \mathcal{T}(Z)) \\ \text{subject to} \quad & \sum_{k=0}^p (|(Z_k)_{ij}| + |(Z_k)_{ji}|) \leq \gamma \lambda, \quad i \neq j \\ & \mathbf{diag}(Z_k) = 0, \quad k = 0, \dots, p \\ & \lambda I + \mathcal{T}(Z) \succeq 0, \end{aligned} \quad (6.9)$$

where $\Psi : Q_{m(p+1)} \rightarrow \mathbb{R}$ is defined as

$$\Psi(V) = -\log \det(V_{00} - V_{1:p,0}^T V_{1:p,1:p}^{-1} V_{1:p,0}) - m,$$

and $V \in Q_{m(p+1)}$ is partitioned as in (6.5).

6.3 Alternating direction method of multipliers

We use the alternating direction method of multipliers (ADMM) as defined by [Boyd et al. \(2011\)](#) to solve (6.9). This choice is motivated by the fact that this algorithm both inherits the strong convergence properties of the method of multipliers and exploits decomposability of the dual problem formulation leading to efficient partial updates of the variables. We show how we rewrite (6.9) in the ADMM format by separating the sparse and low-rank constraints, then explain how we choose an adequate stopping criterion and recover the primal variables.

In order to decouple the constraints related to sparsity and low-rank we introduce the new variable $Y \in Q_{m(p+1)}$ and reformulate (6.9) as

$$\begin{aligned} & \min_{Z \in M_{m,p}} \Psi(C + \mathcal{T}(Z)) \\ \text{subject to} \quad & A(Z) \leq b, \quad (C_1) \\ & Y = \mathcal{T}(Z) + \lambda I, \\ & Y \succeq 0 \quad (C_2), \end{aligned} \tag{6.10}$$

where the first constraint (C_1) gathers the first two constraints on Z of (6.9) and A and b are defined accordingly; and (C_2) is the last constraint of (6.9) imposing positive semidefiniteness of the new variable Y . Using the *augmented Lagrangian* formulation, we introduce L_ρ defined by

$$\begin{aligned} L_\rho(Z, Y, M) = & \Psi(C + \mathcal{T}(Z)) - \langle M, Y - \mathcal{T}(Z) - \lambda I \rangle \\ & + \frac{\rho}{2} \|Y - \mathcal{T}(Z) - \lambda I\|_F^2, \end{aligned}$$

where $\|\cdot\|_F$ is the Frobenius norm. Subsequently, the ADMM updates are

$$\left\{ \begin{array}{l} Z^{k+1} = \min_{Z \in C_1} L_\rho(Z, Y^k, M^k), \\ Y^{k+1} = \min_{Y \in C_2} L_\rho(Z^{k+1}, Y, M^k), \\ M^{k+1} = M^k - \rho(Y^{k+1} - \mathcal{T}(Z^{k+1}) - \lambda I). \end{array} \right. \begin{array}{l} \text{(S1)} \\ \text{(S2)} \\ \text{(S3)} \end{array}$$

It should be noted that (S1) has no closed form solution and corresponds to the sparsity set of constraints defined in [Songsiri and Vandenberghe \(2010\)](#). We approximate the solution by a projective gradient step as in [Songsiri and Vandenberghe \(2010\)](#). Following this approach, the first update is obtained by

$$\begin{aligned}
Z^{k+1} &= \min_{Z \in C_1} L_\rho(Z, Y^k, M^k) \\
&= \min_{Z \in C_1} \Psi(C + \mathcal{T}(Z)) + \langle M^k, \mathcal{T}(Z) \rangle + \frac{\rho}{2} \|Y^k - \mathcal{T}(Z) - \lambda I\|_F^2 \\
&\approx \min_{Z \in C_1} \langle \Psi'(Z^k), Z - Z^k \rangle + \langle \mathcal{D}(M^k), Z \rangle + \rho \langle \mathcal{D}(\mathcal{T}(Z^k) + \lambda I - Y^k), Z - Z^k \rangle \\
&\quad + \frac{1}{2t_k} \|Z - Z^k\|_F^2 \\
&= \min_{Z \in C_1} \langle \Psi'(Z^k) + \mathcal{D}(M^k) + \rho \mathcal{D}(\mathcal{T}(Z^k) + \lambda I - Y^k), Z \rangle + \frac{1}{2t_k} \|Z - Z^k\|_F^2 \\
&= \min_{Z \in C_1} \langle \nabla_Z L_\rho(Z^k, Y^k, M^k), Z \rangle + \frac{1}{2t_k} \|Z - Z^k\|_F^2 \\
&= \min_{Z \in C_1} \|Z - (Z^k - t_k \nabla_Z L_\rho(Z^k, Y^k, M^k))\|_F^2 \\
&= \Pi_{C_1}(Z^k - t_k \nabla_Z L_\rho(Z^k, Y^k, M^k))
\end{aligned}$$

where

- $\nabla_Z L_\rho(Z^k, Y^k, M^k) = \nabla \Psi(Z^k) + \mathcal{D}(M^k) + \rho \mathcal{D}(\mathcal{T}(Z^k) + \lambda I - Y^k)$,
- t_k is found from the Armijo conditions,
- Π_{C_1} is the projection onto C_1 which reduces to a projection onto the l_1 -norm ball ([Berg et al., 2008](#); [Songsiri and Vandenberghe, 2010](#)).

The optimization problem (S2) has a closed form solution and is computed as

$$\begin{aligned}
Y^{k+1} &= \min_{Y \in C_2} L_\rho(Z^{k+1}, Y, M^k) \\
&= \min_{Y \in C_2} \langle M^k, Y \rangle + \frac{\rho}{2} \|Y - \mathcal{T}(Z^{k+1}) - \lambda I\|_F^2 \\
&= \min_{Y \in C_2} \|Y - \frac{1}{\rho} M^k - \mathcal{T}(Z^{k+1}) - \lambda I\|_F^2 \\
&= \Pi_{C_2}(\frac{1}{\rho} M^k - \mathcal{T}(Z^{k+1}) - \lambda I)
\end{aligned}$$

where Π_{C_2} is the projection onto the cone of symmetric positive semidefinite matrices of size $m(p+1) \times m(p+1)$, which is done by selecting the eigenvectors corresponding to *positive* eigenvalues. This leads to the final updates of the ADMM algorithm.

ADMM for sparse plus low-rank inverse power spectral density estimation. Initialize Z_0, Y_0, M_0 ; set $\rho > 0$; and successively update variables as follows:

$$\begin{aligned}
Z^{k+1} &= \Pi_{C_1}(Z^k - t_k \nabla_Z L_\rho(Z_k, Y_k, M_k)), \\
Y^{k+1} &= \Pi_{C_2}(\frac{1}{\rho} M^k - \mathcal{T}(Z^{k+1}) - \lambda I), \\
M^{k+1} &= M^k - \rho(Y^{k+1} - \mathcal{T}(Z^{k+1}) - \lambda I).
\end{aligned} \tag{6.11}$$

Following [Boyd et al. \(2011\)](#), a stopping criterion for (6.11) is based on the primal and dual *residuals* r and s that respectively measure satisfaction of the equality constraint of (6.10) and the distance between two successive iterates of the additional variable Y :

$$\begin{aligned} r &= \|(Y^{k+1} - \mathcal{T}(Z^{k+1}) - \lambda I)\|_F, \\ s &= \rho \|\mathcal{D}(Y^{k+1} - Y^k)\|_F. \end{aligned} \quad (6.12)$$

The algorithm stops when r and s satisfy $\|r\|_F \leq \epsilon^{pri}$ and $\|s\|_F \leq \epsilon^{dual}$ where ϵ^{pri} and ϵ^{dual} are defined as

$$\begin{aligned} \epsilon^{pri} &= m(p+1)\epsilon^{abs} + \epsilon^{rel} \max\{\lambda\sqrt{m(p+1)}, \|T(Z^k)\|_F, \|Y^k\|_F\}, \\ \epsilon^{dual} &= m\sqrt{p+1}\epsilon^{abs} + \epsilon^{rel} \|\mathcal{D}(M^k)\|_F. \end{aligned}$$

Here ϵ^{abs} and ϵ^{rel} are the predefined absolute and relative tolerances for the problem.

A variation is obtained when ρ is multiplied by a factor of $\tau > 1$ at each iteration up to a maximum value ρ_{max} starting from a value ρ_0 depending on the application.

6.3.1 Graphical model corresponding to the optimal solution

From an optimal solution Z_{opt} of (6.10) the interaction graph between the manifest variables is obtained from condition C1. Indeed, it is shown in [Songsiri and Vandenberghe \(2010\)](#); [Zorzi and Sepulchre \(2015\)](#) that:

$$\Sigma_{kh} = 0 \Leftrightarrow (D_j(X + L))_{kh} = 0 \quad \forall j = \{0, \dots, p\} \Leftrightarrow \sum_{j=0}^p (|(Z_j)_{kh}| + |(Z_j)_{kh}|) < \gamma\lambda, \quad (6.13)$$

where $D_j(X + L)$ denotes the j -th block of $\mathcal{D}(X + L)$. In other words there will be a direct connection between x_k and x_h if and only if the corresponding entry of the matrix sum computed in C1 of the reformulated dual (6.10) is strictly smaller than $\gamma\lambda$.

Then, the number of latent variables corresponds to the dimension of the nullspace of $V_{opt} = \lambda I + \mathcal{T}(Z_{opt})$ ([Zorzi and Sepulchre, 2015](#)), which is efficiently computed by identifying the number of eigenvalues of V_{opt} equal to zero.

Following these steps allows to identify the interactions between the manifest vari-

ables as well as the number of latent variables composing the graphical model, for a given set of the parameters (λ, γ) .

In order to discriminate between the different graphical models corresponding to different values of these weighting parameters, we compute a score function f taking into account fitting to the data and complexity of the model, defined in [Zorzi and Sepulchre \(2015\)](#) by:

$$f(m, l, \Phi_m, \Phi_C) = \mathbb{D}(\Phi_C || \Phi_m) \times p, \quad (6.14)$$

where Φ_C is the smoothed correlogram of x^m ([Stoica and Moses, 1997](#)) estimated from the data, Φ_m is the power spectrum estimated from the model, p is the total number of edges in the latent-variable graphical model, and $\mathbb{D}(\Phi_C || \Phi_m)$ is the *relative entropy rate* ([Cover and Thomas, 1991](#)) measuring the matching of Φ_m to the data:

$$\mathbb{D}(\Phi_C || \Phi_m) = \frac{1}{2} \left(\int (\log \det(\Phi_C^{-1} \Phi_m) + \langle \Phi_C, \Phi_m^{-1} \rangle) - m \right). \quad (6.15)$$

Finally, convergence analysis of the ADMM algorithm follows from ([Ouyang et al., 2014; Boyd et al., 2011](#), Section 3.2). The computational cost per iteration of the updates (6.11) depends on the projections onto C_1 and C_2 , the gradient evaluation of L_ρ , and the linear mappings \mathcal{T} and \mathcal{D} leading to a final complexity $\mathcal{O}(m^3(p+1)^3)$. Considering that usually the order or the autoregressive models, p , is relatively small, this complexity allows to deal with values of m ranging from several hundreds up to a thousand which are the dimensions typically encountered in fMRI applications.

6.4 Results

In this Section we apply the proposed ADMM algorithm to solve the sparse plus low-rank decomposition on synthetic and real datasets. The Matlab code for the algorithm is available from the webpage <http://www.montefiore.ulg.ac.be/~rliegeois/>.

6.4.1 Application on linear synthetic data

This synthetic dataset consists of time series corresponding to a first order AR model (dynamic model, $p = 1$) with the interaction graph presented in Figure 6.1. The interaction graphs of the manifest variables (support of Σ) identified for different values of λ and $\lambda\gamma$ are represented in Fig. 6.2 as well as l , the number of latent components (rank of Λ) that were identified.

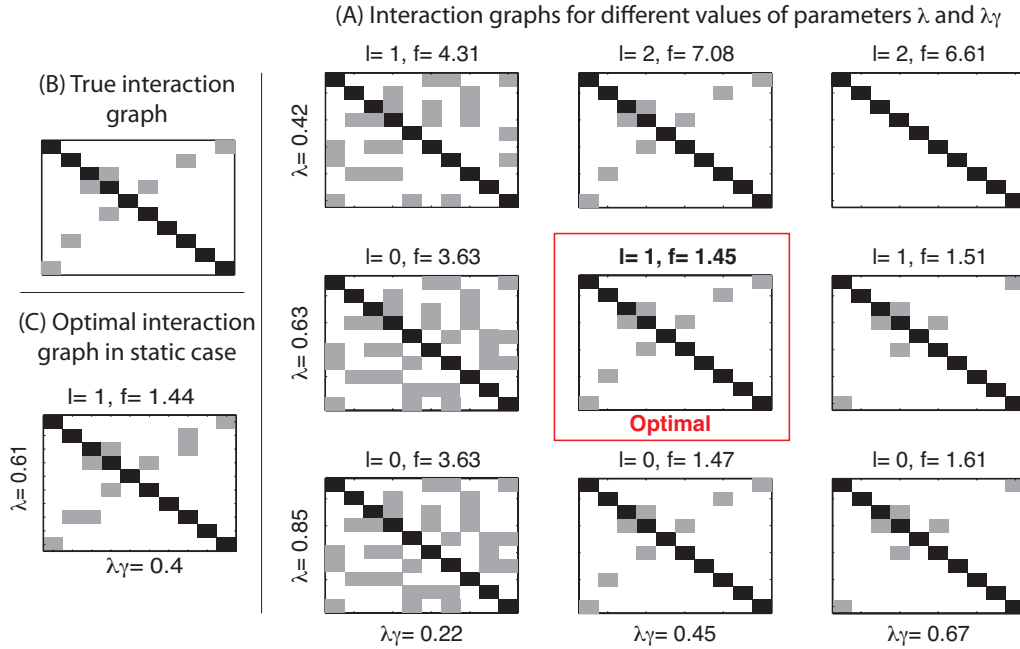


Figure 6.2 – (A) Interaction graphs of estimated models for different values of λ and $\lambda\gamma$ using a first order AR model ($p = 1$). (B) True interaction graph. (C) Optimal interaction graph of estimated model obtained in the static case ($p = 0$).

As expected, higher values of λ promote models with less latent components, and higher values of $\lambda\gamma$ favor models with few interactions between the manifest variables. The model with the best (lowest) score function recovers the true interaction graph with the correct number of latent components (Fig. 6.2A). The optimal interaction graph in the static case (Fig. 6.2C), on the contrary, does not recover exactly the true interaction graph.

It should be noted that the information encoded in the latent variables is not fully exploited in the results presented in Figure 6.2. Indeed, we limit the analysis to considering the *number* of latent variables identified for a specific set of weighting parameters whereas the *weight* of each latent variable in each manifest variable is not used. This limitation is the main motivation of the work developed in Chapter 7.

The stopping criterion based on the primal and dual residuals is illustrated in Fig. 6.3 using this dataset.

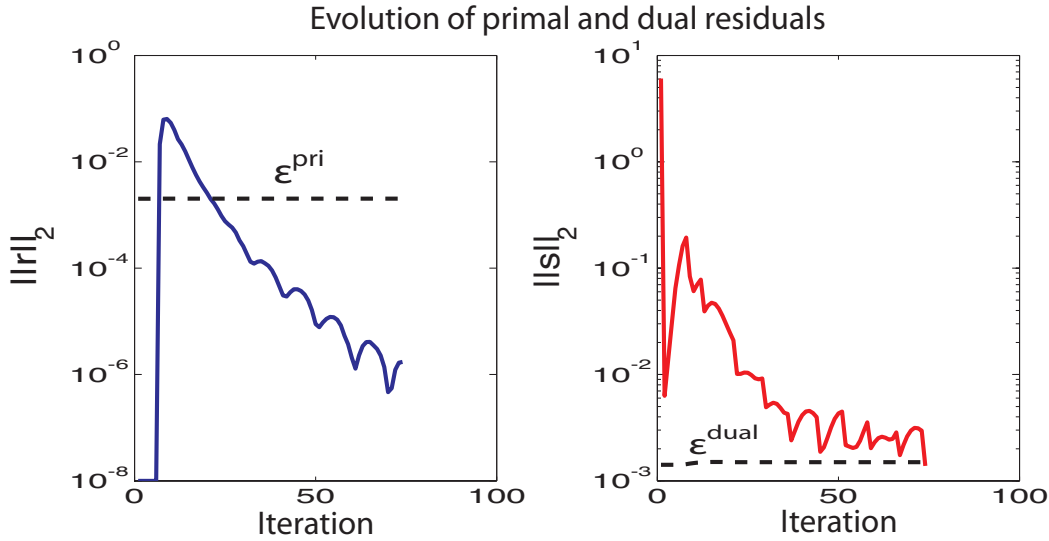


Figure 6.3 – Typical convergence scheme of the ADMM algorithm obtained with the linear synthetic dataset with the parameter values $\rho_0 = 1$, $\tau = 1.1$, $\rho_{max} = 1000$, $\epsilon^{abs} = 10^{-5}$, and $\epsilon^{rel} = 10^{-4}$.

The algorithm stops when $\|r\|_2 \leq \epsilon^{pri}$ and $\|s\|_2 \leq \epsilon^{dual}$ are both satisfied, meaning that constraint (6.10) is satisfied and that the additional variable Y allowing the decoupling of the two constraint sets $C1$ and $C2$ has converged.

6.4.2 Application on real data

We illustrate the application of our proposed algorithm on real neuroimaging data consisting of functional magnetic resonance imaging time series in 90 brain regions collected on 18 patients during rest (Vanhaudenhuyse et al., 2011). Let us remind here that even during rest, the brain shows coherent spatially organised connectivity patterns, also called resting-state networks (e.g. Moussa et al., 2012).

It should be noted that this problem dimension is not tractable with a standard optimization tool such as the CVX toolbox of (Grant et al., 2005) which are able to solve problems containing up to 20 variables in a reasonable time (less than a day).

The optimal graphical models identified for different values of λ and γ are represented in Figure 6.4.

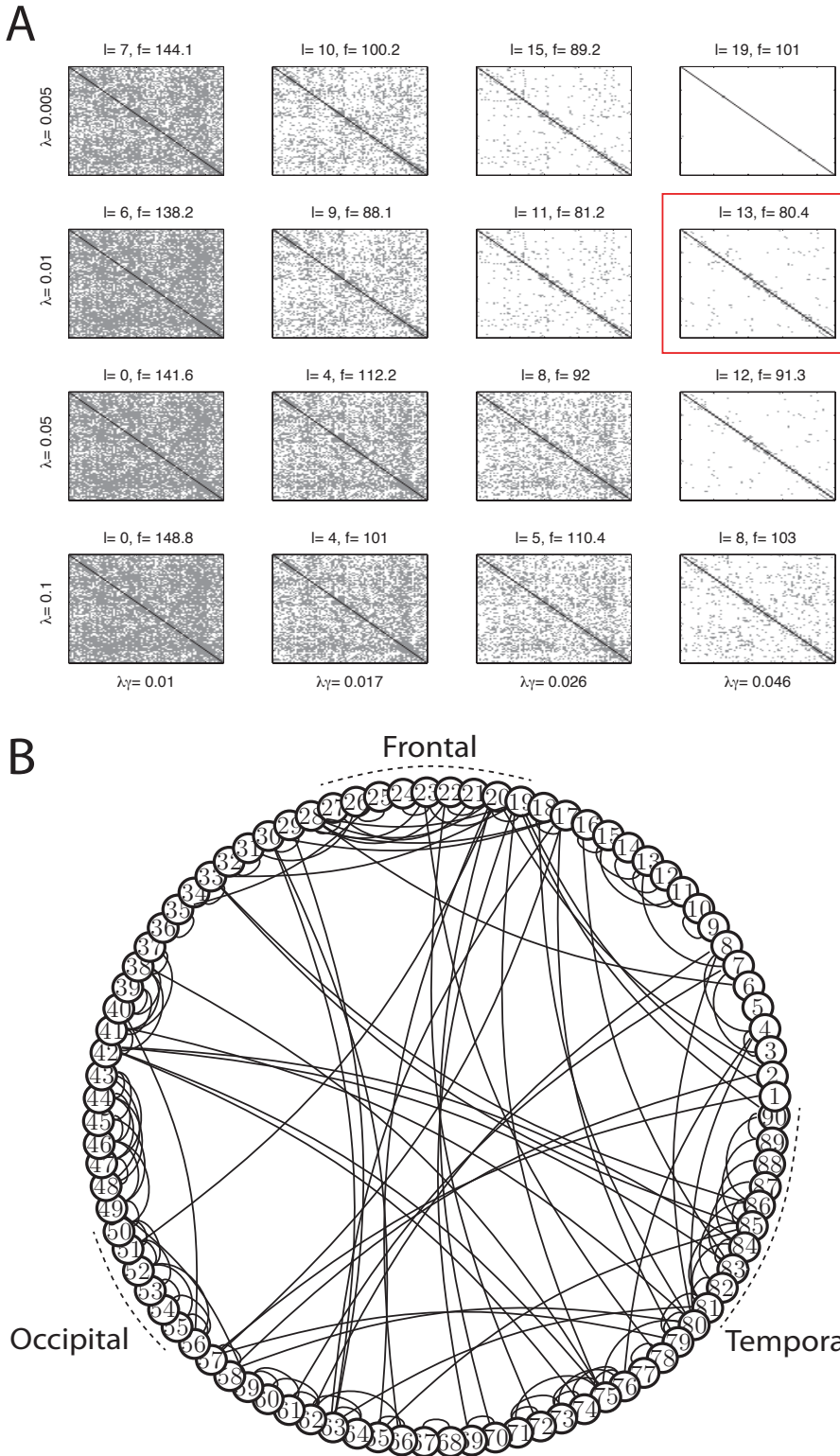


Figure 6.4 – (A) Interaction graphs of estimated models for different values of λ and $\lambda\gamma$ using a first order AR model ($p = 1$) and optimal model. **(B)** Developed representation of the interactions between the manifest variables in the optimal model, latent variables are not represented.

We observe that the optimal number of latent variables l is 13 which is on the same order than the number of networks that are identified using classical component analysis. In addition to the latent variables, the optimal model shows residual interactions mainly happening within spatial clusters such as frontal regions (19-27), occipital regions (50-55) and temporal regions (81-90). This suggests that the latent variables primarily capture interactions linking many regions and happening at the whole-brain level, whereas the few direct interactions within spatial clusters are preferably gathered in the sparse contribution of the S+L decomposition.

Once again this echoes what is observed in component analysis where the components capture some common statistical behaviour characterising many and possibly remote cerebral regions. This is an additional motivation for exploring the interpretation of the low-rank contribution as a dynamic extension of component analysis which we develop in Chapter 7.

6.5 Discussion

The contribution presented in this Chapter first lies in the formulation of the low-rank plus sparse estimation of the inverse power spectral density optimization problem (6.3) into the alternating direction method of multipliers (ADMM) framework. Second we apply this decomposition to resting-state fMRI time series capturing cerebral BOLD activation in 90 different regions.

Considering the latter we show that the proposed algorithm is able to deal with this problem dimension that is not tractable with previously available tools. Results of Figure 6.4 show that the presence of an additional latent variable allows to remove a significant number of direct interactions between the manifest variables. The most stable direct interactions constituting the sparse part of the decomposition seem to be highly spatially defined (Figure 6.4B). On the contrary, latent variables capture common behaviours in possibly remote brain regions, which is typically observed using component analysis. This interpretation of the low-rank part of the decomposition requires a detailed description that is provided in Chapter 7.

We now focus on the computational considerations of the proposed algorithm, highlight some of its limitations and propose some ways to improve its scalability to larger datasets.

6.5.1 Going beyond cubic complexity

As already mentioned the computational complexity of the proposed ADMM algorithm is $\mathcal{O}(m^3(p+1)^3)$ where m is the number of variables and p the order of the AR model that is identified. Thanks to the decoupling of the low-rank and sparsity constraints exposed in (6.10) we were able to keep the same complexity as the one of the algorithm presented in [Songsiri and Vandenberghe \(2010\)](#), despite the additional low-rank constraint. We here ask whether we could expect better scalability of our algorithm by exploiting its low-rank plus sparse structure.

Indeed, recent work has for example emphasised the possibility of exploiting the sparse structure of the optimal solution in the *static* case ($p = 0$), leading to efficient algorithms with $\mathcal{O}(m^2)$ complexity (e.g. [Hsieh et al., 2014a,b](#)). These algorithms solve the *primal* optimization problem in which the variables encode the sparsity constraint, thereby allowing to exploit sparsity directly within the optimization scheme. In the *dynamic* case presented here ($p > 0$), on the contrary, sparsity of the sum $X + L$ needs to be *structured* in order to translate into sparsity of the corresponding inverse power spectral density Σ ([Songsiri and Vandenberghe, 2010](#)). This structured sparsity is induced by the function h defined in (6.8) which is convex but non-smooth thereby preventing from solving on the primal. In the dual formulation (6.9), equation (6.13) shows that structured sparsity translates into non-tightness of (C1) and sparsity can therefore not be exploited directly in the resolution of the proposed formulation of the algorithm, in the sense that the corresponding values of the optimization variables are not equal to zero.

Another improvement proposed in [Hsieh et al. \(2014a\)](#) is the partition of the variable space into an *active* and a *fixed* subspace. At each iteration an active subspace is determined and the adequate update takes place only within this subspace, leaving the fixed subspace unchanged. This procedure allows to significantly decrease the size of variables while keeping strong convergence properties. However, this approach is shown to be valid for l_1 - or nuclear norm regularizers, or a combination of these. Hence once again this approach does not directly apply for solving the primal (6.7) due to the use of the structured sparsity inducing norm h .

We have also examined the possibility of exploiting the block-Toeplitz structure of the variables denoted by $\mathcal{T}(Z)$ in (6.9). However, even if the properties and inversion of Toeplitz matrices have been intensively studied (e.g. [Reichel and Trefethen, 1992](#); [Martinson et al., 2005](#)), *block*-Toeplitz matrices have attracted less attention. We here propose two ways of exploiting this particular structure. The first one is based on recent results showing that Toeplitz matrices with linearly increasing entries can be inverted with linear complexity ([Bünger, 2014](#)). Our preliminary testings suggest that these results can be extended to block-Toeplitz matrices. However, additional work should be done in order to

define how the condition of Toeplitz matrices with “linearly increasing entries” of Bünger (2014) translates in the block-Toeplitz case. This condition might be reasonable in our application because it could be related to the fact that further time points have less influence in the expression of the current time point. However, this interpretation should be further explored and assessed before use.

Second, the approximation of Toeplitz matrices by circulant matrices has also been widely studied because circulant matrices are closely related to Fourier analysis, leading to efficient inversion (Gray, 2005; Ringh and Karlsson, 2015). Once again, these results should be extended to block-Toeplitz and block-circulant matrices in order to be used in this context.

It should finally be noted that exploiting sparsity of the primal variables or their decomposability into *active* and *free* learning subspaces seems more promising in terms of complexity improvements compared to exploiting the block-Toeplitz structure of the dual variables. Indeed, the former could decrease the contribution of m in the global complexity, whereas the latter could decrease the contribution of p . Since $p \ll m$, the most promising improvements are obviously expected from decreasing the complexity due to m compared to decreasing the complexity due to p .

6.5.2 Accuracy requirements of the proposed decomposition

In order to recover the primal optimal variables (X_{opt}, L_{opt}) from an optimal solution Z_{opt} of the dual (6.9), as reminded in Section 6.3.1 it is necessary to identify the nullspace of $V_{opt} = \lambda I + \mathcal{T}(Z_{opt})$ (Zorzi and Sepulchre, 2015). This is done by computing the eigenvectors corresponding to the zero eigenvalues of V_{opt} . It appears that these eigenvalues can be in certain cases quite sensitive to the accuracy required on the primal and dual residuals defined in (6.12) as well as to the threshold used to identify the zero eigenvalues of V_{opt} . Hence, even if the primal cost is not significantly changed when the required accuracy is changed, the corresponding graphical model can be significantly modified.

Considering this, let us note that ADMM generally achieves an intermediate precision in a few iterates but can be slow if a high accuracy is required (Boyd et al., 2011). Hence it should be further studied whether the level of accuracy naturally provided by the ADMM framework is sufficient in this application. We might reasonably assume that the modifications of the optimal graphical model due to a mild change in the prementioned thresholds and accuracy requirements are in some statistical sense not meaningful, but this should be assessed and is left for future work.

6.6 Conclusion

The contribution of this Chapter consists in the reformulation of the sparse plus low-rank autoregressive identification problem into the ADMM framework in order to scale it to larger datasets encountered in neuroimaging applications. To do so, separability of the low-rank and sparse constraints is exploited and allows to build upon previous work to solve the subproblem corresponding to the sparsity constraint. The remaining subproblem resulting from the low-rank constraint then reduces to a well known projection onto the cone of positive semidefinite matrices.

We then illustrate the performance of our proposed algorithm on a synthetic dataset and on a real neuroimaging dataset consisting of fMRI time series acquired in 90 brain regions which is too large to be analysed using standard available optimization tools. The optimal model of the interactions between the variables corresponds to a balance between a low-rank subspace of variation explaining common features in several variables, and some local connectivity not sufficiently spread to be encoded in an additional latent variable and resulting in some sparse interactions.

We detail in the last Section different possibilities to improve the scalability of our algorithm as well as the reasons why we were not able to implement them. Considering the large amount of recent literature on this topic, we might reasonably assume that the present basic formulation is the first step towards more efficient algorithms further exploiting its particular structure.

CHAPTER 7

From latent variables to dynamic component analysis

We have seen in Chapter 6 that the properties of the latent variables identified in the proposed S+L decomposition echo the properties of components identified in component analysis. This Chapter explores this link and motivates the interpretation of the low-rank part of this S+L decomposition as a dynamical extension of component analysis. The main results presented here are based on the last part of the following paper.

R. Liégeois, B. Mishra, M. Zorzi, and R. Sepulchre. *Sparse plus low-rank autoregressive identification in neuroimaging time series*. Accepted at the 54th IEEE Conference on Decision and Control, Osaka, December 2015.

7.1 Introduction

In the context of graphical models, *latent variables* allow to identify common patterns in several variables, as illustrated in Figure 6.1 of the previous Chapter. This interpretation echoes the primary motivation of *component analysis* which is to identify groups of variables sharing specific features. Even though the corresponding generative models are different, we explore in this Chapter the extent to which the low-rank plus sparse decomposition presented in Chapter 6 can be seen as an extension of classical component analysis techniques.

In the next Section we first recall the basic motivations of component analysis. We then describe the two most common versions of component analysis approaches: principal component analysis and independent component analysis. We finish by motivating the use of these techniques for analysing neuroimaging time series.

We then define *latent components*, derived from latent variables. Their properties are compared to the ones of principal and independent component analysis.

7.2 Component analysis

Highlighting hidden features in large datasets is a key challenge in data mining applications going from economics to bioinformatics or medical imaging. Let us consider $x_i(t)$ a dataset with $i \in \{1, \dots, m\}$ and $t \in \{1, \dots, N\}$. This dataset can be considered as a set of m initial random variables with N observations for each of them. Given this dataset component analysis aims at finding a better representation of the set according to some specific criteria. For computational reasons and in order to build on all the results of matrix theory, the best representation is searched among the linear transformations of the data:

$$y_i(t) = \sum_{j=1}^m w_{ij} x_j(t) \quad \forall i = \{1, \dots, l\}, \quad (7.1)$$

where the w_{ij} are the coefficients that determine the linear transformation and l the number of variables in the new space of representation. We can rewrite (7.1) in a matrix form as follows:

$$\mathbf{Y}_{l,N} = \mathbf{W}_{l,m} \mathbf{X}_{m,N}, \quad (7.2)$$

where $\mathbf{X}_{m,N}$ is the initial dataset in a m -dimensional space, $\mathbf{Y}_{l,N}$ is the new representation of the dataset in a l -dimensional space with $l \leq m$, and $\mathbf{W}_{l,m}$ is the matrix that expresses the base changement from the m to l -dimensional space.

Depending on the criterion chosen to determine \mathbf{W} several variants of component analysis have been developed. We here present the generative models and corresponding properties of two familiar techniques: principal component analysis (PCA) and independent component analysis (ICA).

7.2.1 Principal and independent components

PCA and ICA share the objective of representing the original dataset in a new, more interpretable space. However, these approaches are very different both in the underlying

assumptions, or generative model, and in their applications. On the one hand the primary goal of PCA is to identify a subspace that captures most of the information contained in the data, in this case we have $l < m$. On the other hand ICA first aims at solving the so-called *blind source separation problem* in which the reconstruction of the original signals is central, without identifying a subspace or reducing dimensionality of the data (Hyvärinen et al., 2001). We now describe the corresponding generative models of PCA and ICA.

PCA assumes that the initial variables are *gaussian*, and consequently, that they can be completely characterised by their first two statistical cumulants: their mean and covariance matrix. For centered data, finding a subspace capturing the highest amount of information about the dependencies between the variables then naturally translates into finding a subspace of maximum variance. In this case the lines of $\mathbf{W}_{l,m}$ in (7.2) encode *orthogonal* directions onto which the projection of the data $\mathbf{X}_{m,N}$ has the largest variance (Jolliffe, 2002).

ICA, on the contrary, looks for non-gaussian original variables. This is because non-gaussianity is used as a measure of *independence* between the variables. Indeed, the central limit theorem states that a mixture of independent variables tends to converge towards a gaussian distribution (Laplace, 1809). Hence in order to recover the true underlying variables ICA looks for a linear transformation of the data that results in the least gaussian components (lines of $\mathbf{Y}_{l,N}$). Non-gaussianity is in this context commonly evaluated by the *kurtosis* of the variables which exploits the fourth order cumulant of the variables (see Hyvärinen et al. (2001) and Appendix B). Since measures of non-gaussianity are scale-free, ICA is not well suited to reduce dimensionality of the initial dataset because it is not possible to rank the importance of different components, as in PCA. Let us now define the notion of statistical independence:

Definition 7.2.1 *Two random variables are statistically independent if and only if their joint probability equals the product of their probabilities.* ◇

Difficulty arises from the fact that independence is not measurable in an easy way for non-gaussian variables. Indeed, this requires to completely characterize the random variables by considering all their cumulants and not the two first ones as for orthogonality in the case of PCA. Considering this, ICA can be seen as an extension of PCA (Comon, 1994).

This definition also results in the fact that independence implies orthogonality for centered variables but the converse is in general not true. However, in the case of jointly gaussian variables independence is equivalent to orthogonality because the variables can be entirely described by their first two cumulants.

The above paragraphs can be summarised as follows: PCA assumes a gaussian framework and is mostly used in order to reduce the dimensionality of the data whereas ICA

models the data as a mixture of signals identifiable because of their non-gaussianity. The interested reader will find in Appendix B some specific examples of application of PCA and ICA on gaussian and non-gaussian datasets, providing deeper insight about the properties of the original datasets that are exploited by each technique.

7.2.2 Component analysis for neuroimaging applications

As already mentioned neuroimaging datasets generally consist of time series recorded in different cerebral regions. In this context component analysis techniques assume that the initial dataset is the linear superposition of several principal or independent components. This modelling assumption has a straightforward neurological interpretation as it has been shown that some of these components capture distinct cerebral processes. Hence the identified components were called *neuronal networks*. At rest, we can for example identify the visual, the sensory motor, or the default mode networks ([Moussa et al., 2012](#)).

Both principal component analysis ([Andersen et al., 1999; Viviani et al., 2005; Suma and Murali, 2007](#)) and independent component analysis ([McKeown et al., 1998; Calhoun et al., 2001; Anemüller et al., 2006](#)) were extensively used in order to extract neuronal networks from the initial data. Pros and cons of these approaches have been debated and it came out that PCA is a preferred preliminary step performed to reduce the dimensionality of the dataset, or in other terms remove noise. On the contrary ICA has become a gold standard for the final identification of the neuronal networks because this decomposition is more robust to different perturbations encountered in neuroimaging data, and able to disentangle neuronal from non-neuronal information ([Liégeois, 2011](#)).

Considering the properties of PCA and ICA highlighted in Section 7.2.1, it is reasonable to think that the non-gaussianity assumption made for ICA is crucial in order to extract neuronal networks, for two main reasons. First, neuronal networks are usually sparse, meaning that few regions are activated within the network. The distribution of these networks is highly non-gaussian (it is *super*-gaussian, see Figure B.1), and ICA will be naturally well suited to identify such networks ([Daubechies et al., 2009](#)). Second, the neuronal networks exhibit temporal structure, they are for example oscillating at specific frequencies ([Gusnard et al., 2001; Greicius et al., 2003](#)). This structure also translates into a non-gaussian distribution of the corresponding density (see for example the distribution of the sinusoidal signal o_2 in Figure B.3) which can be efficiently recovered by ICA, even if ICA, as PCA, relies on a *static* generative model.

We describe in the next Section the properties of the low-rank contribution in the low-rank plus sparse decomposition presented in Chapter 6. In light of the properties of ICA and PCA presented in this Section we explore what type of information is captured by the

latent variables composing this low-rank contribution. Since the corresponding generative model is *gaussian* and *dynamic*, we specifically discuss the potential benefits of going from a *static* to a *dynamic* framework.

7.3 Characterizing Latent Variables

Historically, the covariance selection problem¹ was first blended with sparsity constraints modelling the presence of few direct interactions between the manifest variables ([Dempster, 1972](#)). The low-rank structure modelling the presence of latent variables that are not observed but generating a common behavior in the manifest variables was introduced later (e.g. [Chandrasekaran et al., 2010](#)). It was shown that adding a latent variable in a model often allows to remove several direct interactions, thereby simplifying in some sense the corresponding graphical model ([Zorzi and Sepulchre, 2015](#)). Surprisingly, the interpretation of the low-rank contribution in such decompositions has to our knowledge not been further studied.

Consider for example the graphical model of Figure 7.1.

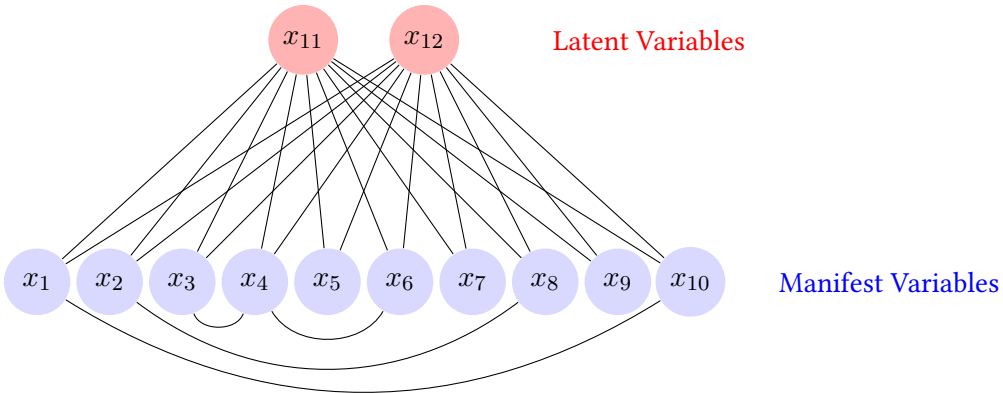


Figure 7.1 – Ten observed variables $x_i, i \in [1 \dots 10]$ with few interactions among them (sparse structure) and two latent variables x_{11} and x_{12} (low-rank structure).

From this representation no distinction can be done between the two latent variables, and usually only the number of latent variables identified in a model is provided without further characterisation, as in Figures 6.2 and 6.4 or in [Zorzi and Sepulchre \(2015\)](#). However, one might reasonably ask where the difference between the two latent variables is encoded. Indeed, if the two variables were encoding the same information, capturing the

¹ The derivation of this well known problem is derived for information in Section 2.2.2

same set of interactions between the observed variables, the two latent variables would obviously be merged into the same latent variable.

Before entering the details of how to recover information encoded in the latent variables, let us recall that the inverse power spectral density of the manifest variables, according to the identification procedure (6.7), can be written as:

$$\Phi_m^{-1}(e^{j\theta}) = \Sigma(e^{j\theta}) - \Lambda(e^{j\theta}), \quad (7.3)$$

where $\Sigma(e^{j\theta})$ is sparse, meaning that some of its entries are identically equal to zero, for all $\theta \in [0, 2\pi]$, and Λ is low-rank, where the rank is defined as follows.

Definition 7.3.1 *The rank - called normal rank - of a power spectral density is computed by:*

$$\text{rank}(\Lambda) = \max_{\theta \in [0, 2\pi]} \text{rank}(\Lambda(e^{j\theta})). \quad (7.4)$$

◊

7.3.1 Definition of latent components

Λ_{opt} is a square matrix function of size m , defined over the unit circle. Since Λ_{opt} is low-rank for all $\theta \in [0, 2\pi]$ as defined by (7.4) we consider its pointwise singular value decomposition:

$$\Lambda_{m,m}^{opt}(e^{j\theta}) = \Gamma_{m,l}(e^{j\theta})\Omega_{l,l}(e^{j\theta})\Gamma_{m,l}^*(e^{j\theta}). \quad (7.5)$$

This decomposition is not unique, as precised in [Zorzi and Sepulchre \(2015\)](#), but it is unique provided diagonality is imposed on $\Omega_{l,l}(e^{j\theta})$. Since $\Omega_{l,l}$ encodes dependencies between the latent variables as defined in (6.1), such a constraint is reasonable because we are interested in identifying latent variables that are (conditionally) independent from each other.

Regarding $\Gamma_{m,l}(\theta)$ - $\Gamma_{m,l}(\theta)$ and $\Gamma_{m,l}(e^{j\theta})$ are equivalent notations-, its i -th column contains the strength of the conditional dependence relation between the i -th unobserved latent variable and each of the m manifest variables. Following component analysis nomenclature ([Jolliffe, 2002](#)) we define *latent components* as follows:

Definition 7.3.2 *The i -th latent component of a graphical model, with $i \in \{1, \dots, l\}$, is the i -th column of $\Gamma_{m,l}(\theta)$. It is denoted $\gamma_{i,.}(\theta)$.* ◊

In other words, $\gamma_{i,j}(\theta)$ with $i \in \{1, \dots, l\}$ and $j \in \{1, \dots, m\}$ represents the weight of the conditional dependence between the latent variable $x_{m+i}(t)$ and the manifest variable $x_j(t)$ in the expression of $x_j(t)$, and can be considered as the weight associated to the edge linking $x_{m+i}(t)$ and $x_j(t)$ in Figure 7.1. In the static case, $\gamma_{i,.}(\theta)$ reduces to a constant vector because $\Delta = I$ in (6.4) and hence Λ does not depend on θ . On the contrary, in the dynamic case each latent component is a function of $\theta \in [0, 2\pi]$.

This interpretation of the elements of the latent components echoes the one of independent or principal components, for which each entry corresponds to the contribution of the variable in the component (Liégeois, 2011).

7.3.2 Linking latent components and component analysis

It can be shown (Zorzi and Sepulchre, 2015) that the optimization problem (6.9), solved to identify a sparse plus low-rank decomposition of the inverse power spectral density Φ_m^{-1} , can be reformulated as a maximum entropy problem of the form:

$$\begin{aligned} \max_{\Phi_m} \quad & \int \log \det \Phi_m \\ \text{subject to} \quad & \mathcal{C}(\Phi_m, \hat{R}), \end{aligned} \tag{7.6}$$

where $\mathcal{C}(\Phi_m, \hat{R})$ gathers the structural constraints on Φ_m and the matching constraints to the data encoded in the experimental covariance lags \hat{R} (Stoica and Moses, 1997).

Interestingly, it has been shown that principal component analysis can also be seen as a maximum entropy problem (Paiva et al., 2006; He et al., 2011). Let us also note that since the variables x_i with $i \in \{1, \dots, m+l\}$ are assumed to be gaussian (Zorzi and Sepulchre, 2015), independence in this case reduces to orthogonality.

Considering these elements, the proposed low-rank plus sparse decomposition can be seen as an extension to dynamical models of component analysis, rooted similarly to principal component analysis as all the variables (manifest and latent) are assumed to be gaussian, and the corresponding optimization problems are closely related. However, the temporal structure of the variables is also taken into account in our proposed framework, and in this sense our approach could also be related to independent component analysis as this approach also partly recovers this information, as highlighted in Section 7.2.2.

7.4 Results

We first illustrate the information encoded in the latent *components* on a synthetic dataset. Building upon these preliminary results, we then perform the same analysis on real fMRI time series coming from healthy subjects undergoing different states of consciousness already studied in Chapter 5.

7.4.1 Application on nonlinear synthetic data

Considering a nonlinear generative model allows to produce endogenous sustained oscillations in networks similarly to what is observed in neuroimaging data, which presents a double advantage. First it allows to generate synthetic datasets with specific temporal structure which, as we show, can be at least partly recovered by the latent components. Second, having a generative model different from the one of the proposed decomposition procedure provides better insight about its robustness and applicability to real datasets. A popular nonlinear model, that we use to generate the synthetic dataset, is the Hopfield model widely used in neural networks Hopfield (1982):

$$\dot{x}_i = -x_i + \text{sat}\left(\sum_{j \neq i} G_{ij} x_j\right) + \epsilon, \quad (7.7)$$

where x_i denotes the level of activity of the variable i , G_{ij} is the strength of the connection from x_j to x_i , and $\text{sat}()$ is a sigmoidal saturation function. Figure 7.2 shows how we generate oscillations in two clusters for different values of the coupling parameters G_{ij} .

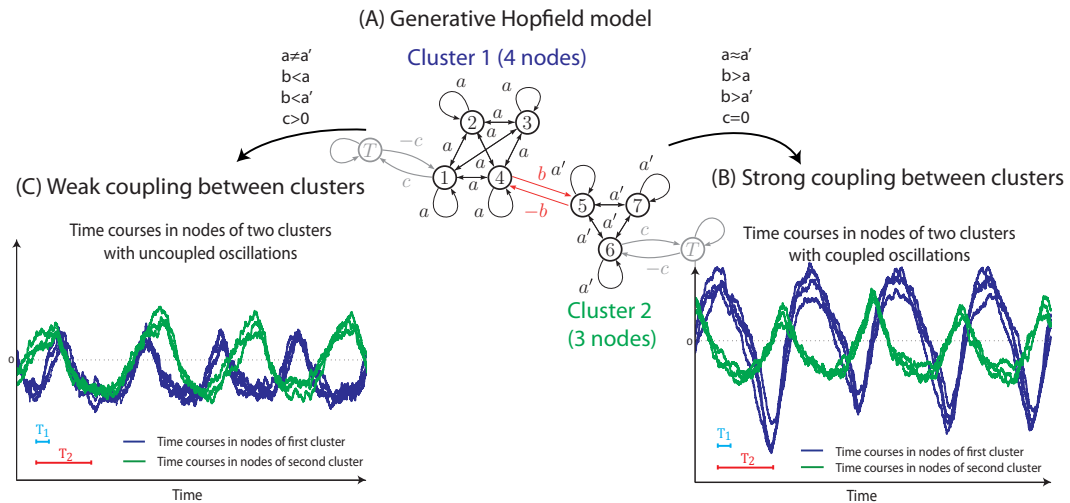


Figure 7.2 – (A) The generative model contains two clusters and the values of the directed connectivity between the nodes is indicated on the corresponding arrows. These values correspond to the matrix G in (7.7). (B) Set of parameters leading to coupled oscillations and (C) decoupled oscillations.

In the first case (Figure 7.2B) the oscillations are coupled, leading to dephased oscillations of the same frequency whereas in the second case the clusters are decoupled (Figure 7.2C), leading to oscillations of different frequencies in the two clusters. We finally generate three different datasets for each configuration by sampling these time series at different frequencies. The first dataset is produced by using the original time series (no sampling), the second and third datasets are obtained by sampling the time series with a period of T1 and T2 to generate synthetic data with higher frequency content. We identify a *static* model ($p = 0$) and a *dynamic* model to the datasets presented in Figure 7.2 B & C.

Figure 7.3 shows the static and dynamic latent components as defined in Section 7.3.1 that are identified in the optimal models from the synchronous oscillations datasets of Figure 7.2B. Since the results are very similar within the nodes of each cluster and for clarity purposes we plot only the value of the latent components in node 1 ($\gamma_{i,1}$) and in node 5 ($\gamma_{i,5}$).

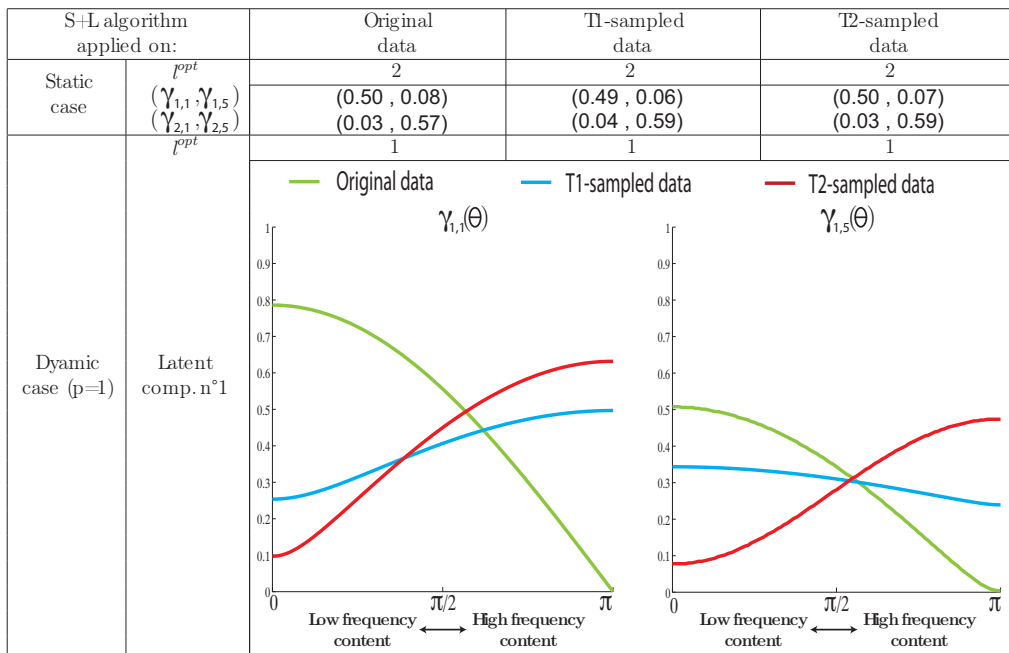


Figure 7.3 – Latent components identified in the static and dynamic cases from the three datasets generated from coupled oscillators (Figure 7.2 B).

In the static case (upper rows of Figure 7.3) two latent components corresponding to the two clusters of the generative model are identified. There is no significant difference for the three input datasets suggesting that the frequency content of original data is not encoded in the static latent components.

In the dynamic case ($p = 1$, last row of Figure 7.3), the latent components are encoded

in $\gamma_{i,j}(\theta)$ and a single latent component, function of θ , is identified in the optimal model.

In this case, the latent components are influenced by the sampling rate applied on the original time series. The T2-sampled synthetic data (high-frequency time series) leads to a latent component showing a strong high-frequency content whereas the original dataset leads to a latent component with dominant low-frequency content.

Having the same approach on asynchronous oscillations, we get the results shown in Figure 7.4.

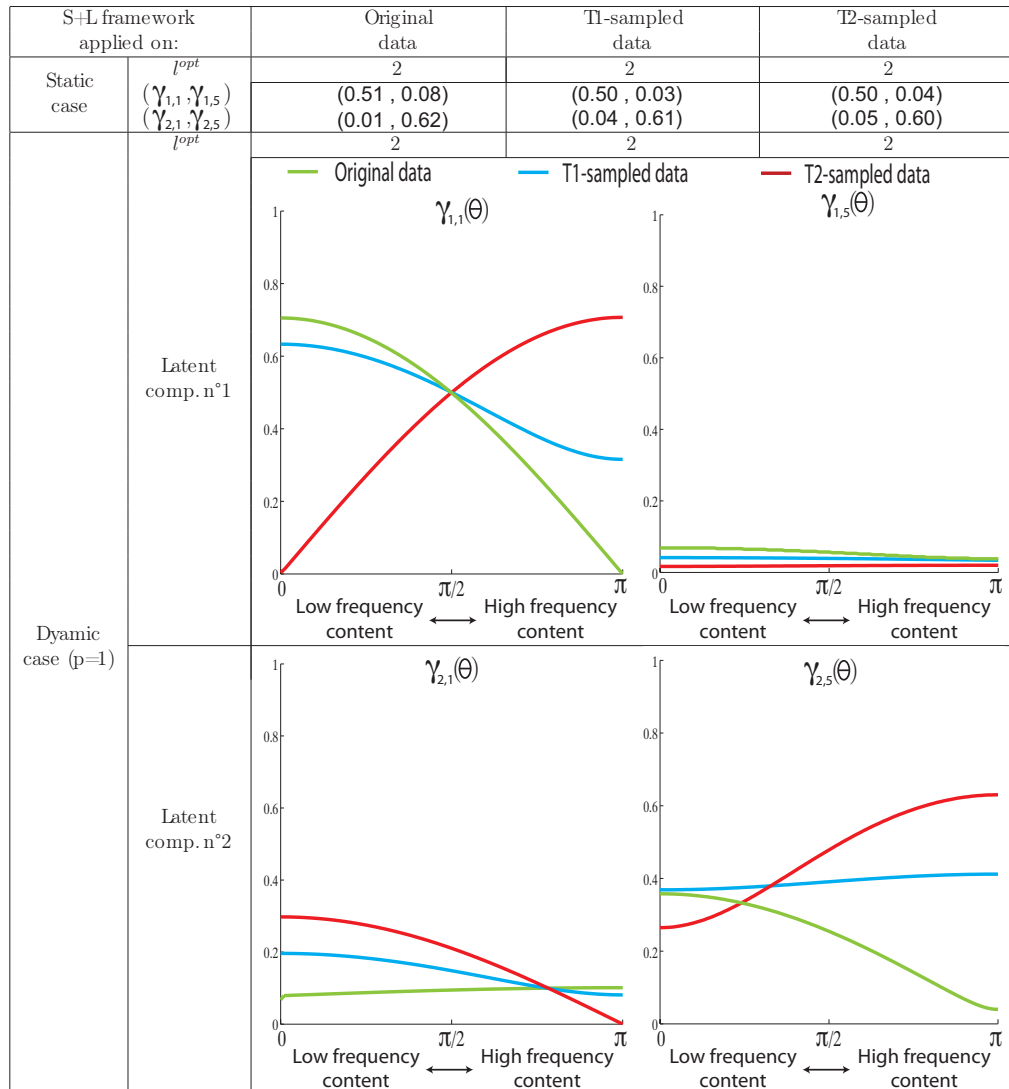


Figure 7.4 – Latent components identified in the static and dynamic cases from the three datasets generated from decoupled oscillators (Figure 7.2C).

In the static case we still obtain two latent components recovering the two clusters with no distinction between the three starting datasets. In the dynamic case ($p = 1$), however, the optimal model now has two latent components, each one capturing the oscillations in one of the two clusters.

As in the previous case the frequency content of the synthetic data is encoded in the frequency content of the latent component. Identifying two latent components in the case of unsynchronised clusters, as opposed to only one component identified in the case of synchronised clusters, probably comes from the fact that the frequency of oscillation in the two clusters are different, suggesting that the dynamic latent component identifies a *spatio-temporal* subspace of variation common to different manifest variables.

7.4.2 Application to neuroimaging data

We illustrate the application of the proposed algorithm on real neuroimaging data consisting of functional magnetic resonance imaging time series in 90 brain regions collected on 17 patients during rest [Vanhoudenhuysse et al. \(2011\)](#). It should be noted that this problem dimension is not tractable with a standard optimization tool such as the CVX toolbox of [Grant et al. \(2005\)](#). The classical approach is to use component analysis to extract neuronal networks. During rest, three networks are robustly identified using component analysis: the visual network (VIS), the default mode network (DMN) and the executive control network (EXN) that are represented in Fig 7.5.

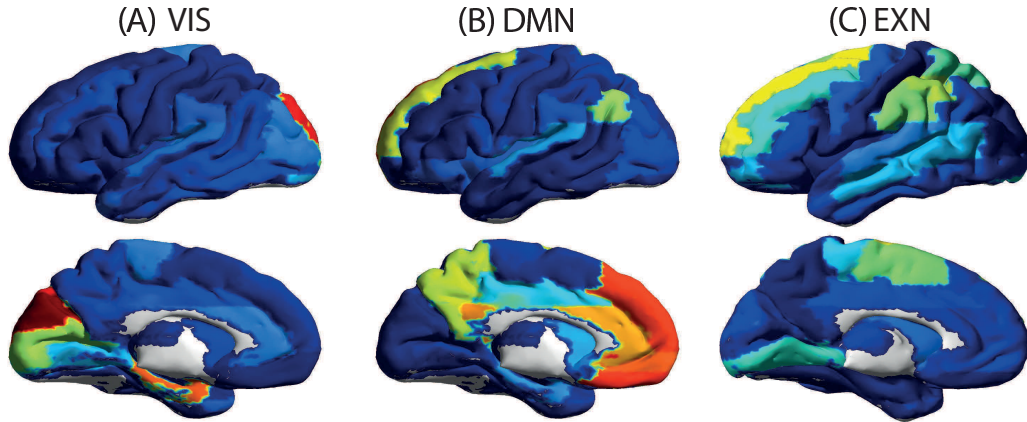


Figure 7.5 – Three resting state neuronal networks are commonly recovered using component analysis: (A) the visual network, (B) the default mode network, and (C) the executive control network.

By fitting a first order AR model ($p = 1$) to this dataset we identify latent components corresponding to these networks. Their representation appears to be less straightforward than for principal components for example, as in Figure 7.5. Indeed, latent components

consist of power spectra associated to each variable. In the previous example, with 7 nodes belonging to two clusters, the power spectrum corresponding to two variables, one in each cluster, is represented.

In the case of a real neuroimaging dataset, plotting the power spectrum for 90 variables would be unreadable. Instead in Figure 7.6 we plot only these components for $\theta = 0$, a low-frequency contribution called $\gamma_0 = \gamma(\theta = 0)$ from the definition of Section 7.3.1, and $\theta = \pi$, a high-frequency contribution called $\gamma_\pi = \gamma(\theta = \pi)$. This is motivated by the fact that for a first order AR model the latent components are characterized by these two extreme values γ_0 and γ_π because the power spectrum evolves monotonically between them.

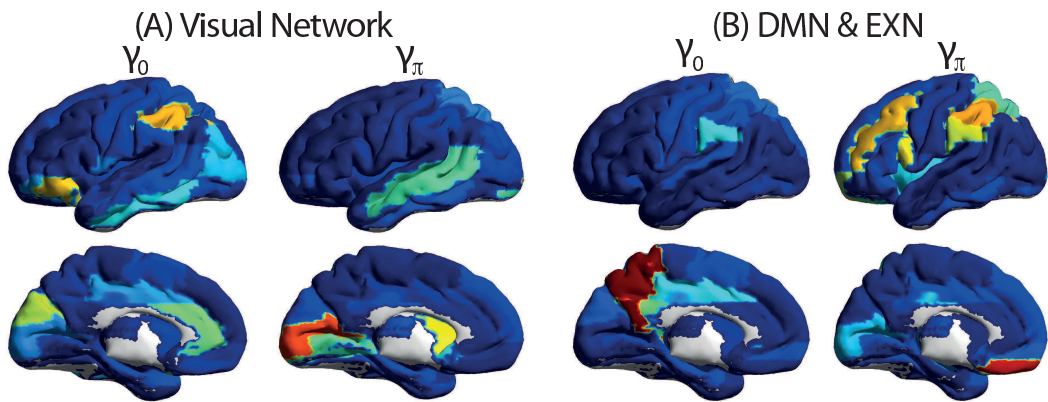


Figure 7.6 – (A) The visual network is recovered in 14 out of 17 subjects. (B) The DMN and EXN are coupled into a unique latent component in 12 out of 17 subjects.

In 14 subjects out of 17 we observe that VIS is recovered in one latent component, with no significant differences between γ_0 and γ_π . On the other hand, in 12 subjects the DMN and EXN networks are gathered in a unique latent variable, the DMN corresponding to γ_0 and EXN to γ_π .

Considering the results of Figures 7.3 and 7.4, having two classically identified static component merged into the same dynamic latent component is supposed to result from a highly similar spectral content. In the case of the DMN, measuring the degree of internal awareness, and EXN, which evaluates the level of consciousness of the environment or external awareness, this interestingly echoes some recent results. Indeed it has been shown experimentally that these two networks are highly anti-correlated (i.e. a person in resting-state has his or her degree of awareness either more internally or externally oriented, but not both) suggesting that the DMN and the EXN are both reflecting an underlying consciousness related driving process, oscillating at a specific frequency inherited by the DMN and EXN (Vanhaudenhuyse et al., 2011).

7.5 Discussion

Following what was done in component analysis in order to exploit information contained in connectivity matrices, we motivate in this Chapter the interpretation of the low-rank part of the sparse plus low-rank decomposition detailed in Chapter 6 as an extension of component analysis to dynamical models. Hence we define *latent components* from this low-rank part and the latent variables they model. As principal or independent components consist of only spatial maps, latent components possess a *spatio-temporal* structure, as illustrated in figures 7.3 & 7.4. In the case of first order dynamical models ($p = 1$) we illustrate in Figure 7.6 that each latent component can be characterised by two maps, γ_0 and γ_π as the corresponding spectrum evolves monotonically between $\theta = 0$ and $\theta = \pi$. Higher order models could be used ($p \geq 2$) but characterisation, interpretation and representation of the components will be even more difficult since the function is not monotonically increasing or decreasing between $\theta = 0$ and $\theta = \pi$.

The present contribution is part of a current trend aiming to extend component analysis techniques to dynamical models. For example, [Banko et al. \(2011\)](#); [Hyvärinen et al. \(2014\)](#) propose to apply principal component analysis on segments of the initial time series, with the limitations highlighted in Chapters 3 and 4. In comparison with these approaches, the sparse and low-rank decomposition proposed in Chapter 6 and the related latent components defined in the present Chapter provide a coherent framework in order to explore spatio-temporal structure of neuroimaging data, from a data-driven point of view. However, the amount of additional information introduced by extending component analysis to dynamical models is important and a key upcoming challenge will obviously be to better exploit, understand and characterise this information.

7.6 Conclusion

We present in this Chapter a description of the type of information encoded in the latent components identified in the low-rank part of the low-rank plus sparse decomposition presented in Chapter 6. Figure 7.3 & 7.4 suggest that this information is richer in dynamic models than in static models in the sense that dynamic latent components recover *spatio-temporal* properties of the original time series such as common spectral content. Applied to a neuroimaging dataset, this interpretation led to a novel characterization of the dynamical interplay between two neuronal networks mediating consciousness, echoing recent experimental results.

As a future research direction we intend to explore whether additional information can be recovered in higher order dynamical latent components ($p > 1$). The mathematical link between the latent components of the proposed framework and principal components

should also be developed in order to better characterise the rich information encoded in latent components.

CHAPTER 8

Conclusion

*“Man muss noch Chaos in sich haben,
um einen tanzenden Stern gebären zu können.”*

—Friedrich W. Nietzsche

This dissertation balances applicative contributions in which we assess the importance of considering the dynamical properties of functional connectivity, and methodological results consisting in the development of novel statistics and modelling approaches able to identify these properties efficiently, considering the specificities of the resting-state fMRI signal.

In this final Chapter we first summarise the main conclusions of this thesis. We then broaden the picture by identifying some promising research perspectives based on these conclusions.

8.1 Conclusions

We first define in Chapter 2 the notion of *functional connectivity* (FC), which encodes the statistical dependencies between different brain regions observed from neuroimaging data. This quantity is largely used in order to characterise brain function and we review in the sequel of the Chapter the classical *static* measures of FC. i.e. measures assuming that FC is constant over the whole neuroimaging acquisition.

Then, motivated by recent results proving that cerebral FC, as measured from fMRI time series, is actually not constant, we assess in the work presented in Chapter 3 the neuronal origin of the FC fluctuations. Originality of our results consists in the particular focus that is put on the role played by the underlying anatomical structure in these fluctuations. In particular, we show that anatomy guides the transitions between different FC patterns presenting particular modularity and efficiency properties, leading to confirmatory yet independent results about the “dynamical” nature of functional connectivity. We eventually show that these fluctuations at least partly reflect consciousness-related processes as they mainly arise from regions known for being implied in such processes.

The fluctuations of FC that we just described are captured, as in most of the studies on this topic, by evaluating the corresponding statistics in an adequate window slid over the whole fMRI time series. This approach captures fluctuations but precludes characterisation of inherent dynamical properties of FC, such as internal memory, that we believe to be important in order to characterise FC. This motivates Section 4.2 in which we clarify the distinction between *temporal* approaches of FC, that aim at characterising its fluctuations, and *dynamical* approaches of FC, that aim at capturing intrinsic dynamical markers of FC. Since dynamical models often result in simple markers and capture in our opinion essential properties of FC, the remaining of the thesis focuses on *dynamical* instead of *temporal* models and markers of FC.

The review of dynamical models of FC proposed in the sequel of Chapter 4 then allowed us to identify which family of models are more appropriate if one wants (*i*) to be able to perform whole-brain analyses leading to models with at least one hundred variables, and (*ii*) some robustness of the connectivity measure against the delays inherent to fMRI time series. These criteria led us to eliminate *directed* measures of connectivity because they rely on precedence of neuronal events that can not be assessed simply from fMRI time series as different delays can affect recordings in different regions of the brain. We also eliminated approaches explicitly modelling underlying neuronal activity through *hidden* variables related to the *observed* variables through the hemodynamic response function. Such models are too complex to estimate, precluding brain-scale analyses. These considerations motivated the new modelling approaches presented in Chapters 5, 6 and 7.

In Chapter 5 we propose a novel characterisation of FC capturing its spatial and temporal properties. We name it spatiotemporal connectivity (STC). It is based on the sequence of lagged correlation matrices directly estimated from fMRI time series. Even if it is an elementary estimation of connectivity properties, we show based on the analysis of two fMRI datasets that this measure is robust against the inherent delays of fMRI time series and reveals important features of FC that are not captured by classical connectivity measures. In particular, the internal memory of FC in selected networks estimated from STC seems to be highly sensitive to the state of consciousness of the patients. We eventually show based

on STC measurements that information encoded in the *inverse power spectral densities* -reflecting conditional dependencies- and in the power spectral density provide closely related spatial and temporal characterisation of FC. Our results suggest that the former is slightly more sensitive in order to capture differences in the experimental paradigms.

Then, considering the basic motivation of component analysis that aim at capturing a common *spatial* subspace of variation from the classic static correlation matrix, we follow a similar path starting from the dynamical extension of the correlation matrix described in Chapter 5. To this end we propose in Chapter 6 an algorithm identifying the optimal *sparse plus low-rank* decomposition of the inverse power spectral density, or graphical model, estimated from the fMRI time series. We exploit the decoupling between the sparse and the low-rank constraints of the corresponding optimization problem by using the alternating direction method of multipliers which results in solving decoupled simpler optimization problems. The final formulation allows to deal with datasets of dimensions usually encountered in neuroimaging applications, up to a thousand variables.

Similarly to components identified using component analysis techniques that are more complex to interpret compared to pairwise correlations encoded in the correlation matrix, the sparse plus low-rank decomposition that we propose is more difficult to interpret compared to the estimated inverse power spectral density that basically encoded direct interactions between the variables. Chapter 7 develops this question, and in particular we argue that the low-rank part of the decomposition is a dynamical extension of the classical principal component analysis approach. Indeed this part, modelling the presence of *latent variables*, or *latent components* spreading some common behaviour in all the observed variables, captures a *spatiotemporal* subspace of variation of the observed variables, blending the classical interpretation of a component as a *neuronal network* with a spectral characterisation of this network.

8.2 Perspectives

The contributions summarised here above could obviously call for developments. We highlight as a conclusion of this thesis the ones that seem the most promising.

From an application point of view, we detail in Chapter 3 the reasons why the fluctuations of functional connectivity, projected on the underlying anatomy, might reflect consciousness related processes. This is based on spatial and temporal properties of the fluctuations but should be assessed on datasets coming from patients effectively undergoing different states of consciousness. We could not apply our approach to the dataset of patients undergoing four different states of consciousness used in Chapters 5 and 7 because

the structural data, which is needed in this analysis together with functional data, was not available. With such additional information, one could explore more precise questions such as: *Is consciousness more defined by structural or functional connectivity?*, or *Could functional connectivity be decoupled in a structural contribution corresponding to basic physiological needs and a higher-order contribution corresponding to consciousness?*

It appears from the conclusions presented in this Chapter that we favour generic models, designed to be robust against inherent flaws of the fMRI signal, compared to models tailored for fMRI time series analyses and explicitly including more a priori information about the nature of this signal. A representative example of the latter has become quite popular recently: the single co-activation pattern framework briefly described in Chapter 4. In this approach only the highest values of the fMRI time series are considered in the computation of connectivity measures because they are assumed to reflect underlying neuronal activation events, the only one worth considering. This hypothesis obviously leads to different modelling approaches compared to the mere (joint-)gaussianity of the time series assumed in our proposed frameworks. Indeed, we considered that explicitly modelling specific features of fMRI time series, and the uncertainty about this information, was too expensive compared to the potential resulting benefits both from a computational and an interpretability point of view. However, once some assumptions have been strongly assessed about the nature of the fMRI signal, it could be worth blending our frameworks with these specific properties.

Finally, the sparse plus low-rank decomposition of the inverse power spectral density detailed in the last Chapters is presented as a dynamical extension of principal component analysis (PCA). This should be further assessed from a theoretical point of view, clarifying differences and similarities with classic component analysis techniques, as the low-rank part of the decomposition is not exactly equivalent to PCA, even if the underlying motivation is the same. For example, PCA is based on the correlation matrix whereas our proposed decomposition is based on the *inverse* power spectral density that encodes *conditional* dependencies. From a practical point of view we showed in Chapter 5 that the information contained in the power spectral density and its inverse are very close. Still, some additional characterisation of the *latent components* defined in Chapter 7, and more specifically their spectral features, would lead to a better interpretability of these components, hereby strongly grounding the definition of dynamical component analysis.

Bibliography

- Allen, E.A., Damaraju, E., Plis, S.M., Erhardt, E.B., Eichele, T., Calhoun, V.D., 2012. Tracking whole-brain connectivity dynamics in the resting state. *Cereb Cortex* .
- Amico, E., Gomez, F., Di Perri, C., Vanhaudenhuyse, A., Lesenfants, D., Boveroux, P., Bonhomme, V., Brichant, J.F., Marinazzo, D., Laureys, S., 2014. Posterior cingulate cortex-related co-activation patterns: a resting state fMRI study in propofol-induced loss of consciousness. *PLoS One* 9, e100012.
- Andersen, A.H., Gash, D.M., Avison, M.J., 1999. Principal component analysis of the dynamic response measured by fmri: a generalized linear systems framework. *Magn Reson Imaging* 17, 795–815.
- Anemüller, J., Duann, J.R., Sejnowski, T.J., Makeig, S., 2006. Spatio-temporal dynamics in fmri recordings revealed with complex independent component analysis. *Neurocomputing* 69, 1502–1512.
- Banerjee, O., El Ghaoui, L., d'Aspremont, A., 2008. Model selection through sparse maximum likelihood estimation for multivariate gaussian or binary data. *Journal of Machine Learning Research* 9.
- Banko, Z., Dobos, L., Abonyi, J., 2011. Dynamic principal component analysis in multivariate time-series segmentation. *Conservation, Information, Evolution* 1, 11–24.
- Barnett, L., 2009. Granger causality and transfer entropy are equivalent for gaussian variables. *Physical Review Letters* 103, 238701.
- Bassett, D.S., Porter, M.A., Wymbs, N.F., Grafton, S.T., Carlson, J.M., Mucha, P.J., 2013. Robust detection of dynamic community structure in networks. *Chaos* 23, 013142.
- Bassett, D.S., Wymbs, N.F., Porter, M.A., Mucha, P.J., Carlson, J.M., Grafton, S.T., 2011. Dynamic reconfiguration of human brain networks during learning. *Proc Natl Acad Sci U S A* 108, 7641–6.
- Bastian, M., Sackur, J., 2013. Mind wandering at the fingertips: automatic parsing of subjective states based on response time variability. *Front Psychol* 4, 573.
- Baum, L., Petri, T., 1966. Statistical inference for probabilistic functions of finite state markov chains. *The Annals of Mathematical Statistics* 37, 1554–63.

- Beckmann, C.F., DeLuca, M., Devlin, J.T., Smith, S.M., 2005. Investigations into resting-state connectivity using independent component analysis. *Philos Trans R Soc Lond B Biol Sci* 360, 1001–13.
- Berg, E., Schmidt, M., Friedlander, M., Murphy, K., 2008. Group sparsity via linear-time projection. Technical Report. Dept. of Computer Science, Univ. of British Columbia.
- Bhattacharya, S., Ringo Ho, M.H., Purkayastha, S., 2006. A bayesian approach to modeling dynamic effective connectivity with fmri data. *Neuroimage* 30, 794–812.
- Biswal, B.B., Van Kylen, J., Hyde, J.S., 1997. Simultaneous assessment of flow and bold signals in resting-state functional connectivity maps. *NMR Biomed* 10, 165–70.
- Boveroux, P., Vanhaudenhuyse, A., Bruno, M.A., Noirhomme, Q., Lauwick, S., Luxen, A., Degueldre, C., Plenevaux, A., Schnakers, C., Phillips, C., Brichant, J.F., Bonhomme, V., Maquet, P., Greicius, M.D., Laureys, S., Boly, M., 2010. Breakdown of within- and between-network resting state functional magnetic resonance imaging connectivity during propofol-induced loss of consciousness. *Anesthesiology* 113, 1038–53.
- Box, G.E.P., Jenkins, G.M., 1976. Time series analysis: forecasting and control. Holden-Day series in time series analysis and digital processing. rev. ed ed., Holden-Day, San Francisco.
- Boyd, S., Parikh, N., Chu, E., Peleato, B., Eckstein, J., 2011. Distributed optimization and statistical learning via the alternating direction method of multipliers. *Foundations and Trends in Machine Learning* 3.
- Boynton, G.M., Engel, S.A., Glover, G.H., Heeger, D.J., 1996. Linear systems analysis of functional magnetic resonance imaging in human v1. *J Neurosci* 16, 4207–21.
- Breakspear, M., Jirsa, V., Deco, G., 2010. Computational models of the brain: from structure to function. *Neuroimage* 52, 727–30.
- Bressler, S.L., Seth, A.K., 2011. Wiener-granger causality: a well established methodology. *Neuroimage* 58, 323–9.
- Brillinger, D., 2001. *Time Series: Data Analysis and Theory* (Classics in Applied Mathematics, 36). SIAM: Society for Industrial and Applied Mathematics.
- Brookes, M.J., Woolrich, M., Luckhoo, H., Price, D., Hale, J.R., Stephenson, M.C., Barnes, G.R., Smith, S.M., Morris, P.G., 2011. Investigating the electrophysiological basis of resting state networks using magnetoencephalography. *Proc Natl Acad Sci U S A* 108, 16783–8.
- Buckner, R.L., Carroll, D.C., 2007. Self-projection and the brain. *Trends Cogn Sci* 11, 49–57.
- Bullmore, E., Sporns, O., 2009a. Complex brain networks: graph theoretical analysis of structural and functional systems. *Nature Rev Neurosci* 10, 186–98.
- Bullmore, E., Sporns, O., 2009b. Complex brain networks: graph theoretical analysis of structural and functional systems. *Nature Reviews Neuroscience* 10, 186–98.
- Bullmore, E.T., Bassett, D.S., 2011. Brain graphs: graphical models of the human brain connectome. *Annu Rev Clin Psychol* 7, 113–40.

- Bünger, F., 2014. Inverses, determinants, eigenvalues, and eigenvectors of real symmetric toeplitz matrices with linearly increasing entries. Submitted to Linear Algebra and its applications .
- Buxton, R.B., Uludağ, K., Dubowitz, D.J., Liu, T.T., 2004. Modeling the hemodynamic response to brain activation. Neuroimage 23 Suppl 1, S220–33.
- Byrnes, C., Gusev, S., Lindquist, A., 1998. A convex optimization approach to the rational covariance extension problem. SIAM J. Optimiz. 37, 211–29.
- Cabral, J., Hugues, E., Sporns, O., Deco, G., 2011. Role of local network oscillations in resting-state functional connectivity. Neuroimage 57, 130–9.
- Calhoun, V.D., Adali, T., Pearlson, G.D., Pekar, J.J., 2001. Spatial and temporal independent component analysis of functional mri data containing a pair of task-related waveforms. Hum Brain Mapp 13, 43–53.
- Cammoun, L., Gigandet, X., Meskaldji, D., Thiran, J.P., Sporns, O., Do, K.Q., Maeder, P., Meuli, R., Hagmann, P., 2012. Mapping the human connectome at multiple scales with diffusion spectrum mri. J Neurosci Methods 203, 386–97.
- Chai, B., Walther, D., Beck, D., Fei-fei, L., 2009. Exploring functional connectivities of the human brain using multivariate information analysis. Advances in Neural Information Processing Systems 22 , 270–278.
- Chandrasekaran, V., Parrilo, P.A., Willsky, A.S., 2010. Latent variable graphical model selection via convex optimization. ArXiv e-prints , [arXiv:1008.1290](https://arxiv.org/abs/1008.1290).
- Chang, C., Glover, G.H., 2010. Time-frequency dynamics of resting-state brain connectivity measured with fmri. Neuroimage 50, 81–98.
- Christoff, K., Gordon, A.M., Smallwood, J., Smith, R., Schooler, J.W., 2009. Experience sampling during fMRI reveals default network and executive system contributions to mind wandering. Proc Natl Acad Sci U S A 106, 8719–24.
- Clare, L., Whitaker, C.J., Nelis, S.M., 2010. Appraisal of memory functioning and memory performance in healthy ageing and early-stage alzheimer's disease. Neuropsychol Dev Cogn B Aging Neuropsychol Cogn 17, 462–91.
- Clare, L., Wilson, B., Carter, G., Roth, I., Hodges, J., 2002. Assessing awareness in early-stage Alzheimer's disease: development and piloting of the Memory Awareness Rating Scale. Neuropsychol Rehabil. 12, 341–62.
- Comon, P., 1994. Independent component analysis, a new concept? Signal Processing 36, 287–314.
- Cover, T., Thomas, J., 1991. Information Theory. New York: Wiley.
- Dahlhaus, R., 2000. Graphical interaction models for multivariate time series1. Metrika 51, 157–172.
- Dale, A.M., Buckner, R.L., 1997. Selective averaging of rapidly presented individual trials using fmri. Hum Brain Mapp 5, 329–40.

- Damoiseaux, J.S., Greicius, M.D., 2009. Greater than the sum of its parts: a review of studies combining structural connectivity and resting-state functional connectivity. *Brain Struct Funct* 213, 525–33.
- Damoiseaux, J.S., Rombouts, S.A.R.B., Barkhof, F., Scheltens, P., Stam, C.J., Smith, S.M., Beckmann, C.F., 2006. Consistent resting-state networks across healthy subjects. *Proc Natl Acad Sci U S A* 103, 13848–53.
- Daubechies, I., Roussos, E., Takerkart, S., Benharrosh, M., Golden, C., D’Ardenne, K., Richter, W., Cohen, J.D., Haxby, J., 2009. Independent component analysis for brain fmri does not select for independence. *Proc Natl Acad Sci U S A* 106, 10415–22.
- D’avanzo, C., Tarantino, V., Bisiacchi, P., Sparacino, G., 2009. A wavelet methodology for eeg time-frequency analysis in a time discrimination task. *International Journal of Bioelectromagnetism* 11, 185–88.
- David, O., Cosmelli, D., Friston, K.J., 2004. Evaluation of different measures of functional connectivity using a neural mass model. *Neuroimage* 21, 659–73.
- David, O., Guillemain, I., Sallet, S., Reyt, S., Deransart, C., Segebarth, C., Depaulis, A., 2008. Identifying neural drivers with functional mri: an electrophysiological validation. *PLoS Biol* 6, 2683–97.
- Deco, G., Hagmann, P., Hudetz, A.G., Tononi, G., 2013a. Modeling resting-state functional networks when the cortex falls sleep: Local and global changes. *Cereb Cortex* .
- Deco, G., Ponce-Alvarez, A., Mantini, D., Romani, G.L., Hagmann, P., Corbetta, M., 2013b. Resting-state functional connectivity emerges from structurally and dynamically shaped slow linear fluctuations. *J Neurosci* 33, 11239–52.
- Deco, G., Senden, M., Jirsa, V., 2012. How anatomy shapes dynamics: a semi-analytical study of the brain at rest by a simple spin model. *Front Comput Neurosci* 6, 68.
- Dempster, A., 1972. Covariance selection. *Biometrics* 28, 157–75.
- Desikan, R.S., Ségonne, F., Fischl, B., Quinn, B.T., Dickerson, B.C., Blacker, D., Buckner, R.L., Dale, A.M., Maguire, R.P., Hyman, B.T., Albert, M.S., Killiany, R.J., 2006. An automated labeling system for subdividing the human cerebral cortex on MRI scans into gyral based regions of interest. *Neuroimage* 31, 968–80.
- Doucet, G., Naveau, M., Petit, L., Zago, L., Crivello, F., Jobard, G., Delcroix, N., Mellet, E., Tzourio-Mazoyer, N., Mazoyer, B., Joliot, M., 2012. Patterns of hemodynamic low-frequency oscillations in the brain are modulated by the nature of free thought during rest. *Neuroimage* 59, 3194–200.
- Duan, R., Man, H., 2012. Activation detection on fmri time series using hidden markov model. *Advances in Artificial Neural Systems* 4.
- Eaton, M., 1983. Multivariate Statistics: a Vector Space Approach. John Wiley and Sons.
- Edgington, E., Onghena, P., 1969. Randomization Tests. CRC Press.

- Engel, Jr, J., Thompson, P.M., Stern, J.M., Staba, R.J., Bragin, A., Mody, I., 2013. Connectomics and epilepsy. *Curr Opin Neurol* 26, 186–94.
- Eryilmaz, H., Van De Ville, D., Schwartz, S., Vuilleumier, P., 2011. Impact of transient emotions on functional connectivity during subsequent resting state: a wavelet correlation approach. *Neuroimage* 54, 2481–91.
- Fox, K.C.R., Nijeboer, S., Solomonova, E., Domhoff, G.W., Christoff, K., 2013. Dreaming as mind wandering: evidence from functional neuroimaging and first-person content reports. *Front Hum Neurosci* 7, 412.
- Fox, M.D., Snyder, A.Z., Vincent, J.L., Corbetta, M., Van Essen, D.C., Raichle, M.E., 2005. The human brain is intrinsically organized into dynamic, anticorrelated functional networks. *Proc Natl Acad Sci U S A* 102, 9673–8.
- Fox, M.D., Snyder, A.Z., Vincent, J.L., Raichle, M.E., 2007. Intrinsic fluctuations within cortical systems account for intertrial variability in human behavior. *Neuron* 56, 171–84.
- Friston, K.J., 2011. Functional and effective connectivity: a review. *Brain Connectivity* 1, 13–36.
- Friston, K.J., Harrison, L., Penny, W., 2003. Dynamic causal modelling. *Neuroimage* 19, 1273–302.
- Friston, K.J., Kahan, J., Biswal, B., Razi, A., 2014. A dcm for resting state fmri. *Neuroimage* 94, 396–407.
- Gao, W., Zhu, H., Giovanello, K., Lin, W., 2010. Multivariate network-level approach to detect interactions between large-scale functional systems. *Med Image Comput Comput Assist Interv* 13, 298–305.
- Garraux, G., 2014. Introduction à la neurophysiologie - NEUR0431-1. Notes de cours.
- Goldberg, I.I., Harel, M., Malach, R., 2006. When the brain loses its self: prefrontal inactivation during sensorimotor processing. *Neuron* 50, 329–39.
- Gollo, L.L., Breakspear, M., 2014. The frustrated brain: from dynamics on motifs to communities and networks. *Philos Trans R Soc Lond B Biol Sci* 369.
- Gollo, L.L., Zalesky, A., Hutchison, R.M., van den Heuvel, M., Breakspear, M., 2015. Dwelling quietly in the rich club: brain network determinants of slow cortical fluctuations. *Philos Trans R Soc Lond B Biol Sci* 370.
- Gonzalez-Castillo, J., Handwerker, D.A., Robinson, M.E., Hoy, C.W., Buchanan, L.C., Saad, Z.S., Bandettini, P.A., 2014. The spatial structure of resting state connectivity stability on the scale of minutes. *Front Neurosci* 8, 138.
- Gorgolewski, K., Burns, C.D., Madison, C., Clark, D., Halchenko, Y.O., Waskom, M.L., Ghosh, S.S., 2011. Nipype: a flexible, lightweight and extensible neuroimaging data processing framework in python. *Front Neuroinform* 5, 13.
- Granger, C., 1969. Investigating causal relations by econometric models and cross-spectral methods. *Econometrica* 37, 424–38.

- Grant, M., Boyd, S., Yu, Y., 2005. Cvx: Matlab software for disciplined convex programming. Available from www.stanford.edu/~boyd/cvx/.
- Gray, R., 2005. Toeplitz and circulant matrices: a review. *Foundations and trends in Communication and Information Theory* 2.
- Greicius, M.D., Krasnow, B., Reiss, A.L., Menon, V., 2003. Functional connectivity in the resting brain: a network analysis of the default mode hypothesis. *Proc Natl Acad Sci U S A* 100, 253–8.
- Griffa, A., Baumann, P.S., Thiran, J.P., Hagmann, P., 2013. Structural connectomics in brain diseases. *Neuroimage* 80, 515–26.
- Gusnard, D.A., Raichle, M.E., Raichle, M.E., 2001. Searching for a baseline: functional imaging and the resting human brain. *Nat Rev Neurosci* 2, 685–94.
- Hagmann, P., Cammoun, L., Gigandet, X., Meuli, R., Honey, C.J., Wedeen, V.J., Sporns, O., 2008. Mapping the structural core of human cerebral cortex. *PLoS Biol* 6, e159.
- Hahn, B., Ross, T.J., Stein, E.A., 2007. Cingulate activation increases dynamically with response speed under stimulus unpredictability. *Cereb Cortex* 17, 1664–71.
- Handwerker, D.A., Roopchansingh, V., Gonzalez-Castillo, J., Bandettini, P.A., 2012. Periodic changes in fMRI connectivity. *Neuroimage* 63, 1712–9.
- Harrison, L., Penny, W.D., Friston, K., 2003. Multivariate autoregressive modeling of fmri time series. *Neuroimage* 19, 1477–91.
- Hasenkamp, W., Wilson-Mendenhall, C.D., Duncan, E., Barsalou, L.W., 2012. Mind wandering and attention during focused meditation: a fine-grained temporal analysis of fluctuating cognitive states. *Neuroimage* 59, 750–60.
- He, R., Hu, B., Zheng, W., Kong, X., 2011. Robust principal component analysis based on maximum correntropy criterion. *IEEE Transactions on Image Processing* 20, 1485–94.
- Heine, L., Soddu, A., Gómez, F., Vanhaudenhuyse, A., Tshibanda, L., Thonnard, M., Charland-Verville, V., Kirsch, M., Laureys, S., Demertzi, A., 2012. Resting state networks and consciousness: alterations of multiple resting state network connectivity in physiological, pharmacological, and pathological consciousness states. *Front Psychol* 3, 295.
- van den Heuvel, M.P., Mandl, R.C.W., Kahn, R.S., Hulshoff Pol, H.E., 2009. Functionally linked resting-state networks reflect the underlying structural connectivity architecture of the human brain. *Hum Brain Mapp* 30, 3127–41.
- Honey, C.J., Sporns, O., Cammoun, L., Gigandet, X., Thiran, J.P., Meuli, R., Hagmann, P., 2009. Predicting human resting-state functional connectivity from structural connectivity. *Proc Natl Acad Sci U S A* 106, 2035–40.
- Honey, C.J., Thivierge, J.P., Sporns, O., 2010. Can structure predict function in the human brain? *NeuroImage* 52, 766–76.
- Hopfield, J.J., 1982. Neural networks and physical systems with emergent collective computational abilities. *Proceedings of the National Academy of Sciences* 79, 2554–2558.

- Horn, R.A., Johnson, C.R., 1990. Matrix analysis. Cambridge University Press .
- Hsieh, C.J., Dhillon, I., Ravikumar, P., Becker, S., Olsen, P., 2014a. QUIC & DIRTY: A Quadratic Approximation Approach for Dirty Statistical Models. In Advances in Neural Information Processing Systems (NIPS) 27.
- Hsieh, C.J., Sustik, M., Dhillon, I., Ravikumar, P., 2014b. QUIC: Quadratic Approximation for Sparse Inverse Covariance Estimation. *Journal of Machine Learning Research* 15.
- Hutchison, R.M., Womelsdorf, T., Allen, E.A., Bandettini, P.A., Calhoun, V.D., Corbetta, M., Della Penna, S., Duyn, J.H., Glover, G.H., Gonzalez-Castillo, J., Handwerker, D.A., Keilholz, S., Kiviniemi, V., Leopold, D.A., de Pasquale, F., Sporns, O., Walter, M., Chang, C., 2013. Dynamic functional connectivity: Promise, issues, and interpretations. *Neuroimage* 80, 360–78.
- Hutchison, R.M., Womelsdorf, T., Gati, J.S., Everling, S., Menon, R.S., 2012. Resting-state networks show dynamic functional connectivity in awake humans and anesthetized macaques. *Hum Brain Mapp* .
- Hyvärinen, A., 1999. Fast and robust fixed-point algorithms for independent component analysis. *IEEE Transactions on Neural Networks* 10, 626–34.
- Hyvärinen, A., Hirayama, J., Kawanabe, M., 2014. Dynamic connectivity factorization: Interpretable decompositions of non-stationarity, in: International Workshop on Pattern Recognition in Neuroimaging, PRNI 2014, Tübingen, Germany, June 4–6, 2014, pp. 1–4.
- Hyvärinen, A., Karhunen, J., Oja, E., 2001. Independent Component Analysis. John Wiley and Son.
- Jahanshad, N., Rajagopalan, P., Hua, X., Hibar, D.P., Nir, T.M., Toga, A.W., Jack, Jr, C.R., Saykin, A.J., Green, R.C., Weiner, M.W., Medland, S.E., Montgomery, G.W., Hansell, N.K., McMahon, K.L., de Zubicaray, G.I., Martin, N.G., Wright, M.J., Thompson, P.M., Alzheimer's Disease Neuroimaging Initiative, 2013. Genome-wide scan of healthy human connectome discovers spon1 gene variant influencing dementia severity. *Proc Natl Acad Sci U S A* 110, 4768–73.
- Jolliffe, I.T., 2002. Principal Component Analysis and Factor Analysis. Springer Series in Statistics, Springer New York, New York.
- Kaiser, M., 2013. The potential of the human connectome as a biomarker of brain disease. *Front Hum Neurosci* 7, 484.
- Kiviniemi, V., Vire, T., Remes, J., Elseoud, A.A., Starck, T., Tervonen, O., Nikkinen, J., 2011. A sliding time-window ICA reveals spatial variability of the default mode network in time. *Brain Connect* 1, 339–47.
- Koch, M.A., Norris, D.G., Hund-Georgiadis, M., 2002. An investigation of functional and anatomical connectivity using magnetic resonance imaging. *Neuroimage* 16, 241–50.
- Koller, D., Friedman, N., 2009. Probabilistic Graphical Models. Massachusetts: MIT Press.
- Kötter, R., Sommer, F.T., 2000. Global relationship between anatomical connectivity and activity propagation in the cerebral cortex. *Philos Trans R Soc Lond B Biol Sci* 355, 127–34.

- Kucyi, A., Davis, K.D., 2014. Dynamic functional connectivity of the default mode network tracks daydreaming. *Neuroimage* 100, 471–480.
- de Kwaasteniet, B., Ruhe, E., Caan, M., Rive, M., Olabarriaga, S., Groefsema, M., Heesink, L., van Wingen, G., Denys, D., 2013. Relation between structural and functional connectivity in major depressive disorder. *Biol Psychiatry* 74, 40–7.
- Lamme, V.A., 2003. Why visual attention and awareness are different. *Trends Cogn Sci* 7, 12–18.
- Laplace, P.S., 1809. Mémoire sur les approximations des formules qui sont fonctions de très-grands nombres, et sur leur application aux probabilités. *Mémoires de la Classe des sciences mathématiques et physiques de l’Institut de France* , 353–415.
- Lenz, M., Musso, M., Linke, Y., Tüscher, O., Timmer, J., Weiller, C., Schelter, B., 2011. Joint eeg/fmri state space model for the detection of directed interactions in human brains—a simulation study. *Physiol Meas* 32, 1725–36.
- Leonardi, N., Richiardi, J., Gschwind, M., Simioni, S., Annoni, J.M., Schluep, M., Vuilleumier, P., Van De Ville, D., 2013. Principal components of functional connectivity: A new approach to study dynamic brain connectivity during rest. *Neuroimage* 83.
- Leonardi, N., Van De Ville, D., 2015. On spurious and real fluctuations of dynamic functional connectivity during rest. *Neuroimage* 104, 430–6.
- Li, W., 1990. Mutual information functions versus correlation functions. *Journal of Statistical Physics* 60, 823–37.
- Lieberman, M.D., 2007. Social cognitive neuroscience: a review of core processes. *Annu Rev Psychol* 58, 259–89.
- Liégeois, R., 2011. Structured sparse PCA for fMRI Imaging. Master’s thesis. University of Liège.
- Liégeois, R., Ziegler, E., Phillips, C., Geurts, P., Gomez, F., Bahri, M.A., Yeo, B.T.T., Soddu, A., Vanhaudenhuyse, A., Laureys, S., Sepulchre, R., 2015. Cerebral functional connectivity periodically (de)synchronizes with anatomical constraints. *Brain Structure and Function*, in Press .
- Lindquist, M.A., Xu, Y., Nebel, M.B., Caffo, B.S., 2014. Evaluating dynamic bivariate correlations in resting-state fmri: a comparison study and a new approach. *Neuroimage* 101, 531–46.
- Liu, X., Duyn, J.H., 2013. Time-varying functional network information extracted from brief instances of spontaneous brain activity. *Proc Natl Acad Sci U S A* 110, 4392–7.
- Lizier, J.T., Heinze, J., Horstmann, A., Haynes, J.D., Prokopenko, M., 2011. Multivariate information-theoretic measures reveal directed information structure and task relevant changes in fmri connectivity. *J Comput Neurosci* 30, 85–107.
- Lohmann, G., Erfurth, K., Müller, K., Turner, R., 2012. Critical comments on dynamic causal modelling. *Neuroimage* 59, 2322–9.
- Lv, P., Guo, L., Hu, X., Li, X., Jin, C., Han, J., Li, L., Liu, T., 2013. Modeling dynamic functional information flows on large-scale brain networks. *Med Image Comput Comput Assist Interv* 16, 698–705.

- Macey, P.M., Macey, K.E., Kumar, R., Harper, R.M., 2004. A method for removal of global effects from fmri time series. *NeuroImage* 22, 360–6.
- MacKay, D., 2006. Gaussian process basics. http://videolectures.net/gpip06_mackay_gpb/.
- Marrelec, G., Krainik, A., Duffau, H., Pélégrini-Issac, M., Lehéricy, S., Doyon, J., Benali, H., 2006. Partial correlation for functional brain interactivity investigation in functional mri. *Neuroimage* 32, 228–37.
- Martinsson, P., Rokhlin, V., Michael, T., 2005. A fast algorithm for the inversion of general toeplitz matrices. *Computers and Mathematics with Applications* 50, 741–52.
- Maxim, V., Sendur, L., Fadili, J., Suckling, J., Gould, R., Howard, R., Bullmore, E., 2005. Fractional gaussian noise, functional mri and alzheimer's disease. *Neuroimage* 25, 141–58.
- McIntosh, A.R., Gonzalez-Lima, F., 1994. Structural equation modeling and its application to network analysis in functional brain imaging. *Human Brain Mapping* 2, 2–22+.
- McKeown, M.J., Makeig, S., Brown, G.G., Jung, T.P., Kindermann, S.S., Bell, A.J., Sejnowski, T.J., 1998. Analysis of fmri data by blind separation into independent spatial components. *Hum Brain Mapp* 6, 160–88.
- McKhann, G.M., Knopman, D.S., Chertkow, H., Hyman, B.T., Jack, Jr, C.R., Kawas, C.H., Klunk, W.E., Koroshetz, W.J., Manly, J.J., Mayeux, R., Mohs, R.C., Morris, J.C., Rossor, M.N., Scheltens, P., Carrillo, M.C., Thies, B., Weintraub, S., Phelps, C.H., 2011. The diagnosis of dementia due to alzheimer's disease: recommendations from the national institute on aging-alzheimer's association workgroups on diagnostic guidelines for alzheimer's disease. *Alzheimers Dement* 7, 263–9.
- Messé, A., Rudrauf, D., Benali, H., Marrelec, G., 2014. Relating structure and function in the human brain: relative contributions of anatomy, stationary dynamics, and non-stationarities. *PLoS Comput Biol* 10, e1003530.
- Meunier, D., Lambiotte, R., Bullmore, E.T., 2010. Modular and hierarchically modular organization of brain networks. *Frontiers in Neuroscience* 4.
- Moran, R., Pinotsis, D.A., Friston, K., 2013. Neural masses and fields in dynamic causal modeling. *Front Comput Neurosci* 7, 57.
- Moussa, M.N., Steen, M.R., Laurienti, P.J., Hayasaka, S., 2012. Consistency of network modules in resting-state fmri connectome data. *PLoS One* 7, e44428.
- Murphy, K., Birn, R.M., Handwerker, D.A., Jones, T.B., Bandettini, P.A., 2009. The impact of global signal regression on resting state correlations: are anti-correlated networks introduced? *NeuroImage* 44, 893–905.
- Newman, M.E.J., Girvan, M., 2004. Finding and evaluating community structure in networks. *Physical Review E* 69, 026113+.
- Onnela, J.P., Saramäki, J., Kertesz, J., Kaski, K., 2005. Intensity and coherence of motifs in weighted complex networks. *Physical Review E* 71.

- Ouyang, Y., Chen, Y., Lan, G., Pasiliao, E., 2014. An accelerated linearised alternating direction method of multipliers. Submitted <http://arxiv.org/pdf/1401.6607v3.pdf>.
- Paiva, a., Xu, J., John, P., 2006. Kernel principal components are maximum entropy projections. Proceedings of the International Conference on Independent Component Analysis and Blind Source Separation.
- Park, H.J., Friston, K., 2013. Structural and functional brain networks: from connections to cognition. *Science* 342, 1238411.
- Passingham, R.E., Stephan, K.E., Kotter, R., 2002. The anatomical basis of functional localization in the cortex. *Nat Rev Neurosci* 3, 606–16.
- Rajapakse, J.C., Kruggel, F., Maisog, J.M., von Cramon, D.Y., 1998. Modeling hemodynamic response for analysis of functional mri time-series. *Hum Brain Mapp* 6, 283–300.
- Ramkumar, P., Parkkonen, L., Hyvärinen, A., 2014. Group-level spatial independent component analysis of fourier envelopes of resting-state meg data. *Neuroimage* 86, 480–91.
- Reichel, L., Trefethen, L., 1992. Eigenvalues and pseudo-eigenvalues of toeplitz matrices. *Linear Algebra and its applications*, 153–85.
- Richiardi, J., Eryilmaz, H., Schwartz, S., Vuilleumier, P., Van De Ville, D., 2011. Decoding brain states from fMRI connectivity graphs. *Neuroimage* 56, 616–26.
- Ringh, A., Karlsson, J., 2015. A fast solver for the circulant rational covariance extension problem. European Control Conference .
- Rogers, B.P., Katwal, S.B., Morgan, V.L., Asplund, C.L., Gore, J.C., 2010. Functional mri and multivariate autoregressive models. *Magn Reson Imaging* 28, 1058–65.
- Rubinov, M., Sporns, O., 2010. Complex network measures of brain connectivity: uses and interpretations. *Neuroimage* 52, 1059–69.
- Ryali, S., Chen, T., Supekar, K., Menon, V., 2012. Estimation of functional connectivity in fmri data using stability selection-based sparse partial correlation with elastic net penalty. *Neuroimage* 59, 3852–61.
- Sakoḡlu, U., Pearson, G.D., Kiehl, K.A., Wang, Y.M., Michael, A.M., Calhoun, V.D., 2010. A method for evaluating dynamic functional network connectivity and task-modulation: application to schizophrenia. *MAGMA* 23, 351–66.
- van Schouwenburg, M.R., Zwiers, M.P., van der Schaaf, M.E., Geurts, D.E.M., Schellekens, A.F.A., Buitelaar, J.K., Verkes, R.J., Cools, R., 2013. Anatomical connection strength predicts dopaminergic drug effects on fronto-striatal function. *Psychopharmacology (Berl)* 227, 521–31.
- Schreiber, T., 2000. Measuring information transfer. *Phys Rev Lett* 85, 461–64.
- Shen, K., Hutchison, R.M., Bezgin, G., Everling, S., McIntosh, A.R., 2015. Network structure shapes spontaneous functional connectivity dynamics. *J Neurosci* 35, 5579–88.

- Shirer, W.R., Ryali, S., Rykhlevskaia, E., Menon, V., Greicius, M.D., 2012. Decoding subject-driven cognitive states with whole-brain connectivity patterns. *Cereb Cortex* 22, 158–65.
- Sidlauskaitė, J., Wiersema, J.R., Roeyers, H., Krebs, R.M., Vassena, E., Fias, W., Brass, M., Achten, E., Sonuga-Barke, E., 2014. Anticipatory processes in brain state switching - evidence from a novel cued-switching task implicating default mode and salience networks. *Neuroimage* 98C, 359–365.
- Smith, S.M., Jenkinson, M., Woolrich, M.W., Beckmann, C.F., Behrens, T.E.J., Johansen-Berg, H., Bannister, P.R., De Luca, M., Drobniak, I., Flitney, D.E., Niazy, R.K., Saunders, J., Vickers, J., Zhang, Y., De Stefano, N., Brady, J.M., Matthews, P.M., 2004. Advances in functional and structural MR image analysis and implementation as FSL. *Neuroimage* 23 Suppl 1, S208–19.
- Smith, S.W., 1997. The scientist and engineer's guide to digital signal processing. First ed., California Technical Pub.
- Songsiri, J., Vandenberghe, L., 2010. Topology selection in graphical models of autoregressive processes. *J. Mach. Learn. Res.* 11, 2671–2705.
- Sporns, O., 2002. Graph theory methods for the analysis of neural connectivity patterns. *Neuroscience Databases. A Practical Guide* (Kötter, R. ed.) , 171–186.
- Sporns, O., Chialvo, D., Kaiser, M., Hilgetag, C., 2004. Organization, development and function of complex brain networks. *Trends in Cognitive Sciences* 8, 418–425.
- Sporns, O., Tononi, G., Edelman, G.M., 2000. Theoretical neuroanatomy: relating anatomical and functional connectivity in graphs and cortical connection matrices. *Cerebral Cortex* 10, 127–141.
- Sporns, O., Tononi, G., Kötter, R., 2005. The human connectome: A structural description of the human brain. *PLoS Comput Biol* 1, e42.
- Stephan, K.E., Weiskopf, N., Drysdale, P.M., Robinson, P.A., Friston, K.J., 2007. Comparing hemodynamic models with dcm. *Neuroimage* 38, 387–401.
- Stoica, P., Moses, R.L., 1997. Introduction to spectral analysis. Prentice Hall, Upper Saddle River, N.J.
- Stouffer, S.E.S., DeVinney, L., Star, S., Williams, R., 1949. The american soldier, vol.1: Adjustment during army life. Princeton University Press .
- Suma, H., Murali, S., 2007. Principal component analysis for analysis and classification of fMRI activation maps. *International Journal of Computer Science and Network Security* 7, 235–42.
- Sun, F.T., Miller, L.M., D'Esposito, M., 2004. Measuring interregional functional connectivity using coherence and partial coherence analyses of fmri data. *Neuroimage* 21, 647–58.
- Tagliazucchi, E., Balenzuela, P., Fraiman, D., Chialvo, D.R., 2012. Criticality in large-scale brain FMRI dynamics unveiled by a novel point process analysis. *Front Physiol* 3, 15.
- Theiler, J., Eubank, S., Longtin, A., Galdrikian, B., Farmer, J., 1992. Testing for nonlinearity in time series: the method of surrogate data. *Physica D* 58, 77–94.

- Tournier, J.D., Calamante, F., Connelly, A., 2007. Robust determination of the fibre orientation distribution in diffusion MRI: non-negativity constrained super-resolved spherical deconvolution. *Neuroimage* 35, 1459–72.
- Tournier, J.D., Calamante, F., Connelly, A., 2012. MRtrix: Diffusion tractography in crossing fiber regions. *International Journal of Imaging Systems and Technology* 22, 53–66.
- Tournier, J.D., Calamante, F., Gadian, D.G., Connelly, A., 2004. Direct estimation of the fiber orientation density function from diffusion-weighted MRI data using spherical deconvolution. *Neuroimage* 23, 1176–85.
- Van De Ville, D., Blu, T., Unser, M., 2004. Integrated wavelet processing and spatial statistical testing of fmri data. *Neuroimage* 23, 1472–85.
- Vanhaudenhuyse, A., Demertzi, A., Schabus, M., Noirhomme, Q., Bredart, S., Boly, M., Phillips, C., Soddu, A., Luxen, A., Moonen, G., Laureys, S., 2011. Two distinct neuronal networks mediate the awareness of environment and of self. *J Cogn Neurosci* 23, 570–8.
- Vicente, R., Wibral, M., Lindner, M., Pipa, G., 2011. Transfer entropy—a model-free measure of effective connectivity for the neurosciences. *J Comput Neurosci* 30, 45–67.
- Van de Ville, D., Britz, J., Michel, C.M., 2010. EEG microstate sequences in healthy humans at rest reveal scale-free dynamics. *Proc Natl Acad Sci U S A* 107, 18179–84.
- Vincent, J.L., Patel, G.H., Fox, M.D., Snyder, A.Z., Baker, J.T., Van Essen, D.C., Zempel, J.M., Snyder, L.H., Corbetta, M., Raichle, M.E., 2007. Intrinsic functional architecture in the anaesthetized monkey brain. *Nature* 447, 83–6.
- Viviani, R., Grön, G., Spitzer, M., 2005. Functional principal component analysis of fmri data. *Hum Brain Mapp* 24, 109–29.
- Walker, G., 1931. On periodicity in series of related terms. *Philosophical Transactions of the Royal Society of London* 311.
- Welch, P.D., 1967. The use of fast fourier transform for the estimation of power spectra: A method based on time averaging over short, modified periodograms. *Audio and Electroacoustics, IEEE Transactions on* 15, 70–73.
- Wen, X., Rangarajan, G., Ding, M., 2013. Is granger causality a viable technique for analyzing fmri data? *PLoS One* 8, e67428.
- Whittaker, J., 1990. *Graphical Models in Applied Multivariate Statistics*. John Wiley, Chichester.
- Woolrich, M.W., Ripley, B.D., Brady, M., Smith, S.M., 2001. Temporal autocorrelation in univariate linear modeling of fmri data. *Neuroimage* 14, 1370–86.
- Yang, Z., Craddock, R.C., Margulies, D.S., Yan, C.G., Milham, M.P., 2014. Common intrinsic connectivity states among posteromedial cortex subdivisions: Insights from analysis of temporal dynamics. *Neuroimage* 93 Pt 1, 124–37.

- Yule, U., 1927. On a method of investigating periodicities in disturbed series, with special reference to wolfer's sunspot numbers. *Philosophical Transactions of the Royal Society of London* 226, 267–98.
- Zalesky, A., Breakspear, M., 2015. Towards a statistical test for functional connectivity dynamics. *Neuroimage* 114, 466–70.
- Zalesky, A., Fornito, A., Cocchi, L., Gollo, L.L., Breakspear, M., 2014. Time-resolved resting-state brain networks. *Proc Natl Acad Sci U S A* 111, 10341–6.
- Ziegler, E., Foret, A., Mascetti, L., Muto, V., Le Bourdiec-Shaffii, A., Stender, J., Balteau, E., Dideberg, V., Bours, V., Maquet, P., Phillips, C., 2013. Altered white matter architecture in BDNF met carriers. *PLoS One* 8, e69290.
- Zorzi, M., Sepulchre, R., 2015. AR Identification of Latent-variable Graphical Models. arXiv preprint arXiv:1405.0027 .

APPENDIX A

Methodological complements to Chapter 3

We provide some complementary results and arguments supporting the work presented in Chapter 3.

A.1 Correlation between SC and tFC

As already mentioned, we are computing correlations between SC and FC which itself is encoding correlations between fMRI time series. It could be argued that this is not appropriate because the variance of the correlation coefficients is not constant on the [-1,1] interval. This could be addressed by applying a variance-stabilizing transformation such as the Fischer transformation but we did not use this approach in this work for two reasons.

First because SC is not encoding a correlation coefficient and hence the matching between the values in FC and SC should not a priori be addressed using this type of transformation, the log-rescaling being an alternative.

The other reason is that we wanted to stick to the methodology presented in [Honey et al. \(2009\)](#) in order to explore which additional information we get by going from the static to the temporal case, all other things being equal.

Let us finally note that we computed the correlation between FC and SC after applying this transformation and did not find significant differences. One possible explanation for that could be that there are few 'extreme' values in FC and hence the Fisher transform does not modify significantly the values in FC since the transformation has very mild effect for correlation coefficients in the [-0.7, 0.7] interval.

A.2 Other markers of statistical significance

In order to confirm the significance of the window width determined using V we used another marker to differentiate the original and surrogate datasets: the variance of the temporal correlation $R(t)$. The result shown in Figure A.1 presents a peak of significance around $w=20$ TR = 40 sec, thereby confirming our findings.

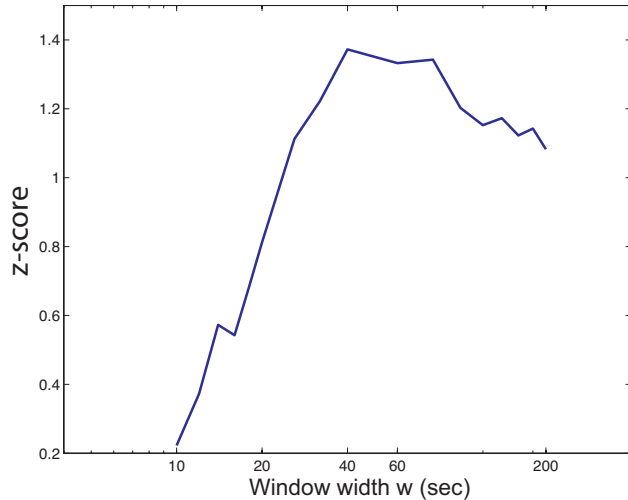


Figure A.1 – Estimation of the statistical significance region based on the variance of the temporal correlation $R(t)$.

Figure A.2 shows that we could not differentiate original and surrogate datasets based on the main oscillatory mode of $R(t)$. This suggests that F^* is imposed by the window width w and does not necessarily capture effects of neuronal fluctuations.

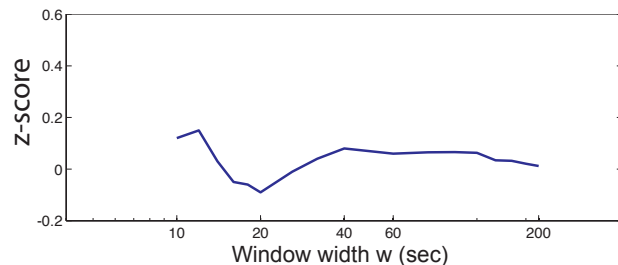


Figure A.2 – Estimation of the statistical significance region based on F^* .

A.3 Influence of the threshold

Finally, as mentioned in chapter 3, Figure A.3 shows that the choice of the thresholds T used to compute average FC patterns and corresponding graph metrics during high and low correlation between SC and tFC (only highest and lowest T% of R(t) are considered) does not influence the general trend observed in Figure 3.6.

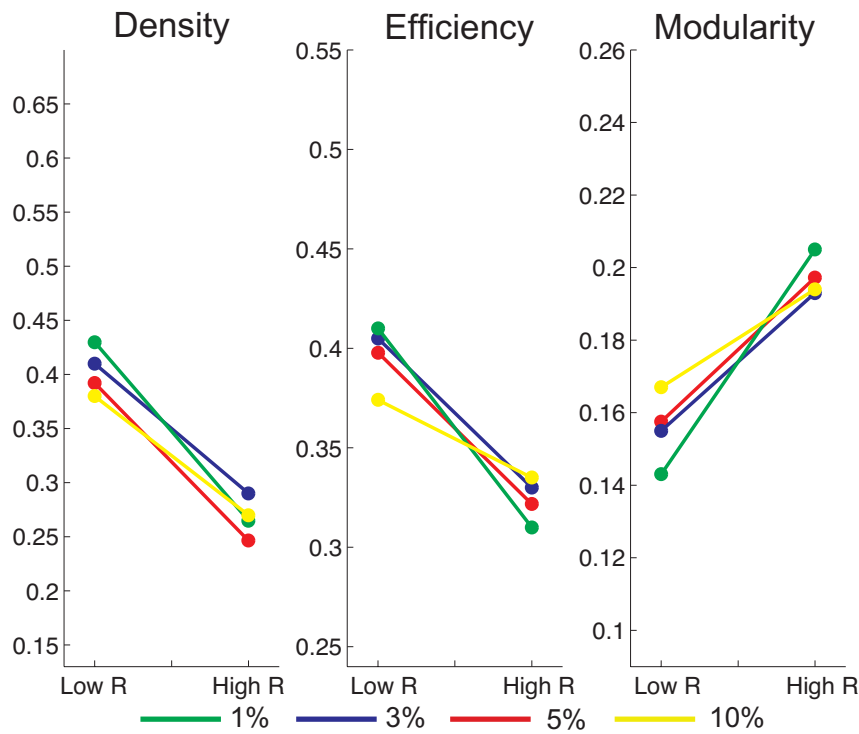


Figure A.3 – Average evolution of graph metrics for four different thresholds.

APPENDIX B

Gaussianity assumption in component analysis

This Appendix presents detailed examples of application of PCA and ICA on gaussian and non-gaussian datasets for the reader interested in getting deeper intuition about these related yet different component analysis techniques.

B.1 Measuring (non-)gaussianity

Let us first recall that non-gaussianity is usually measured in ICA by evaluating the *kurtosis* of the candidate components.

Definition B.1.1 *Let x be a random variable. Its kurtosis $K(x)$ is defined by*

$$K(x) = \frac{\mu_4(x)}{\sigma^4(x)} - 3, \quad (\text{B.1})$$

where

- $\mu_4(x)$ is the fourth statistical moment of x ,
- $\sigma(x)$ is the standard deviation of x ,
- a constant term is added to match gaussian distributions with $K = 0$. ◊

This measure allows to evaluate how far a given distribution is from gaussianity. Distributions with $K > 0$ are called super-gaussian and are characterized by sharper peaks at the mean (zero in our case). On the other hand distributions with $K < 0$ are called sub-gaussian and exhibit broader distributions. Examples of three distributions with zero mean and unit variance are represented in Figure B.1.

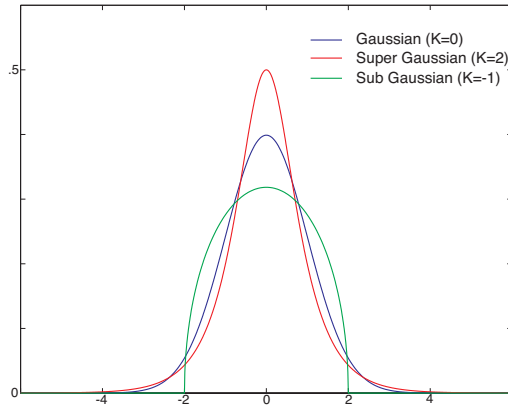


Figure B.1 – Super-gaussian, gaussian, and sub-gaussian distributions

B.2 PCA and ICA on adequate datasets

We first illustrate how PCA and ICA work on datasets verifying the corresponding generative modelling assumptions.

B.2.1 PCA on gaussian data

Consider two gaussian variables x_1 and x_2 composing the lines of $\mathbf{X}_{m,T}$ with $m = 2$. The output provided by PCA is shown in Figure B.2.

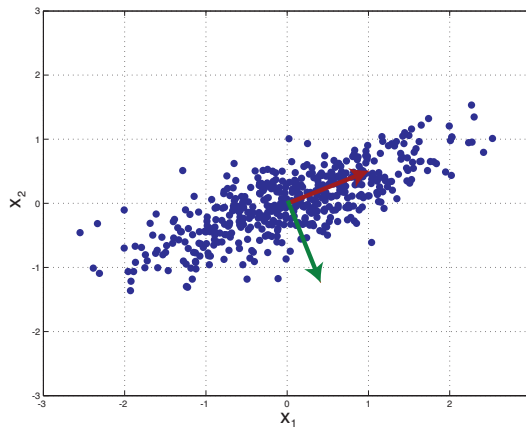


Figure B.2 – Application of PCA on gaussian data

The direction of maximum variance are identified, the red arrow is the first principal component, along which the variation is maximal and the green arrow is the second principal component, orthogonal to the first principal component.

B.2.2 ICA on non-gaussian data

Let us consider o_1 and o_2 the *sub-gaussian* original signals one wants to identify and represented in Figure B.3.

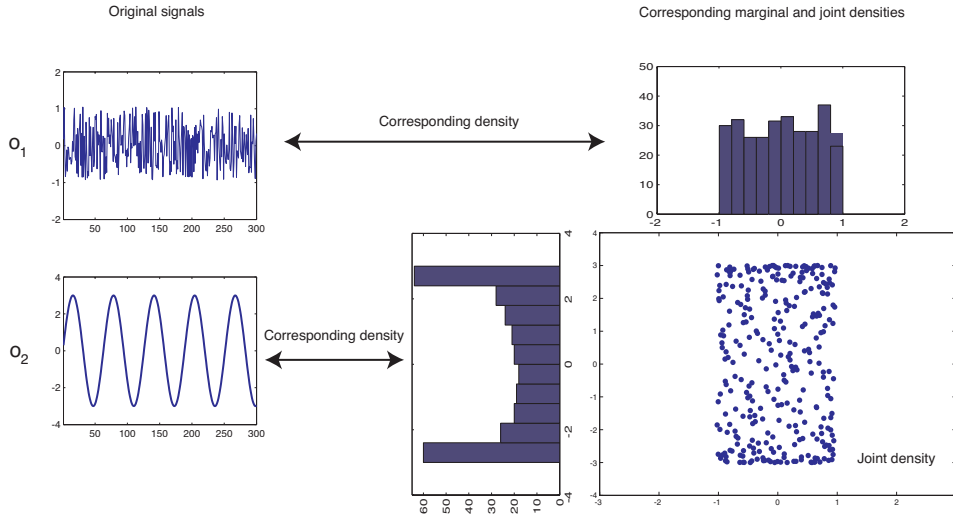


Figure B.3 – Original sub-gaussian signals and corresponding marginal and joint densities

After randomly mixing the signals, we get two linear combinations of o_1 and o_2 that we call x_1 and x_2 , the lines of $\mathbf{X}_{2,T}$, represented in Figure B.4.

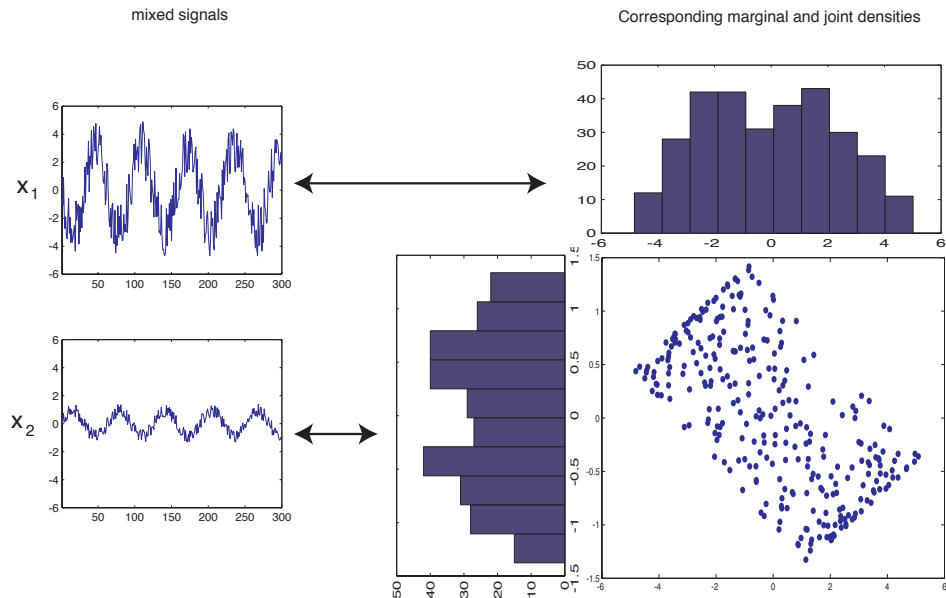


Figure B.4 – Mixed signals and corresponding marginal and joint densities

As a consequence of the central limit theorem we observe that the random mixing of o_1 and o_2 leads to mixed signals x_1 and x_2 with marginal densities closer to gaussianity (higher algebraic value of kurtosis). The ICA algorithm now proceeds in successive steps as follows ([Hyvärinen, 1999](#)):

1. **Whitening of the data:** this implies an un-stretching of the joint probability density (the angles of the joint probability distribution are made right) and a rescaling corresponding to the normalization of the variances.
2. **Projection pursuit:** this steps consists of looking for directions onto which the projections are as *independent* as possible. As discussed in section 7.2.1 this translates into looking for the most non-gaussian projections. These first two steps are represented in Figure B.5.

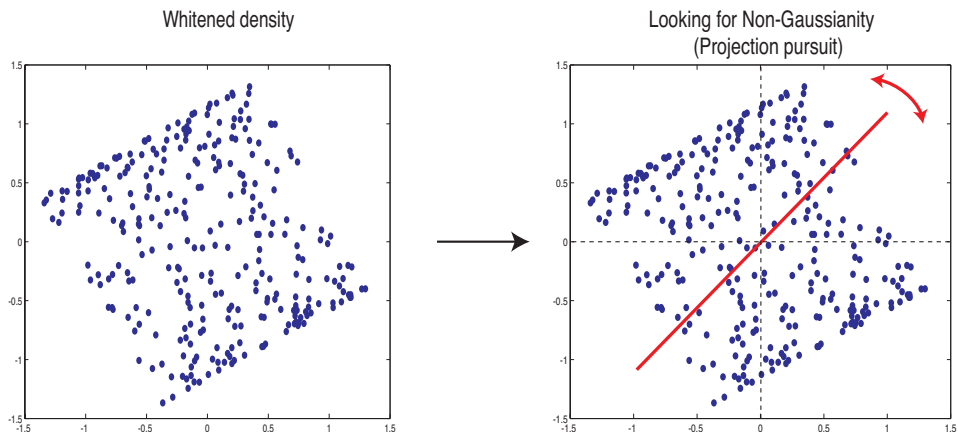


Figure B.5 – Whitening and projection pursuit steps

3. **Unwhitening:** once the directions of maximum non-gaussianity are found based on the whitened data the last step consists of going back to the initial space of representation, or unwhitened space. The independent components y_1 and y_2 (lines of $\mathbf{Y}_{2,T}$) are finally recovered by projecting the data onto the directions determined by the projection pursuit, as represented in Figure B.6.

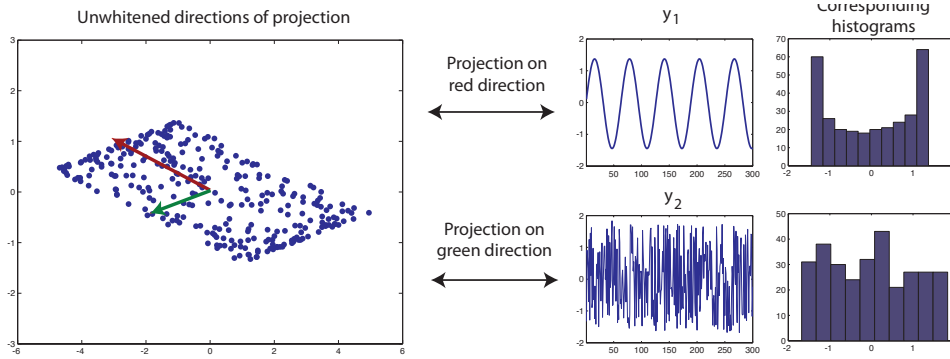


Figure B.6 – Final step of the ICA algorithm

The recovered independent components y_1 and y_2 are close to the original signals o_1 and o_2 , as expected.

B.3 PCA and ICA on inadequate datasets

Let us now switch the starting datasets and consider how PCA behaves on the non-gaussian dataset shown in Figure B.4 and conversely, how ICA deals with a gaussian input.

B.3.1 PCA on non-gaussian data

Starting from the joint density presented in Figure B.4, PCA aims at finding the directions of maximum variance of the joint density as illustrated in Figure B.7.

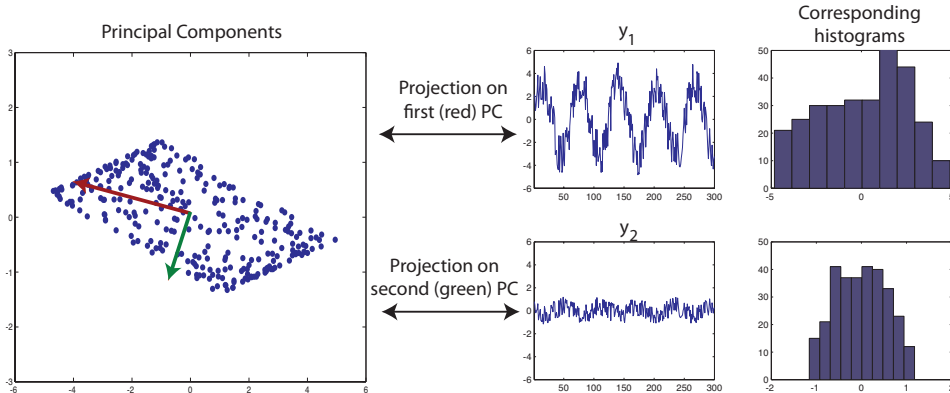


Figure B.7 – Application of PCA on non-gaussian data

The left panel of Figure B.7 shows that PCA considers a gaussian distribution of the data and neglects the particular structure of the joint density that arises from non-gaussianity of the original signals, leading to a poorer identification of the original signals o_1 and o_2 .

B.3.2 ICA on gaussian data

We apply ICA on the dataset shown in Figure B.2. In this case the whitening step produces a totally symmetric distribution from which no information can be deduced anymore (Figure B.8)

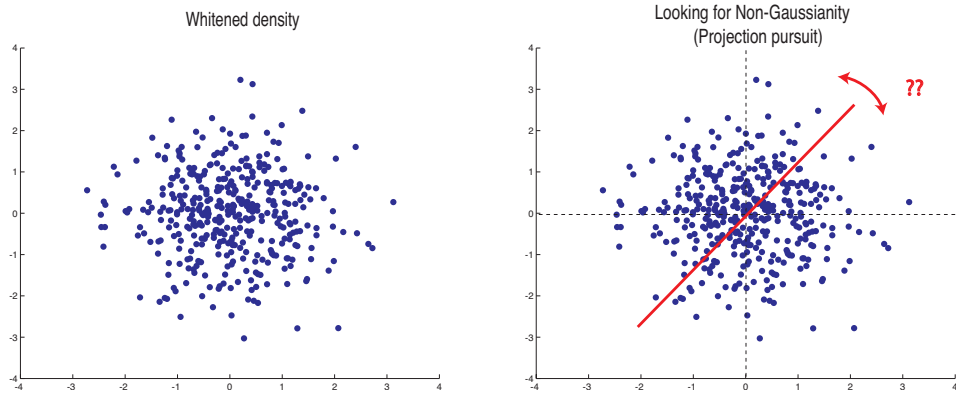


Figure B.8 – Whitening gaussian data

As a consequence, the projection pursuit step won't find any relevant local extrema and when there is convergence of the algorithm the directions of projection will be very different at each run and almost random as illustrated in Figure B.9

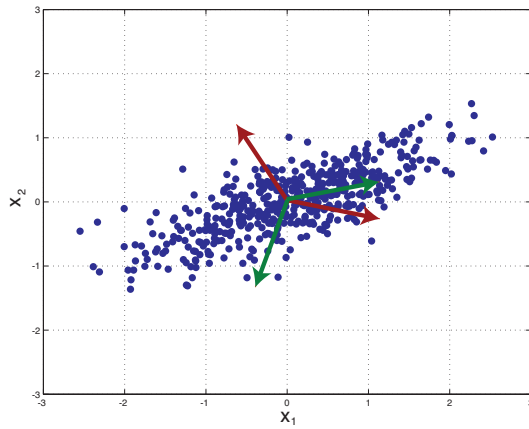


Figure B.9 – Two runs of the ICA algorithm on gaussian data lead to two different results